In the Trenches of the Solar-Stellar Connection.
I. Ultraviolet and X-ray Flux–Flux Correlations
Across the Activity Cycles of the Sun and Alpha Centauri AB

Thomas R. Ayres

Center for Astrophysics and Space Astronomy,
389 UCB, University of Colorado, Boulder, CO 80309;
Thomas.Ayres@Colorado.edu

ABSTRACT

This study focuses on high-energy proxies of stellar magnetic activity over long-term starspot cycles of three low-activity sunlike stars: α Centauri A (HD 128620: G2 V), α Cen B (HD 128621: K1 V), and the Sun itself. Datasets include: solar UV irradiance spectra from *SORCE*–SOLSTICE, and X-ray fluxes from *SORCE*–XPS, during recent sunspot Cycles 23 and 24; IRIS long-slit stigmatic imaging of solar Mg II h (2803 Å) and k (2796 Å) in quiet and active regions; and *HST*-STIS UV, and *Chandra* X-ray, campaigns on α Cen AB. Established stellar "flux–flux" relations, for example X-rays ($T \sim 1$ MK) versus Mg II ($T \sim 8000$ K), showed increasing power-law slopes with increasing formation temperature; but these give way on the Sun to bent power laws, and surprising inversions in the activity hierarchy: Si III is more "active" (steeper power laws) than N V, despite the latter's four times higher formation temperature. The Sun's flux–flux behavior, nevertheless, remarkably parallels low-activity solar twin α Cen A. In contrast, the cooler, somewhat more active, K dwarf companion displays correlations more in line with the previous stellar paradigm. The new flux–flux relations offer a way to vet numerical spectral simulations and proxy-based irradiance models; extrapolate solar global activity indices into regimes below or above the grasp of contemporary records; or to exoplanet hosts at the low end of the sunlike activity ladder.

Subject headings: Sun: activity — Sun: UV radiation — Sun: X-rays — stars: activity — ultraviolet: stars — X-rays: stars — techniques: spectroscopic — stars: individual (the Sun, HD 128620, HD 128621)

1. INTRODUCTION

The magnetic "activity" of cool, convective stars reveals itself in many ways. Perhaps most familiar are the dark magnetized sunspots prominent at times on the solar disk, and which, in the remote stars, are visible by periodic dimming of their optical light curves. Also conspicuous, at least to a variety of orbiting space observatories, are the bright ultraviolet and X-ray emissions associated with over-heated layers of the solar outer atmosphere ("chromosphere" [$T \sim$ 8000 K] and "corona" [$T \sim$ 1 MK]). A curiosity of the solar activity is the 11-year ebb and flow of sunspots (an even more remarkable 22-year progression considering the alternate flip-flops of the global mean magnetic field), a phenomenon that also has been recognized in the stars thanks to long-term monitoring of optical chromospheric Ca II emission by O. C. Wilson (1978), and others.

The activity and magnetic cycling are attributed to a deep-seated Dynamo (Parker 1970), inhabiting a thin shear layer sandwiched between the outside convective envelope and inside radiative zone (e.g., Hughes et al. 2007). The Dynamo is powered by convection and rotation, needing the former to operate at all, and increasing in strength in step with the latter. Late-type stars normally begin their lives spinning rapidly (e.g., Stauffer & Hartmann 1986) and experience dramatically elevated activity, but their magnetically coupled coronal winds dissipate stellar angular momentum (e.g., Weber & Davis 1967; Matt et al. 2010), thus throttling the rotation – and activity – over time (Kraft 1967; Skumanich 1972; see also Bouvier 1994).

An important consequence of the activity, and its evolution, is the impact of the associated ionizing radiation on planetary atmospheres, not only within our own Solar System (e.g., Zahnle & Walker 1982; Ayres 1997; Guinan et al. 2003; Claire et al. 2012), but now extending out to the domain of the exoplanets (e.g., Kasting et al. 1996; Chadney et al. 2015; France et al. 2016; Ribas et al. 2016). (An extensive discussion of the various types of spectral simulations and proxy-based modeling to derive estimates of the EUV radiation loading on planetary atmospheres, for the specific case of Mars, can be found in Thiemann [2016]. See, also, Fontenla et al. [2016] and Peacock et al. [2019] for the more extreme situation of M-dwarf exoplanet hosts.)

When the initial wave of space-borne telescopes, like *Einstein* X-ray Observatory (Giacconi et al. 1979) and *International Ultraviolet Explorer* (Boggess et al. 1978), first investigated late-type activity, one of the early discoveries was that the high-energy emissions were tightly correlated with one another, for example 0.2–2 keV coronal soft X-rays versus chromospheric Mg II 2800 Å (Ayres et al. 1981). That these emissions were strongly linked was not surprising. After all, they must arise in the same magnetically influenced regions. But, remarkably, the power-law exponents were steeper than unity, something like $\alpha \sim 3$ for

the coronal-chromospheric pair mentioned above. Apparently, the high-temperature coronal emissions rise proportionately much more rapidly with increasing lower temperature chromospheric strength. This was unexpected because the prevailing view at the time, motivated by the solar example, was that more active stars were "more active" simply because they were covered by a larger area of the UV- and X-ray-bright "active regions" (also called chromospheric plage) associated with, and surrounding, the dark, highly magnetized spots on the Sun. This idea had its origin in the fact that daily global ultraviolet and X-ray emissions of the Sun closely tracked the area of spot groups on the visible hemisphere as they came and went over the magnetic cycle. If this were true for other stars, one might anticipate that the various activity indices would increase linearly with the chromospheric plage area, and thus directly correlate with one another. However, the evident non-linear power laws suggested that something beyond a simple area factor was at work.

One possibility was an observational bias whereby the lower excitation chromospheric species, such as Mg II, might have a dual identity, partly associated with the magnetic plages, but also partly energized by other processes not directly connected with the cycling activity (such as acoustic shock waves stemming from constructive interference of photospheric p-mode oscillations; as simulated numerically by Carlsson & Stein [1995, 1997]; and embodied in the "Clapotisphere" promoted by R. J. Rutten [1995]). In that case, there could be a cycle-independent baseline flux, which when removed, might restore a more linear correlation against a higher excitation species (one that might be completely dominated by the cycling component). R. G. M. Rutten et al. (1991) called this background level the "basal flux." However, even when such a contribution could be estimated (say, by focusing on the least active stars in a broad sample) and subtracted, nonlinear power laws still remained, especially for X-rays (ibid; see, also, Schrijver 1983). Furthermore, enhanced coronal X-ray luminosities usually were accompanied by hardening of the X-ray spectrum, indicating increasing average coronal temperatures (e.g., Schmitt et al. 1990; Preibisch 1997). Also seen was an uptick in the transient large-scale violent explosions called flares on active (i.e., fast-rotating) sunlike stars (e.g., Maehara et al. 2012). These effects were additional indications that the active regions on active stars change character as the overall magnetic involvement intensifies.

Although flux–flux correlations are a staple on the cool-star side of the solar-stellar connection, the tool rarely has made an appearance on the solar side. Mainly, one finds correlations between various activity proxies, like sunspot numbers, the 10.7 cm radio index, or total unsigned magnetic flux Φ_{m}, against a dominant FUV emission, such as H I 1215 Å Lyα, or the coronal soft X-ray flux (e.g., Pevtsov et al. [2003] for X-rays versus Φ_{m}). Notable exceptions to the rule include the Lyα proxy-modeling of Woods et al. (2000), who examined the variation of the solar H I flux against several FUV emission species, such as the O I 1305 Å triplet and the C I 1657 Å multiplet; and the extensive thesis work of R. Hock (2012), who

assessed the short-term behavior of extreme-ultraviolet (EUV: roughly 10–1050 Å) emission lines during solar flare outbursts. Hock constructed numerous flux–flux diagrams contrasting the joint histories of pairs of high-excitation diagnostics (e.g., Fe XII 195 Å [$\log T \sim 6.1$] versus Fe XX 133 Å [$\log T \sim 7.0$]; or O V 630 Å [$\log T \sim 5.4$] versus He II 304 Å [$\log T \sim 4.7$]) as the dynamic, strongly heated plasma events evolved through their impulsive rise phases and subsequent gradual decays (see her Appendix E). Hock's work was based mostly on the EUV Variability Experiment (EVE: Woods et al. 2012) on *Solar Dynamics Observatory* (*SDO*: Pesnell et al. 2012), which is analogous (aside from the shorter wavelengths covered) to the *SORCE*–SOLSTICE spectrometer (1150–3100 Å) that is the main focus of the solar flux–flux diagrams described later. (EVE and SOLSTICE both were built and operated by the Laboratory for Atmospheric and Space Physics [LASP] at the University of Colorado.)

Previous studies of the stellar flux–flux relations typically were based on moderate-size surveys, in which each star usually was observed only once, or at most a few times, catching just a glimpse of the long-term activity state of the object (e.g., R. G. M. Rutten et al. 1991; Ayres et al. 1995; or more recently, Youngblood et al. 2017 for M dwarfs). The alternative would be to focus on a single stellar subject, but in the time domain, pivoting to the long-term evolution of the star's activity cycle. Such a time series might illuminate key details that otherwise could be obscured in a large heterogeneous stellar sample, owing to distractions imposed by natural dispersions of age, surface temperature, spin periods, metallicity, and so forth. The present study examines the three (actually, only) sunlike stars for which suitable long-term UV and X-ray records exist: nearby ($d \sim 1.34$ pc) α Centauri A (G2 V) and α Cen B (K1 V), and the Sun (G2 V) itself.

The paper is organized as follows. The initial sections describe the three stars of the project, and the solar and stellar instruments that were utilized. The middle sections outline the measurement strategies, including a series of cross-calibrations to place the solar and stellar activity indices on as equitable a basis as practical. The penultimate section presents, and compares, various flux–flux correlations across the activity cycles of the three subject stars. The paper concludes with a discussion of the findings. The conclusions are relatively slim, as befits the primarily observational nature of this work.

2. OBSERVATIONS

2.1. The Stellar Players

Given that most of the stars within a few pc of the Sun are low-mass, diminutive red dwarfs, it is unsurprising that the nearest star is one of these, dM5 Proxima Centauri

(α Cen C). Despite the preponderance of dwarf Ms in the solar neighborhood, however, the 2nd and 3rd closest stars (α Cen A and B [hereafter AB]) are rather solar-like, nearly precisely bracketing our Sun in mass, luminosity, temperature and coronal activity levels. The system appears to be somewhat older than the Sun, although perhaps by only a Gyr, or less (e.g., Bazot et al. 2012), and slightly metal-rich (e.g., Morel 2018). The proximity, and multiplicity, of α Cen ensures that it will be the first stop if humanity ever attempts interstellar travel, but also renders the system a natural target for investigations of sunlike phenomena on other stars, because nearest and brightest holds a special advantage.

Properties of the three subjects are summarized in Table 1 (for α Cen AB mainly from the comprehensive study by Kervella et al. 2017). Because the central AB binary of α Cen is a visual pair with a long history of astrometry and radial velocities, the 80-year orbit is well characterized. Thus, the masses of the two stars are precisely known, at least more so than for many other such systems. Further, there are interferometric measurements of the stellar radii (Kervella et al. 2017), and additional support from asteroseismology (e.g., Miglio & Montalbán 2005). Most of the time in their mutual orbit, AB are well separated on the sky ($> 10''$), with minimum scattered light confusion, so the optical photometry – luminosities and colors – of the pair are well established. This extends to spectroscopic measurements of the metallicity of the system, which is slightly elevated compared to the Sun by about 0.2 dex (see recent summary by Morel 2018). In fact, one can attempt a global solution for the binary age (e.g., Flannery & Ayres 1978; for a modern implementation, incorporating seismic constraints, see Bazot et al. 2012 and Joyce & Chaboyer 2018), taking the well established luminosities and masses as a Bayesian prior, and solving for the set of mass- and composition-dependent evolutionary tracks that jointly predict the correct luminosities of the pair at the same age. Within that set, the effective temperatures of the stars at that evolutionary crossroads should be consistent with the input $T_{\rm eff}$-dependent metallicities, assuming [Fe/H] is the same for both components. The main uncertainties stem from the various approximations in the underlying evolutionary models (e.g., 1D mixing-length parameters), and the atmospheric temperature profiles by which metallicities were derived. An advantage in this case is that the properties of AB are very close to the Sun's, so any differential results likely are robust.

Table 1. Stellar Properties

Name	HD No.	Type	M	R	L_{BOL}	T_{eff} (K)	[Fe/H]	f_{BOL} (erg cm^{-2} s^{-1})	v_{ROT} (km s^{-1})
Sun	$\cdots$	G2 V	1.99×10^{33} gr	6.96×10^{10} cm	3.83×10^{33} erg s^{-1}	5770	$+0.00$	1.361×10^{6}	2.0^{a}
α Cen A	128620	G2 V	$1.11\,M_{\odot}$	$1.22\,R_{\odot}$	$1.52\,L_{\odot}$	5800 ± 20	$+0.24\pm0.01^{b}$	2.718×10^{-5}	2.1–2.8^{c}
α Cen B	128621	K1 V	$0.94\,M_{\odot}$	$0.86\,R_{\odot}$	$0.50\,L_{\odot}$	5230 ± 20	$+0.22\pm0.02^{b}$	0.899×10^{-5}	1.1^{d}

Note. — Parameters for α Cen AB abstracted from, or based on, Kervella et al. (2017).

[a] For surface rotation period of 25.7 d at 30° latitude.

[b] Morel (2018): [C/Fe]$\sim$(-0.02) $-$ (-0.04); [O/Fe]$\sim$(-0.06) $-$ (-0.09). [c] Hallam et al. (1991): $P_{\mathrm{ROT}} \sim 29$ d; Saar & Osten (1997), $v_{\mathrm{ROT}} \sim 2.8$ km s^{-1}, with $i \sim 79°$.

[d] Dumusque et al. (2012): $P_{\mathrm{ROT}} \sim 39$ d.

2.2. Facilities

2.2.1. Chandra *High-Resolution Camera*

Chandra (Weisskopf et al. 1996) pointings on α Cen AB have been carried out on a regular basis (roughly every six months) since late-2006, with the High-Resolution Camera (HRC-I: Murray et al. 1997). This is the imager of choice for optically bright, but spectrally soft coronal X-ray sources (Ayres et al. 2008). The separation of the binary on the sky has been closing in recent years, reaching a minimum of $4''$ at the end of 2015. Among the several X-ray-capable telescopes in orbit at present, only *Chandra* with its $1''$ spatial resolution is able to successfully image AB without confusion (and for the foreseeable future: the separation increases to about $10''$ in 2028, but then decreases again through the 2030's). There was an earlier observation of AB at the end of 1999 with *Chandra's* Low-Energy Transmission Grating Spectrometer (LETGS; Raassen et al. 2003), and two subsequent LETGS exposures in 2007 and 2011, from which the coronal luminosities can be deduced from the grating zeroth-order images (Ayres 2014). *XMM-Newton* (Jansen et al. 2001) also obtained a series of imaging spectra of AB, beginning in early-2003 and continuing (sporadically, about once a year) to the present, although 2003–2008 is the most useful time frame, when the binary still was partially resolved by the $\sim10''$ imaging of the ESA telescope (Robrade et al. 2012). Unfortunately, mandatory use of the thick optical blocking filter (the *XMM-Newton* European Photon Imaging Camera [EPIC: Briel et al. 2000] is susceptible to "red leak" for optically bright sources like AB) apparently significantly suppressed the soft response, to the extent that cool-corona α Cen A ($T \lesssim 1$ MK) virtually disappeared from the EPIC images in early-2005 (Robrade et al. 2005: "The Darkening of the Solar Twin"), when the sunlike dwarf entered a minimum of its long-term activity cycle. The hotter ($T \gtrsim 2$ MK) corona of K-type B was less affected by the muted soft response of EPIC. Because B is X-ray brighter than A most of the time, the *XMM-Newton* time series of the partially blended AB images is most relevant for the K star.

Table 2 summarizes the *Chandra* X-ray observations of α Cen AB to date (2020.4), including only the HRC-I exposures (ignoring the three LETGS zeroth-order HRC-S measurements, which are less well calibrated). The X-ray light curves of both stars during the short-term (5–10 ks) pointings were filtered against transient flare activity (Ayres 2014), so far seen exclusively from the more active B component and at the higher phases of its long-term cycle.

Table 2. *Chandra* HRC-I Pointings

ObsID	UT$_{\rm mid}$	$t_{\rm exp}$	(CR)$_{\rm A}$	(CR)$_{\rm B}$	($L_{\rm X}$)$_{\rm A}$	($L_{\rm X}$)$_{\rm B}$
	(yr)	(ks)	(counts s^{-1})		(10^{27} erg s^{-1})	
(1)	(2)	(3)	(4)	(5)	(6)	(7)
6373	2005.805	5.15	0.45±0.04	2.20±0.15	0.27	1.99
6374	2006.362	5.11	0.45±0.03	0.99±0.07	0.26	0.79
6375	2006.960	2.67	0.41±0.04	0.94±0.10	0.24	0.74
7433	2007.469	5.04	0.45±0.04	0.71±0.04	0.27	0.54
7434	2007.961	5.11	0.47±0.04	0.74±0.04	0.28	0.57
8906	2008.389	10.08	0.46±0.03	0.81±0.08	0.28	0.62
8907	2008.961	9.34	0.47±0.05	0.87±0.06	0.28	0.68
9949	2009.409	10.06	0.43±0.04	1.48±0.06	0.25	1.25
9950	2009.949	10.05	0.49±0.04	1.83±0.08	0.29	1.60
10980	2010.335	9.76	0.62±0.05	3.32±0.65	0.39	3.20
10981	2010.808	10.03	0.49±0.05	2.75±0.19	0.29	2.58
12333	2011.437	4.88	0.63±0.05	2.20±0.15	0.39	1.99
12334	2011.993	10.07	0.56±0.04	3.35±0.17	0.34	3.24
14191	2012.473	10.10	0.76±0.07	2.82±0.10	0.49	2.66
14192	2012.950	10.06	0.92±0.06	2.38±0.10	0.61	2.18
14193	2013.480	10.59	0.83±0.07	1.93±0.10	0.54	1.72
14232	2013.963	10.05	0.95±0.05	2.01±0.10	0.63	1.79
14233	2014.477	9.62	0.86±0.07	1.40±0.09	0.56	1.18
14234	2014.999	10.11	0.83±0.06	1.64±0.16	0.54	1.41
16677	2015.346	10.07	1.10±0.07	1.36±0.07	0.75	1.14
16678	2015.810	10.08	1.13±0.06	1.01±0.05	0.77	0.81
16679	2016.330	10.03	0.89±0.05	1.19±0.08	0.58	0.98
16680	2016.771	10.01	1.06±0.05	1.31±0.06	0.72	1.09
16681	2017.335	9.99	0.96±0.06	2.11±0.18	0.64	1.90
16682	2017.823	10.00	0.74±0.05	2.64±0.12	0.47	2.46
20987	2018.378	5.12	0.96±0.06	3.64±0.18	0.64	3.58
21572	2018.967	5.11	0.68±0.04	2.96±0.10	0.43	2.81
21573	2019.391	5.10	0.76±0.06	3.26±0.10	0.49	3.14

Table 2—Continued

ObsID	$\mathrm{UT_{mid}}$	t_exp	$\mathrm{(CR)_A}$	$\mathrm{(CR)_B}$	$(L_\mathrm{X})_\mathrm{A}$	$(L_\mathrm{X})_\mathrm{B}$
	(yr)	(ks)	(counts s^{-1})		(10^{27} erg s^{-1})	
(1)	(2)	(3)	(4)	(5)	(6)	(7)
21574	2020.097	5.07	0.56±0.04	3.02±0.16	0.34	2.87
21575	2020.428	5.11	0.49±0.06	3.90±0.44	0.29	3.87

Note. — Col. 3 exposure duration includes dead-time correction. Cols. 4 (α Cen A) and 5 (B) count rates were time-filtered to remove flare enhancements, if any; and were corrected for the 95% encircled energy of the $r = 1.5''$ detect cell. Cited uncertainties reflect standard deviations of time-binned count rates with respect to flare-filtered averages. Cols. 6 (α Cen A) and 7 (B) X-ray luminosities (0.2–2 keV) were derived from the count rates using source-dependent Energy Conversion Factors (See Ayres 2014 for details), and $d = 1.338$ pc (e.g., Kervella et al. 2017). $(L_\mathrm{X})_\odot \sim 0.4$–1.9 in same energy band and luminosity units.
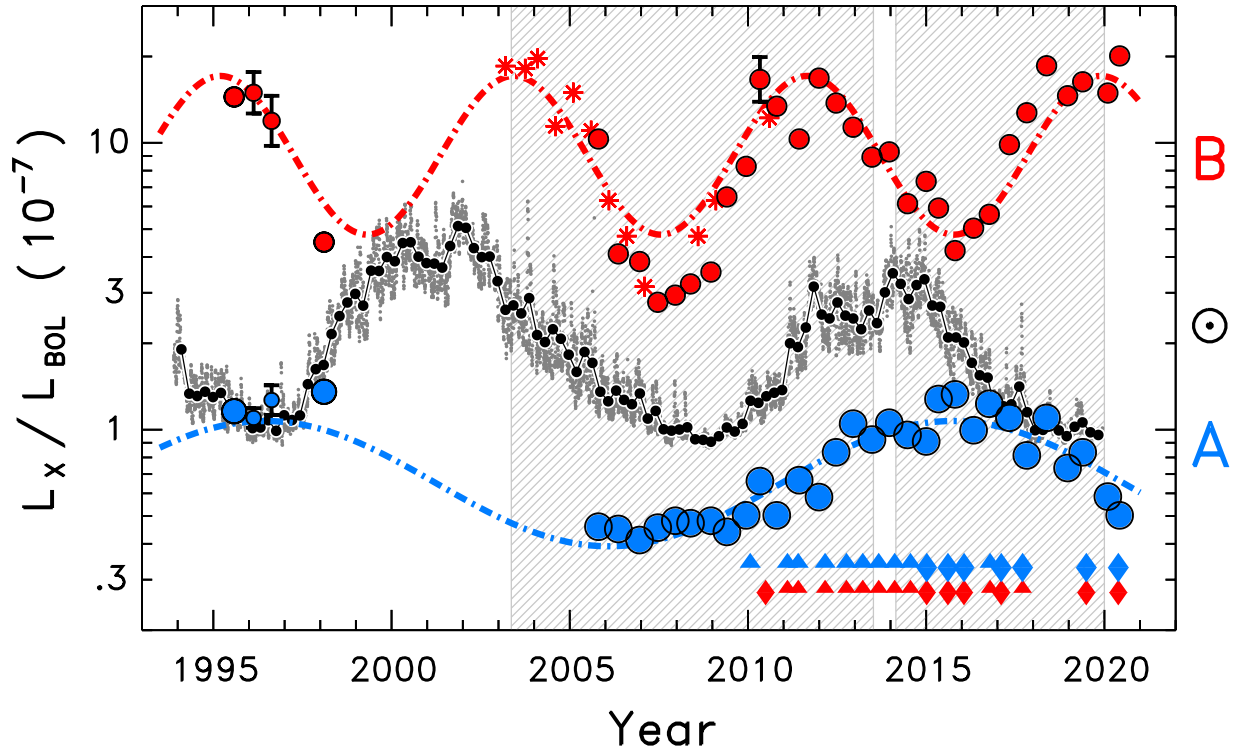
Fig. 1.— Long-term, bolometrically normalized X-ray (0.2–2 keV) light curves of α Cen AB, and the Sun.

Figure 1 illustrates α Cen's X-rays over the past nearly three decades: α Cen A in blue, B in red. A series of *ROSAT* campaigns and single pointings prior to 2000 serve to anchor the later *Chandra* and *XMM-Newton* efforts (the latter shown for B, only, and just through 2010.5). The α Cen AB $L_{\mathrm{X}}/L_{\mathrm{BOL}}$ ratios are slightly different than reported previously owing to adoption of the revised bolometric luminosities, and system distance, of Kervella et al. (2017). Also included is the solar X-ray light curve over previous Cycle 23 and current Cycle 24 (small gray points are daily values; connected dark dots are 81-day averages [3 synodic rotations]), based on Flare Irradiance Spectral Model 2 (FISM2)[1] reconstructions of various high-energy datasets, most homogeneous since 2003. These solar values also differ somewhat from previous reports owing to changes from original FISM to new FISM2 (as outlined in the *SORCE*–XPS section later [§2.2.4]). The gray hatched background highlights the time frame of the solar *SORCE* mission (another key player in this study). The chain of symbols at lower right indicate epochs of *HST* STIS spectroscopy, as described later.

If one accepts the pre-*Chandra* measurements at face value, with some extrapolation over the several gaps, the indicated cycles (via log-sinusoidal modeling) are 19 years for α Cen A, longer than the Sun's iconic 11-year spot period; and only 8 years for B, shorter than solar. These ~50 % differences are despite the only ±10% spread in the stellar masses of AB relative to the Sun (Table 1).

2.2.2. HST *STIS*

Space Telescope Imaging Spectrograph (STIS: Woodgate et al. 1998) has been a fixture in the instrument bay of *Hubble* for more than two decades. It is a multi-mode UV/Optical spectral imager, the workhorse for high precision studies of bright stars, both hot and cool, as well as many other types of cosmic objects, including the Interstellar Medium and Intergalactic counterparts. The STIS modes commonly used for cool stars are the medium-resolution ($\lambda/\Delta\lambda \sim 45{,}000$) FUV (1150–1700 Å) echelle grating E140M (which has the single home position 1425 Å covering the full FUV range), and the high-resolution ($\lambda/\Delta\lambda \sim 110{,}000$) NUV (1600–3200 Å) echelle E230H, primarily for Mg II "h" (2803 Å) and "k" (2796 Å). These are the brightest emission lines of, and dominant sources of radiative cooling in, a low-activity stellar chromosphere like the Sun's. Three grating settings ("CENWAVEs") of E230H are available for the purpose: prime 2762 Å and two flanking secondaries, 2713 Å and 2812 Å; all of which overlap in the hk interval at 2800 Å.

For bright stars like α Cen AB, especially larger warmer A, a neutral-density (ND)

---

[1]see: http://lasp.colorado.edu/lisird/data/fism_daily_hr/

filtered aperture often must be used, although cooler α Cen B is faint enough in the 2713 Å CENWAVE to avoid the (less-well calibrated) ND apertures. Even so, the narrow "spectroscopic" slit ($0.2'' \times 0.09''$), with somewhat reduced throughput, must be deployed to prevent a detector Global Count Rate violation. For E140M-1425, the FUV emissions of both A and B are faint enough – even bright H I 1215 Å Lyα – that the high-throughput, well-calibrated "photometric" slot ($0.2'' \times 0.2''$) is safe. This aperture provides more accurate photometry than the narrower slits, without significant loss of resolution, especially in the face of small thermally driven focus drifts of *Hubble's* Optical Telescope Assembly (OTA).

Alpha Cen AB have been observed by STIS approximately every six months since shortly after Servicing Mission 4 (in 2009, when STIS was revived after a long hibernation following an electrical failure 5 years earlier). These pointings were part of a long-term joint *Chandra/HST* campaign to track the X-ray and UV activity cycles of the two nearby sunlike stars. An earlier series of STIS FUV and NUV observations of α Cen A, at the highest possible echelle resolution, was carried out in 1999 (Pagano et al. 2004). However, these spectra pre-dated the *Chandra* X-ray campaign, and for that reason were not included in the present study.

Most of the FUV observations of α Cen AB utilized the E140M plus photometric slot combination described earlier. However, the observations of α Cen B since 2015 have used high-resolution E140H echelle settings instead, because many of the lower excitation emission lines of the K dwarf (especially Cl I 1351 Å) are narrower than those of the G star. These pointings were done with a pair of overlapping E140H secondary settings; and through the photometric aperture, which further ensured an accurate relative, and absolute, flux scale. There are eight of the E140H pairs for B to date (2020.4), together with an additional nine earlier E140Ms. For α Cen A, the 17 available FUV epochs are exclusively E140M with the photometric slot. The deeper E140M exposures ($t_{\mathrm{exp}} \gtrsim 3600$ s) of each star were split into 2–3 equal-length sub-exposures.

There are fewer NUV measurements of the Mg II region. For A, there are only five E230H-2812 and two E230H-2713, all taken with the $31'' \times 0.05''$ NDC neutral-density filtered long slit; and for B, six E230H-2713 exposures with the $0.2'' \times 0.09''$ spectroscopic slit, and one with the $0.1'' \times 0.03''$ "Jenkins" aperture (paired with the first E140M in 2010.5). These shorter NUV observations all were single exposures. There also are several E230H-2762 and E230H-2862 exposures of B, and one E230H-2762 of A, taken through other ND-filtered slits. Moreover, a number of B's other NUV exposures, and one of A's, were blank; owing mainly to Guide Star re-acquisition failures, causing the target to fall outside the STIS aperture, or the STIS shutter to remain closed. For the sake of homogeneity, only the E230H-2812 + E230H-2713 series of A and the E230H-2713 series of B (including the one

Jerkins-slit observation) were retained for the present analysis. The S/N in these exposures is uniformly high, averaging 50–85 per 2-pixel resolution element (resel) across each setting (except for the one Jenkin's slit spectrum of B, which has significantly lower S/N owing to poor throughput, but still adequate).

Table 3 summarizes the STIS datasets for AB considered for the present study. All the spectra were reprocessed via the MAST archive at the time of the most recent datasets (2020.4). The individual sub-exposures were subjected to a specialized echelle blaze correction, and the sub-exposures were co-added into observation-averaged spectra. The throughputs of the NDC long slit used for α Cen A, and to a lesser extent that of the spectroscopic slit for B, and certainly the low-throughput Jenkin's aperture, are somewhat variable depending on the OTA focus. Thus, the flux scales of the NUV exposures were normalized to the one with the best apparent throughput (highest total counts s^{-1}) in a 8 Å window in the red wing of the h-line centered at 2820 Å, a "continuum" band that displays low variability in solar irradiance spectra, as described in more detail later.

The STIS epochs are marked in Fig. 1: triangles for FUV, diamonds for FUV + NUV; blue for A, red for B. For both α Cen stars, the apparent minimum and peak of at least one X-ray activity cycle were covered by the FUV epochs. The same is true for the NUV exposures of B. However, most of the NUV observations of A fall near the peak of its cycle in the 2015–2019 time frame, which should be kept in mind for later comparisons with the Sun.

Table 3.   *HST*/STIS Pointings on α Cen AB (2010.1–2020.4)

Dataset	UT$_{\rm mid}$ (yr)	Setting	Aperture ($''\times''$)	Range (Å)	$t_{\rm exp}$ (s)	S/N
1	2	3	4	5	6	7
			α Centauri A			
ob8w01010	2010.064	E140M-1425	0.2×0.2	1140–1709	3800	13
oblh01020	2011.106	E140M-1425	0.2×0.2	1140–1709	4950	15
oblh02020	2011.410	E140M-1425	0.2×0.2	1140–1709	4950	14
obua01010	2012.163	E140M-1425	0.2×0.2	1140–1709	4275	14
obua02010	2012.764	E140M-1425	0.2×0.2	1140–1709	4275	14
oc1i10010	2013.220	E140M-1425	0.2×0.2	1140–1709	4275	14
oc1i11010	2013.668	E140M-1425	0.2×0.2	1140–1709	4275	14
oc7w10010	2014.116	E140M-1425	0.2×0.2	1140–1709	4275	13
oc7w11010	2014.561	E140M-1425	0.2×0.2	1140–1709	4275	14
ocre10010	2015.016	E140M-1425	0.2×0.2	1140–1709	1500	8
ocre10020	2015.016	E230H-2812	31×0.05NC	2667–2931	500	60
ocre11010	2015.612	E140M-1425	0.2×0.2	1140–1709	1500	9
ocre11020	2015.612	E230H-2812	31×0.05NC	2667–2931	500	60
octr10010	2016.062	E140M-1425	0.2×0.2	1140–1709	1500	8
octr10020	2016.062	E230H-2812	31×0.05NC	2667–2931	500	59
octr12010	2016.795	E140M-1425	0.2×0.2	1140–1709	1500	8
od5c10010	2017.105	E140M-1425	0.2×0.2	1140–1709	1499	9
od5c10020	2017.105	E230H-2812	31×0.05NC	2667–2931	500	64
od5c11010	2017.706	E140M-1425	0.2×0.2	1140–1709	1499	8
od5c11020	2017.706	E230H-2812	31×0.05NC	2667–2931	500	63
oduz10010	2019.492	E140M-1425	0.2×0.2	1140–1709	1750	9
oduz10020	2019.492	E230H-2713	31×0.05NC	2577–2834	500	53
odzy10010	2020.390	E140M-1425	0.2×0.2	1140–1709	1750	9
odzy10020	2020.391	E230H-2713	31×0.05NC	2577–2834	500	54

Table 3—Continued

Dataset	UT$_{\rm mid}$ (yr)	Setting	Aperture ($''\times''$)	Range (Å)	$t_{\rm exp}$ (s)	S/N
1	2	3	4	5	6	7

		α Centauri B				
ob8w02010	2010.496	E140M-1425	0.2×0.2	1140–1709	3600	9
ob8w02040	2010.496	E230H-2713	0.1×0.03	2577–2834	884	18
oblh01050	2011.107	E140M-1425	0.2×0.2	1140–1709	4950	10
oblh02050	2011.410	E140M-1425	0.2×0.2	1140–1709	4950	10
obua01020	2012.163	E140M-1425	0.2×0.2	1140–1709	4275	10
obua02020	2012.765	E140M-1425	0.2×0.2	1140–1709	4275	9
oc1i10020	2013.220	E140M-1425	0.2×0.2	1140–1709	4275	10
oc1i11020	2013.668	E140M-1425	0.2×0.2	1140–1709	4275	9
oc7w10020	2014.116	E140M-1425	0.2×0.2	1140–1709	4275	8
oc7w11020	2014.561	E140M-1425	0.2×0.2	1140–1709	4275	9
ocre10030	2015.017	E140H-1307	0.2×0.2	1196–1397	1500	5
ocre10040	2015.017	E140H-1489	0.2×0.2	1385–1586	1500	2
ocre10050	2015.017	E230H-2713	0.2×0.09	2577–2834	750	85
ocre11030	2015.612	E140H-1307	0.2×0.2	1196–1397	1500	5
ocre11040	2015.612	E140H-1489	0.2×0.2	1385–1586	1500	2
ocre11050	2015.612	E230H-2713	0.2×0.09	2577–2834	750	85
octr10030	2016.062	E140H-1307	0.2×0.2	1196–1397	1500	5
octr10040	2016.063	E140H-1489	0.2×0.2	1385–1586	1500	2
octr10050	2016.063	E230H-2713	0.2×0.09	2577–2834	745	84
octr12040	2016.795	E140H-1307	0.2×0.2	1196–1397	2000	6
octr12020	2016.795	E140H-1489	0.2×0.2	1385–1586	450	1
octr12030	2016.795	E140H-1489	0.2×0.2	1385–1586	862	2
od5c10030	2017.106	E140H-1307	0.2×0.2	1196–1397	1500	6
od5c10040	2017.106	E140H-1489	0.2×0.2	1385–1586	1500	2
od5c10050	2017.106	E230H-2713	0.2×0.09	2577–2834	745	83
od5c11030	2017.706	E140H-1307	0.2×0.2	1196–1397	1500	6

Table 3—Continued

Dataset	UT$_\mathrm{mid}$	Setting	Aperture	Range	t_exp	S/N
	(yr)		($''\times''$)	(Å)	(s)	
1	2	3	4	5	6	7
od5c11040	2017.706	E140H-1489	0.2×0.2	1385–1586	1500	2
oduz10030	2019.492	E140H-1307	0.2×0.2	1196–1397	2500	8
oduz10040	2019.492	E140H-1489	0.2×0.2	1385–1586	1900	3
oduz10050	2019.492	E230H-2713	0.2×0.09	2577–2834	500	67
odzy10030	2020.391	E140H-1307	0.2×0.2	1196–1397	2500	8
odzy10040	2020.391	E140H-1489	0.2×0.2	1385–1586	1900	3
odzy10050	2020.391	E230H-2713	0.2×0.09	2577–2834	500	71

Note. — Col. 2 is UT of mid-exposure. Col. 3 echelle settings: "140" are FUV, "230" are NUV; "M" is medium resolution, "H" is high; trailing 4-digit CENWAVE is in Å. Col. 4 aperture beginning in "31" is ND-filtered long slit; "0.2×0.2" is the "photometric" slot; "0.2×0.09" is default "spectroscopic" slit; "0.1×0.03" is ultra-high-resolution "Jenkins" aperture (which has a nominal throughput of 50 % at 2800 Å, but can be much lower depending on the telescope focus). Longer E140M exposures (Col. 6) were split into two equal sub-exposures for $3600 \leq t_\mathrm{exp} < 4000$ s and three for $t_\mathrm{exp} > 4000$ s. Col. 7 "S/N" is average signal-to-noise per 2-pixel resolution element (resel): more meaningful for continuum-dominated NUV; less informative for line-dominated FUV. Multiple exposures taken in the same "visit" are grouped together.
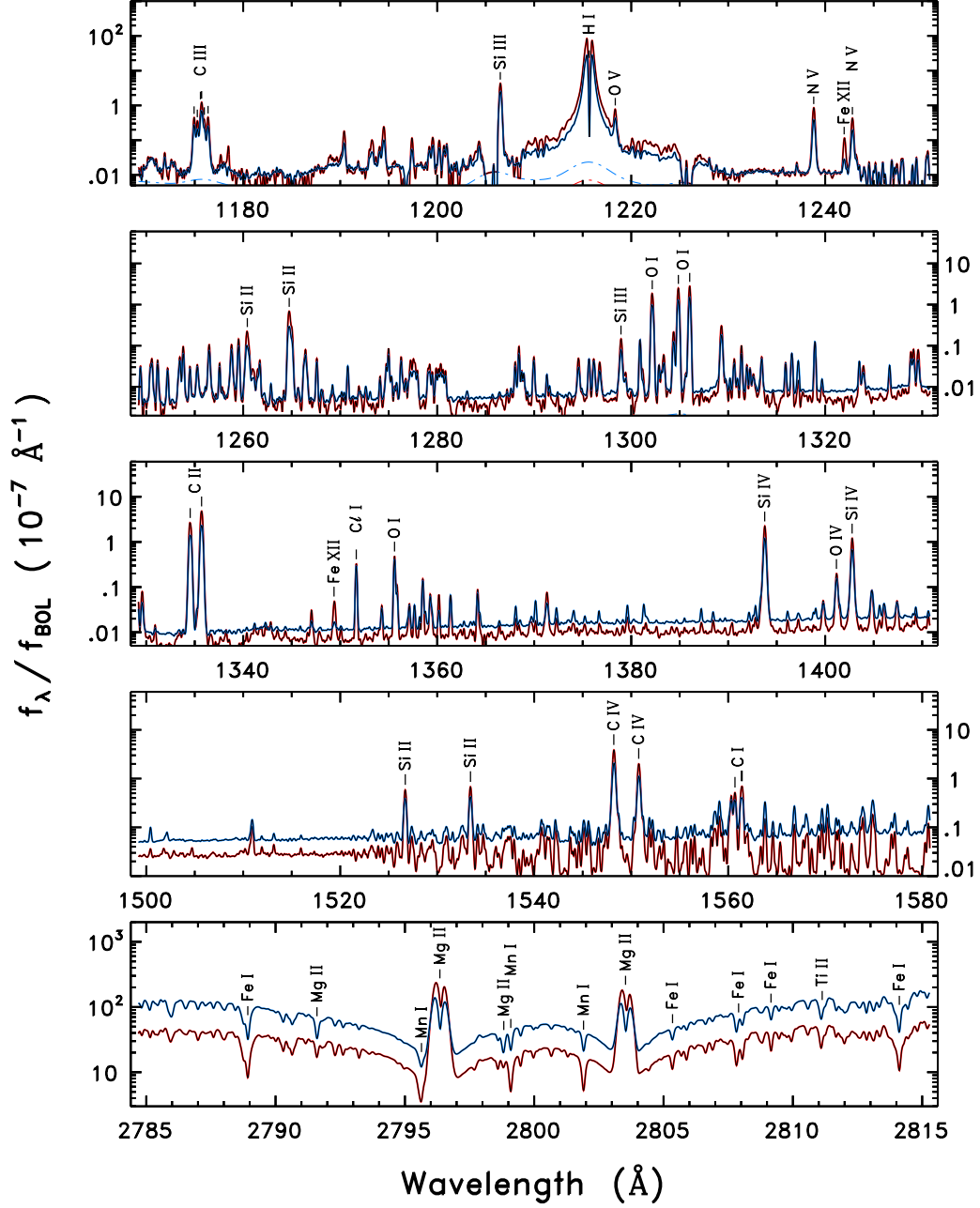
Fig. 2.— STIS epoch-average reference spectra of α Cen AB.

Figure 2 compares time-averaged STIS E140M + E230H reference spectra of α Cen AB, over selected wavelength intervals of interest to the present study, in the stellar velocity frames (as inferred from narrow chromospheric emission lines in the FUV, and photospheric absorptions in the NUV). Blue tracings are for α Cen A; red, for B. A 5-resel (10-pixel) FWHM Gaussian smoothing was applied to the original flux density spectra for display purposes. The ordinate is the bolometrically normalized flux density, $f_\lambda/f_{\rm BOL}$, which allows a fairer comparison of A and B, given the smaller size of the latter. The many decade logarithmic scale permits the strong as well as weak features to be seen. With the bolometric normalization, the peak fluxes of the B lines uniformly exceed those of A, although the FUV continuum of B, and the photospheric wings of its Mg II features, fall well below those of A, as expected given the cooler surface temperature of the K star. Note, also, that the H I 1215 Å feature completely dominates the FUV regions of AB, lording over the numerous, diverse-excitation emission species present there; but, remarkably, the NUV Mg II chromospheric cores of AB are brighter than the corresponding Lyα peaks, even though the surrounding, more elevated, NUV photospheric emission continuum diminishes the contrast, and overt significance of Mg II compared with Lyα. In fact, for low-activity stars like the Sun, the Mg II resonance lines are the dominant radiative coolants in the middle and upper chromosphere, whereas the much more opaque hydrogen resonance emission becomes important only in higher layers, at higher temperatures. In the low chromospheres of low-activity stars, where the Mg II lines are extremely optically thick, the analogous Ca II HK resonance lines near 3950 Å, and a series of Fe II resonance lines near 2600 Å, take over as the dominant radiative coolants (Anderson & Athay 1989).

A few remarks concerning the FUV + NUV spectra of α Cen AB. First, there is a broad range of ionization energy represented: from neutral species such as H I, O I, and C I ($T \sim 0.8 - 2 \times 10^4$ K); through the first and second ions, like C II, C III, and Si III ($T \sim 3-6 \times 10^4$ K); intermediate species such as lithium-like C IV and N V ($T \sim 1-2 \times 10^5$ K); all the way up to ~ 1 MK "coronal forbidden line" Fe XII. The diverse excitation energies provide the means to tune through the thermal stratification of the stellar outer atmosphere, at least in a schematic way. Second, at least two photoionization continua are visible – C I at 1245 Å and Si I at 1525 Å – represented by a series of sharp emission lines on a low background, marching toward shorter wavelengths, then giving way to an elevated, smoother plateau beyond a distinct "edge." The fact that these continua "step-up" in emission indicates formation in layers where the temperatures are rising outward, namely the chromosphere. Third, several of the prominent resonance lines, especially H I 1215 Å and Mg II hk, have sharp dips inside their emission cores produced by interstellar absorption in the tenuous gas over the short sightline between α Cen and the Sun. Additional ISM absorptions would have been visible had the spectra been displayed at full resolution and on

an expanded wavelength scale. For emission lines affected by the ISM, the integrated fluxes will be diminished somewhat; most for the very strong H I Lyα feature; intermediate for the moderate-strength resonance lines of O I and Mg II; and least for low-abundance metal lines or those of higher excitation than is typical of the conditions in the Local Cloud.

The STIS reference spectrum of α Cen A will be used later to assess the influence of the spectral degradation going from fully resolved STIS measurements to the much lower resolution of the contemporary UV solar irradiance spectrometer, ~ 1 Å *SORCE*–SOLSTICE (described in §2.2.4 later).

2.2.3.   IRIS

The Interface Region Imaging Spectrograph (IRIS: De Pontieu et al. 2014) is a NASA Small Explorer (#94), launched on a PEGASUS rocket in mid-2013. IRIS was built by the Lockheed Martin Solar and Astrophysics Laboratory (LMSAL), in Palo Alto, California, and is operated by LMSAL and NASA's Ames Research Center, in Mountain View, California. IRIS carries out long-slit stigmatic spectral imaging of the Sun's atmosphere at moderate spectral resolution ($\lambda/\Delta\lambda \sim 35{,}000$) and high spatial resolution (down to $0.33''$) in three channels: two FUV (1332–1358 Å [C II, Fe XII, Cl I, and O I] and 1390–1406 Å [Si IV, O IV]) and one NUV (2785–2835 Å [Mg II]). IRIS also obtains fast context imaging, in several broad FUV and narrow NUV bands, via slit-jaw cameras. IRIS is unique among recent solar UV spectrometers in having spectral resolution approaching that of the medium-resolution echelle modes of stellar workhorse STIS. This is valuable in the solar context for assessing the kinematic behavior of the various key spectral diagnostics in each channel, which are shaped by local flows and shock waves in the chromosphere and higher layers. But, the moderately high dispersion also allows a more direct comparison to disk-integrated stellar counterparts from STIS (e.g., α Cen AB). In the present study, IRIS imaging of Mg II in different brightness components of the quiet Sun will be used not only to highlight the general behavior of these important spectral features under varying solar conditions, but also to calibrate the hk emission core contrast-degradation in lower resolution (~ 0.6Å) irradiance scans from *SORCE*–SOLSTICE (§2.2.4).
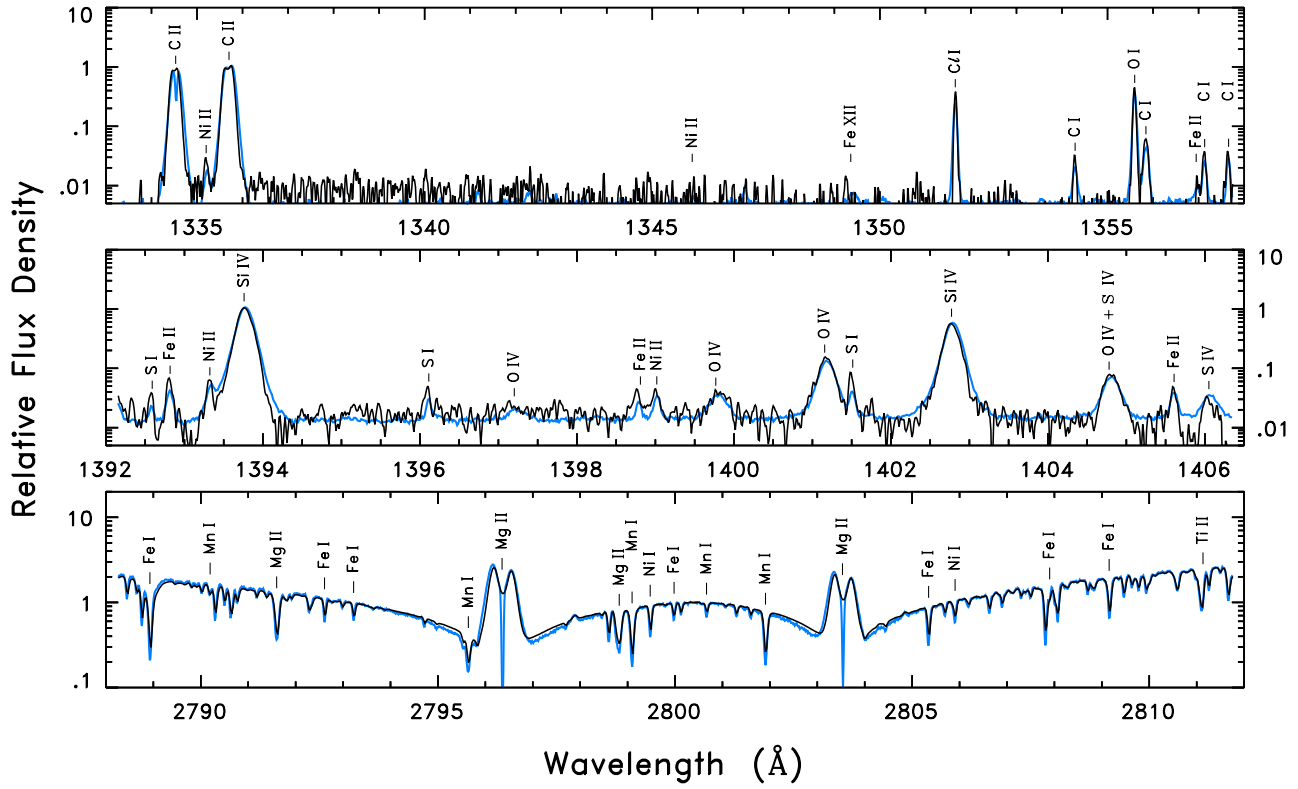
Fig. 3.— Comparison of the three channels of the IRIS solar spectrometer to the epoch-averaged STIS spectrum of α Cen A.

Figure 3 compares the three channels of an IRIS quiet-Sun observation (dark curves) to the STIS epoch-average spectrum of α Cen A (blue), in the velocity frames of the individual stars. The IRIS pointing (iris_l2_20140325_062020: "Deep exposure reference spectrum of Quiet Sun") was at an intermediate disk position ($10.3' \sim 64 \% R_\odot$ from disk center), more representative of the disk-integrated Sun than, say, a disk-center spectrum, and thus better suited for this schematic solar-stellar comparison. Each of the IRIS channels separately was normalized to the corresponding flux scale of α Cen A, and the comparison is rendered in logarithmic relative flux densities to simultaneously display the stronger and weaker features. Note the sharp interstellar absorptions in the C II 1334 Å core and in both Mg II lines, which of course are absent in the corresponding solar profiles. Other than the ISM features, the solar and stellar spectra are remarkably similar. In fact, the solar hk cores display broad central reversals like the corresponding α Cen A features; and the 1334 Å and 1335 Å emissions also show weak core reversals (as does the latter in α Cen A), which are not as evident here owing to the low contrast of the logarithmic presentation. Closer examination of the NUV channel reveals that α Cen A's Mg II inner wings, just outside the emission cores, are slightly broader than the solar features, and the numerous (mostly unrelated to Mg II) absorption lines in stellar far wings are slightly deeper than the solar counterparts. The latter effect must, at least partly, be due to the somewhat higher metallicity of the α Cen system (Table 1). The close similarity of the IRIS and STIS spectra reinforces not only the high quality of the solar instrument[2], but also the suitability of α Cen A as a solar proxy.

To calibrate the Mg II resolution degradation effect mentioned above, a set of fifteen standard IRIS "Large Coarse" 64-step rasters (each covering $2' \times 2'$ on the Sun, with a uniform exposure time of 15 s per $2''$ step for the NUV channel) was chosen from quiet-Sun pointings between disk center and the limb, away from obvious plage regions. The purpose was to construct a disk-average ("Sun as a star") spectrum that would account for systematic changes in the hk lineshapes toward the solar limb, owing to slant-angle effects on the emerging atmospheric radiation. Each raster step consisted of a long-slit spectral image of the Mg II channel (2785–2835 Å: "λ" [x-axis] direction), with approximately $0.4''$ resolution ($0.166''$ spatial pixels) along the slit ("y" direction). In these Coarse Rasters, the slit steps (orthogonal to the y-axis) were separated by $2''$. Each step-image (in accumulated Data Numbers [DN]) was divided by the exposure time; adjusted to 1 au according to the distance of the Sun at the time of observation; then filtered along the spatial y-axis, with a 7-pixel

---

[2]For various reasons, especially the superior resolution, internal wavelength lamps and radiometric validation based on external hot White Dwarfs, together with the low-scattered-light echelle design, STIS must be considered the gold standard of astronomical UV spectrographs.

running median followed by two passes of a 7-pixel running mean, to suppress cosmic ray artifacts. The smoothing corresponds to about $1''$ in the spatial direction. The column then was resampled into $2''$ pixels in the y direction, commensurate with the horizontal raster steps. The central $86''$ of the $\sim 2'$ slit was retained, where the focus is best and to avoid a pair of fiducial wire shadows crossing the top and bottom of the field. Additionally, 50 pixels were removed in the λ-direction at either end of the frame, to avoid edge effects from the geometrical correction.

Next, the spectral image was integrated in a 1 Å wide column centered on the Mg II k line along the (re-sampled) y axis. Each of the resulting k-core intensity "y pixels" has associated with it a high spectral resolution tracing in the λ direction. The set of 64 strip images of the k-core intensities then were mapped onto a "Mg II filtergram" for each Raster. Further, a frequency distribution histogram of the k-core intensities was constructed for each Raster. The individual Mg II maps typically show arcs of small-scale bright points from the ubiquitous magnetic "supergranulation" network, on a generally smoother, dimmer, but still structured background. Each Mg II k-core histogram is roughly Gaussian in shape, but asymmetric with a steeper rise to the peak, then a more gradual fall-off toward higher intensities, with a distinct high-intensity tail (similar to the well-known behavior of analogous Ca II 3950 Å HK [e.g., Cram & Dame 1983]).
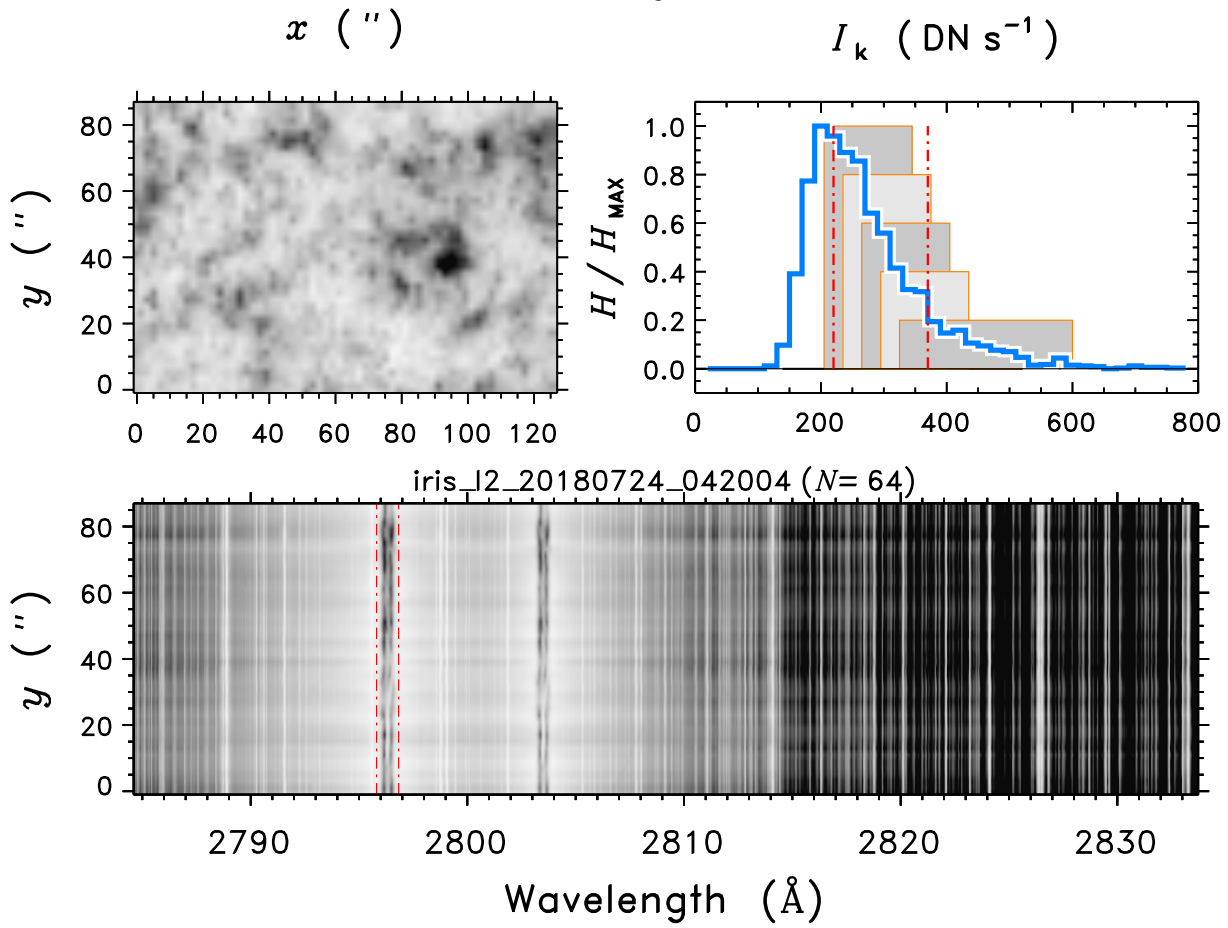
Fig. 4.— Schematic processing sequence for the IRIS Mg II channel.

Figure 4 illustrates the procedure for the last step (64th) of a Large Coarse Raster taken near disk center. Shown in the lower part is the NUV stigmatic image (darker = higher Data Numbers). The two wiggly vertical stripes flanking 2800 Å are h (to the right) and k (left). Red dot-dashed lines delimit the spatial/wavelength band in which k-line intensities were integrated, to provide a strip image for that frame. The upper left panel shows the result of concatenating the 64 strip images into a 2D spatial map (North is up, East to the left). The upper right panel illustrates the frequency distribution function for the intensities in the k-line image.

The k-line intensity histogram for each Raster initially was coarsely divided into three parts: "low-quiet" (<220 DN s^{-1}), "medium-quiet" (220–380 DN s^{-1}), and "high-quiet" (>380 DN s^{-1}). Each set of spectra corresponding to one of the three intensity bands was co-added to yield an average spectrum for that brightness level and specific Raster. These histogram-split, Raster-level spectra for the center–limb pointings then were combined into disk averages by weighting according to the areas of the associated disk annuli. Additionally, all the spectra from the fifteen Coarse Rasters were weighted and co-added into a cumulative disk-average profile (which, in fact, is very close to the histogram-split "medium-quiet" brightness level). Finally, the procedure was repeated, but further subdividing each intensity histogram into five narrower, partially overlapping brightness steps, covering the higher intensity levels, as depicted in Fig. 4. The 5-level subdivision will appear later as part of a calibration of the resolution-degradation effect on Mg II hk arising from the low (~ 0.6 Å) resolution of the *SORCE*–SOLSTICE NUV channel. The IRIS 5-step spectra will be used to simulate the behavior of the hk flux profiles as they strengthen from minimum to maximum across the solar activity cycle, taking the elevated brightness components of the spatial average as a surrogate for increasing coverage of activity as a magnetic cycle progresses toward maximum. The resolution-driven flux-redistribution effect is more pronounced for Mg II, than for the FUV emission lines, owing to the unique character of hk: narrow emission cores on top of broad damping wings of comparable intensity from the same species, which vary roughly in step with intensity changes of the emission cores. In contrast, the more isolated FUV emissions fall on generally weaker continua, contributed by processes unrelated to the line transitions themselves, and which usually are much less variable.

In addition to the detailed view of the quiet-Sun disk-average behavior of the IRIS Mg II hk features, a second set of ten IRIS Large Coarse rasters was selected from quiet regions within $\sim 2'$ of disk center, during lower phases of sunspot Cycle 24 (late-2017 through 2018), and away from obvious plage areas. The purpose of this second group was to construct a representative disk-center spectrum, split into low-quiet, medium quiet, and high-quiet components as for the disk average earlier. Finally, an additional nine 64-step pointings were culled from a larger sample of Coarse Rasters that covered areas containing significant

activity – moderately strong plage and sunspots – but also close to disk center (within $\sim 5'$). For the active set, Mg II maps and cumulative histograms were constructed in the same way as described previously. Another three reference spectra were extracted – "low-active," "medium-active," and "high-active" – again by partitioning the cumulative plage histogram, and associated spectra, into three roughly equal levels.

These "active" Mg II features are not especially pertinent to the present study, because the earlier "5-level" disk-average essentially spans the full range of global hk flux behavior across a solar cycle. The main purpose of the enhanced-activity set was for comparisons to other stars more active than the Sun. Further, the full set of low-quiet to high-active profiles is relevant to an odd property of stellar chromospheres called the Wilson-Bappu Effect (Wilson & Vainu Bappu 1957). Namely, the FWHMs of the analogous Ca II HK emission cores (near 3950 Å) broaden systematically with increasing stellar luminosity (an effect traceable mainly to surface gravity [Ayres 1979]). Yet, within a group of stars of similar luminosity, but differing activity levels, the Ca II FHWM remains roughly independent of the core emission strength. The Mg II Wilson-Bappu Effect will be discussed in more detail in a forthcoming paper of this series, for which current "Trenches I" lays important groundwork.
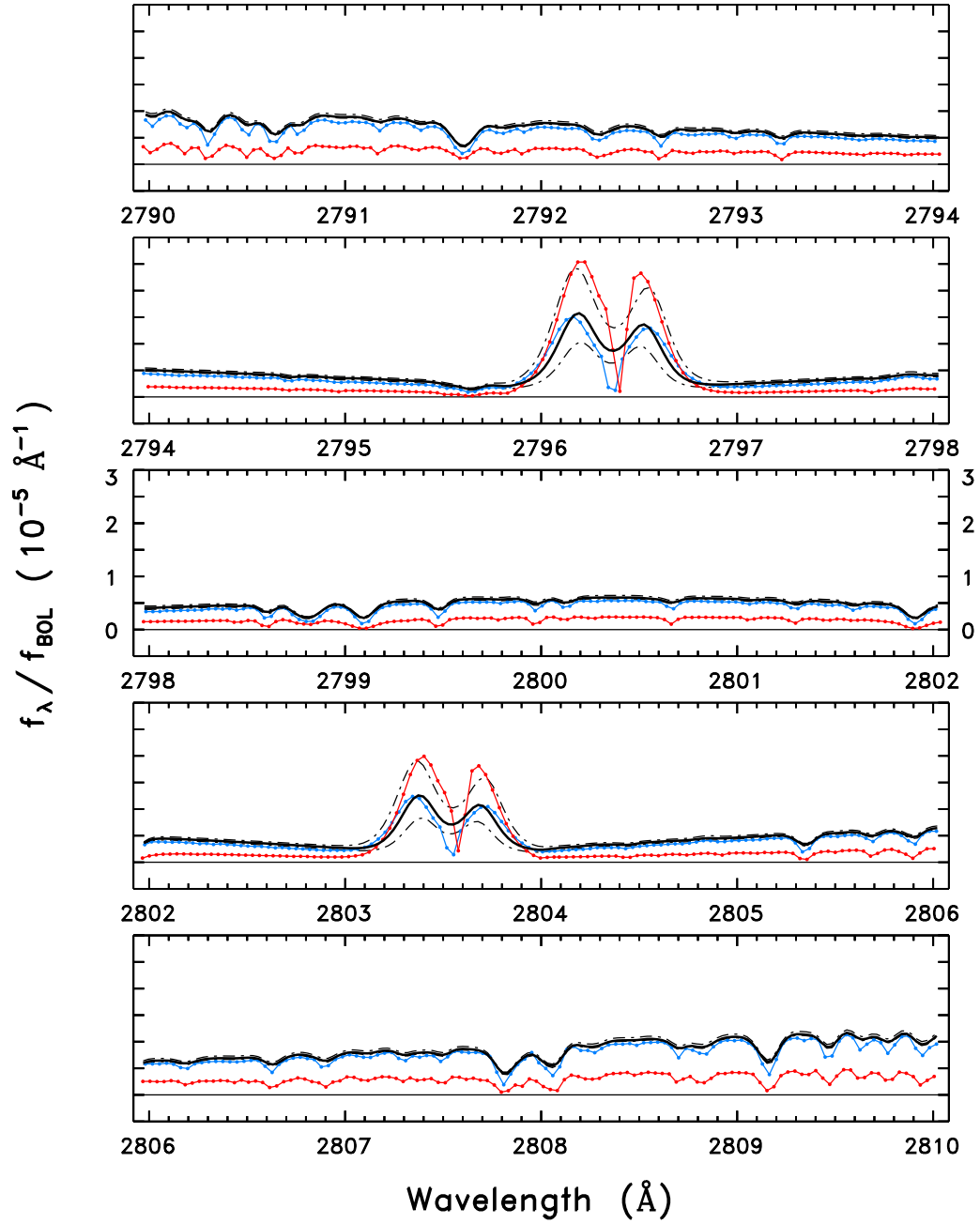
Fig. 5.— STIS stellar and IRIS solar spectra in the NUV Mg II region.

Table 4 summarizes the various IRIS datasets utilized here. Figure 5 compares the full range of disk-average Mg II quiet-Sun profiles – low-quiet (lower dot-dashed), high-quiet (upper dot-dashed), and 5-level step 2 (heavier dark curve; a good match to cycle-MIN *SORCE*–SOLSTICE, as shown later) – to the epoch-average reference UV tracings of α Cen AB (blue and red, respectively). The IRIS profiles are depicted in flux-density units (divided by the solar bolometric flux), based on a cross-calibration against SOLSTICE described in §2.3.2, below. Note, again, that more active α Cen B (in terms of $L_{\rm X}/L_{\rm BOL}$) has brighter hk cores than A (and slightly brighter than the Sun's high-quiet Mg II), but fainter damping wings, as expected from the cooler photosphere of the K dwarf. Alpha Cen A's average Mg II hk core profiles are similar to the quiet-Sun step-2 disk average, aside from the prominent ISM absorptions. Note also that the ISM absorptions of AB (which are at a fixed heliocentric velocity) fall at slightly different apparent velocities in the AB stellar reference frames, owing to the differential orbital motion of the binary pair.

Table 4.   IRIS Pointings

Dataset	UT$_\mathrm{mid}$	$(x_\mathrm{cen}, y_\mathrm{cen})$	ρ	d
	(yr)	$('', '')$		(au)
1	2	3	4	5

		Quiet Regions Away from Disk Center toward Limb		
iris_l2_20180327_042026	2018.235	$(-22.0, +251.0)$	0.262	0.998
iris_l2_20180223_043026	2018.147	$(-65.7, +260.9)$	0.280	0.989
iris_l2_20180117_044418	2018.046	$(+143.8, -298.0)$	0.345	0.984
iris_l2_20180405_041406	2018.259	$(-223.5, -245.4)$	0.346	1.000
iris_l2_20180925_042006	2018.733	$(-309.0, -123.3)$	0.347	1.003
iris_l2_20170827_071007	2017.655	$(+37.2, -369.1)$	0.386	1.010
iris_l2_20180508_042006	2018.350	$(+380.9, -54.2)$	0.401	1.009
iris_l2_20180507_042851	2018.347	$(-258.8, -358.7)$	0.461	1.009
iris_l2_20180504_042006	2018.339	$(+453.0, -118.7)$	0.488	1.008
iris_l2_20180506_041006	2018.344	$(-383.7, -347.1)$	0.539	1.009
iris_l2_20160911_043420	2016.696	$(+556.9, -345.5)$	0.683	1.007
iris_l2_20180301_194118	2018.165	$(+748.3, -166.6)$	0.799	0.991
iris_l2_20180505_042006	2018.341	$(-708.9, -330.0)$	0.815	1.008
iris_l2_20171228_102856a	2017.9916	$(+781.8, +39.5)$	0.815	0.983
iris_l2_20171228_102856b	2017.9917	$(+781.8, +40.1)$	0.815	0.983

		Quiet Regions Near Disk Center		
iris_l2_20180724_042004	2018.560	$(+61.6, +13.6)$	0.066	1.016
iris_l2_20180420_042004	2018.300	$(+1.4, +10.1)$	0.011	1.005
iris_l2_20180303_055517	2018.169	$(+6.1, +11.9)$	0.014	0.991
iris_l2_20171203_093916	2017.923	$(+10.9, +39.9)$	0.043	0.986
iris_l2_20171110_041850	2017.860	$(+11.5, +23.4)$	0.027	0.990
iris_l2_20181010_041605	2018.774	$(+3.0, +31.0)$	0.032	0.999
iris_l2_20180911_031917	2018.694	$(+106.3, +65.0)$	0.130	1.007

Table 4—Continued

Dataset	$\mathrm{UT_{mid}}$	$(x_{\mathrm{cen}}, y_{\mathrm{cen}})$	ρ	d
	(yr)	$('', '')$		(au)
1	2	3	4	5
iris_l2_20180804_041904	2018.591	$(+89.3, +14.5)$	0.094	1.015
iris_l2_20180630_042016	2018.495	$(+28.2, +14.0)$	0.033	1.017
iris_l2_20181017_042014	2018.793	$(+2.2, +59.0)$	0.061	0.997
Active Regions Near Disk Center				
iris_l2_20141214_090817	2014.953	$(+81.2, +174.3)$	0.200	0.984
iris_l2_20150224_070918	2015.149	$(-17.3, -28.0)$	0.034	0.990
iris_l2_20150409_043810	2015.270	$(+5.9, +237.1)$	0.247	1.001
iris_l2_20150421_045916	2015.302	$(+214.5, +171.9)$	0.286	1.005
iris_l2_20150705_105021	2015.508	$(+92.3, +144.1)$	0.178	1.017
iris_l2_20150719_045230	2015.546	$(+115.9, +79.0)$	0.146	1.016
iris_l2_20150920_050328	2015.719	$(+104.6, +95.4)$	0.147	1.004
iris_l2_20151119_185417	2015.884	$(+155.9, +128.5)$	0.210	0.988
iris_l2_20160906_061709	2016.683	$(+28.4, +16.1)$	0.034	1.008

Note. — Col. 2 is UT of mid-observation. Col. 3 provides the pointing coordinates in solar "x" and "y". Col. 4 is fractional distance of pointing from disk center ($\rho = 0$) to the limb ($\rho = 1$). Col. 5 is distance of IRIS (Earth) from the Sun, in units of the mean distance, at the time of observation.

Although not illustrated here, the IRIS pseudo-disk-average step-2 Mg II "flux" profile shows a roughly similar, though slightly more symmetric, core than the quiet-Sun disk-center whole-histogram average. At the same time, the outer wings of disk-average hk are lower than the disk-center reference (when expressed in equivalent flux units). This is because the whole-disk averaging geometrically favors the outer annuli, where the emergent intensities are affected by "limb darkening." Namely, the slant-angle line-of-sight forces the optically thick wing radiation to arise at higher altitudes where, normally, the temperatures are cooler (at least in the photosphere, where the local thermal profile is trending lower outward).
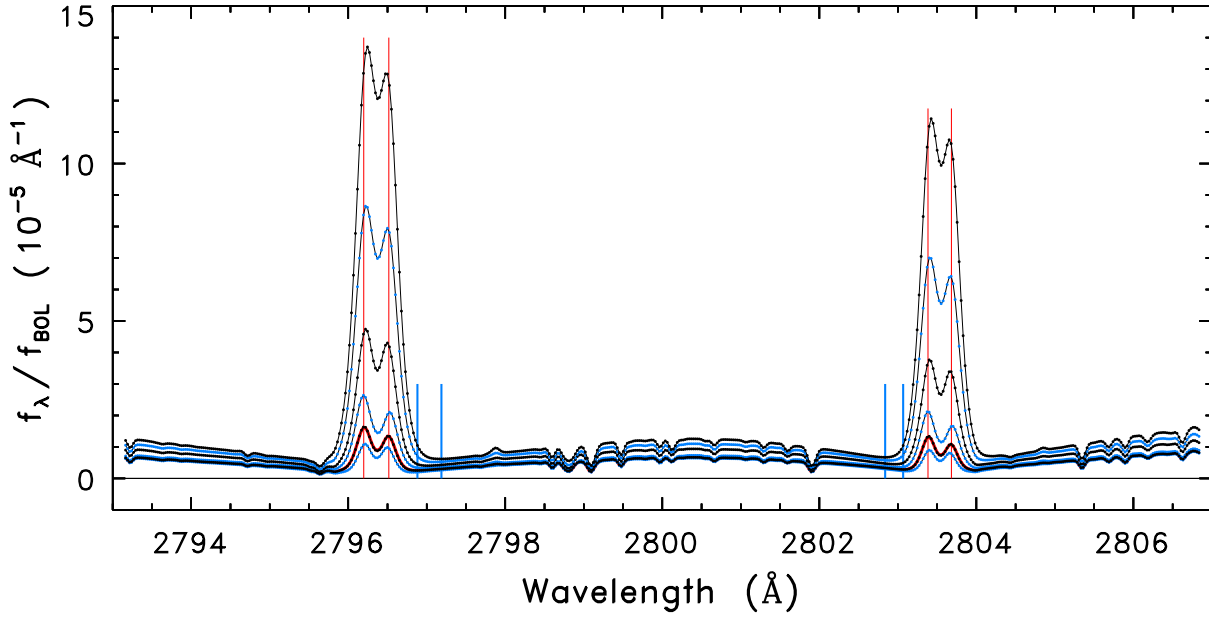
Fig. 6.— IRIS Mg II profiles of the quiet Sun and active plages near disk center.

Figure 6 illustrates the full range of disk-center Mg II profiles from low-quiet to high-active. The heavy red curve is the full-histogram average quiet-Sun spectrum; blue dotted tracings immediately below and above are low-quiet and high-quiet; and the dark-dotted curve, on top of the red tracing, is the medium-quiet profile. The three brighter plage profiles are (from top down): high-active, medium-active, low-active. Thin vertical red lines mark the "h_2" and "k_2" emission peaks of the medium-quiet cores; shorter blue lines mark the "h_1" and "k_1" minimum features of medium-quiet (closer to the line centers) and high-active (farther out). In the plage regions, the hk cores brighten systematically, and so do the inner wings (a similar behavior was noted in plage profiles of Ca II HK by Shine & Linsky 1972). At the same time, the minima on either side of the hk cores appear to move apart with increasing core intensity, indicating that the activity-associated heating is affecting progressively deeper, denser layers of the upper photosphere. Curiously, however, the "k_2" and "h_2" peak separations are roughly independent of the core intensities, and, if anything, become slightly narrower in the most active plage profiles.

2.2.4. SORCE

The Solar Radiation and Climate Experiment (*SORCE*: Rottman 2005) is a NASA-supported small satellite designed to make high-precision measurements of the total solar radiation (the "bolometric flux" or "irradiance"), and spectrally resolved bands relevant to photochemical, ionization, and direct heating processes; variously important to understanding short-term terrestrial atmospheric changes and long-term climate evolution. *SORCE* was launched in early 2003 on a PEGASUS rocket (like IRIS), and ran for 17 years until early-2020 when a variety of spacecraft subsystem issues – mainly failing batteries – terminated routine operations. Earlier battery anomalies caused a six-month gap in data collection between 2013 July and 2014 February, but otherwise the measurement series is continuous from 2003–2020, covering the decline of solar Cycle 23 and the rise and fall of Cycle 24. *SORCE* carries four instruments to measure the solar output, two of which – SOLSTICE and XPS – are central to the present study. These are described separately below. All of the *SORCE* irradiance measurements are quoted for the mean solar distance of 1 au; and a correction for the total motion (satellite plus Earth) relative to the Sun has been applied to the spectrally resolved measurements.

SOLSTICE

The Solar-Stellar Irradiance Comparison Experiment (SOLSTICE[–II]: McClintock et al. 2005) is a broad-band, high dynamic range, photomultiplier-based, scanning spectrometer that records low-resolution, high photometric precision spectra in two independent UV channels (here designated "FUV" and "NUV" to be compatible with STIS) that together cover the same range, 1150–3200 Å, as the *HST* STIS echelles. The SOLSTICE spectral resolution (FWHM), as measured here relative to resolved STIS α Cen A and IRIS, is about 0.9 Å in the FUV and somewhat better, 0.6 Å, in the NUV (at 2800 Å).

A unique aspect of SOLSTICE, as alluded by its proper name, is that it targets on a regular basis a few dozen UV-bright hot stars scattered around the Ecliptic, to empirically track any changes in the instrumental sensitivity over time. In early-2006, the SOLSTICE-B NUV channel suffered an anomaly when the slit-changing mechanism (which toggles between the large stellar and small solar apertures) became stuck in the solar position. The SOLSTICE-A FUV channel was not affected. Ironically, the new slit orientation apparently slightly improved the spectral resolution of SOLSTICE-B's NUV channel. This was inconsequential for the absolute fluxes, owing to the frequent self-calibrations (based on a redundant set of spectrometers exposed to sunlight only occasionally), but had a small influence on the Mg II measurements, as described below, which otherwise would not have been noticeable

except for the extremely precise high-S/N photometry delivered by the instrument.

SOLSTICE spectra were obtained from the LASP Interactive Solar Irradiance Data Center (LISIRD)[3] hosted by the Laboratory for Atmospheric and Space Physics at the University of Colorado, Boulder, the organization that built the *SORCE* instruments and operated the mission. The high-level spectra are provided with a uniform sampling of 0.25 Å. For the present study, SOLSTICE daily scans (Level 3, Version 17) for the years 2003.5–2020.0 were utilized. These cover the declining phase of Cycle 23, and most of subsequent Cycle 24. Nevertheless, these cycles are relatively modest compared with previous ones, especially in mid-20th Century (Cycle 24's maximum Sunspot Number was just over 100, while Cycle 19's [circa 1959] was nearly 300).

---

[3]see: http://lasp.colorado.edu/lisird/data/sorce_solstice_ssi_high_res/.
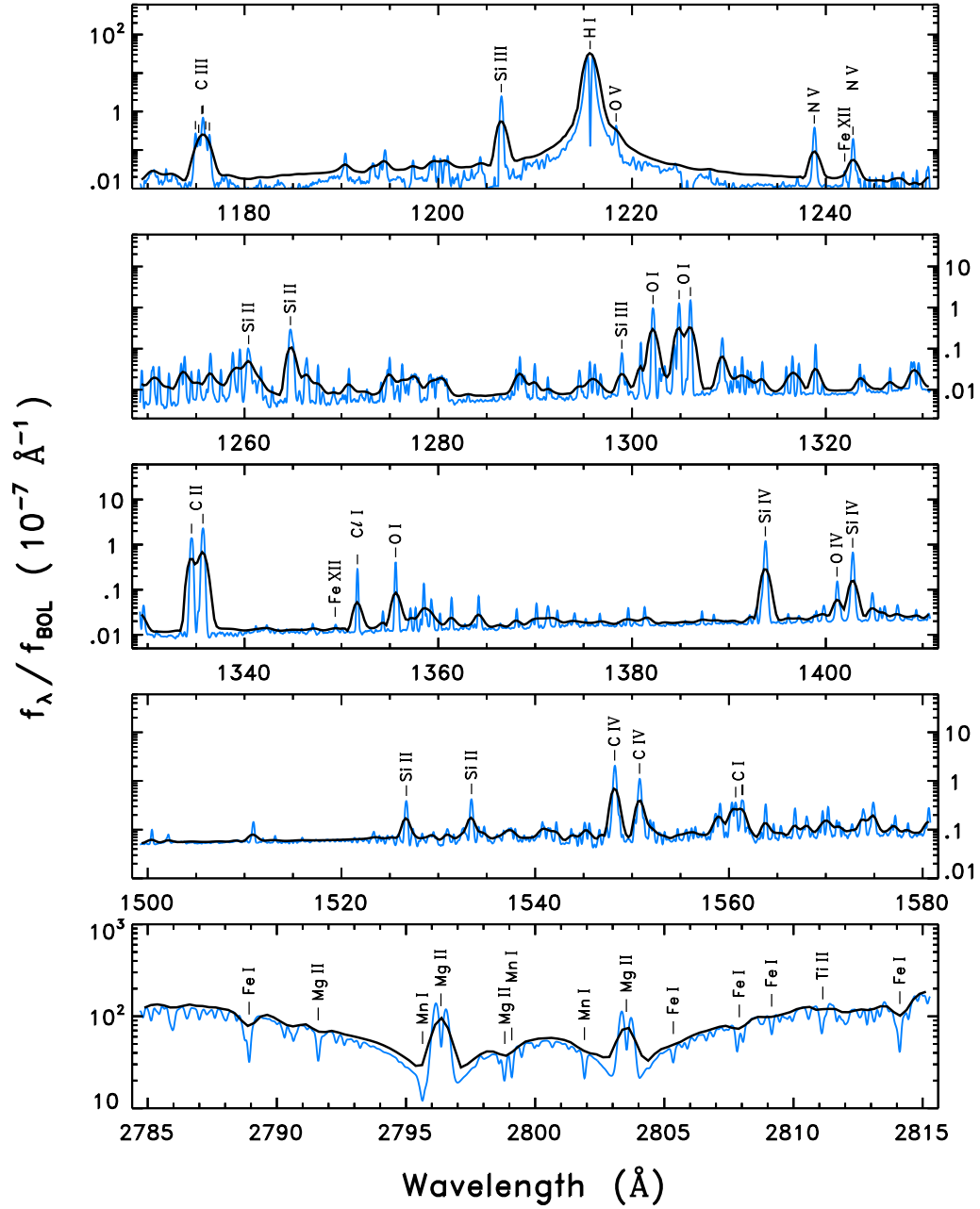
Fig. 7.— Comparison of SOLSTICE spectrum near solar cycle MIN to the higher resolution STIS reference spectrum of α Cen A.

Figure 7 compares selected wavelength intervals of a SOLSTICE tracing (dark curve: average of daily scans 2008.7±0.3 during a period of reduced solar activity during the minimum between Cycles 23 and 24) to the STIS reference spectrum of α Cen A (blue curve). The much lower resolution of SOLSTICE has a conspicuous impact on the overall spectrum, causing line pairs normally separated at STIS resolution, like O I 1304 Å + 1306 Å or C II 1334 Å + 1335 Å, to be partially blended in the solar scans. At the same time, there are relatively isolated features at STIS resolution, like Si III 1206 Å, Cl I 1351 Å, and Si IV 1393 Å, which still appear isolated in the SOLSTICE tracing. Most of these features would have a relatively small correction for the systematic degrading effect of the lower resolution, typically < 10 % as demonstrated later. The important exception is the Mg II doublet, shown in the bottom panel of Fig. 7. The $\sim 25\times$ lower resolution of SOLSTICE has redistributed some of the core flux into the line wings, elevating them at the expense of the core. This has a significant impact on the specialized approach to measure these features (as described in §2.3.1 later).

XPS and FISM2

The XUV Photometer System (XPS: Woods & Rottman 2005) is a compact device on *SORCE* that mainly monitors the high-energy output of the Sun below about 340 Å, but includes a longer-wavelength channel to capture super-bright H I 1215 Å Lyα. The irradiances are measured by means of a dozen diode photosensors set behind a filter wheel. The diodes have relatively low spectral resolution, typically about 70 Å, dictated by the filter responses, but the highest energy passband covers the 6.2–62 Å range (0.2–2 keV) commonly quoted in stellar X-ray astronomy (heritage of *ROSAT* [*Röntgensatellit*: Truemper 1982], the most prolific X-ray observatory prior to *Chandra* and *XMM-Newton*). The cited XPS accuracy is 12–30 % absolute, depending on the diode, and the long-term repeatability is an excellent 1% per year. The XPS daily data (Level 4) also are available through LASP[4], but a derivative product, called the Flare Irradiance Spectral Model (FISM), proved to be more useful in the present study.

FISM2 (upgraded version of original FISM) is a moderate-resolution observationally motivated, but ultimately model-derived, description of the Sun's daily high-energy emissions from 0.5–1900 Å tabulated in 1 Å bins. The data product is based on a *CHIANTI* (e.g., Dere et al. 2019) plasma spectral model adjusted to fit a variety of observational constraints, mainly the *SORCE* XPS L4 diode count rates for the soft X-ray energy range of interest here. The full FISM2 description has not been published yet, but the general strategy of the

---

[4]see: http://lasp.colorado.edu/home/sorce/data/

previous version was described by Chamberlin et al. (2008). The utility for "Trenches" is that FISM2 accomplishes the tricky conversion of the broad-band diode measurements into the stellar 0.2–2 keV reference soft X-ray band, taking into account the laboratory assessments of the various, partially redundant, filter responses. FISM2, which incorporates a number of improvements over the original FISM, shows some significant differences in the solar X-ray fluxes, especially for the minimum periods of Cycles 23 and 24, when the spectrum would have been very soft. For the present study, FISM2 daily spectra were numerically integrated over 6.2–62 Å to provide solar X-ray fluxes at 1 au in the reference "*ROSAT*" energy band.
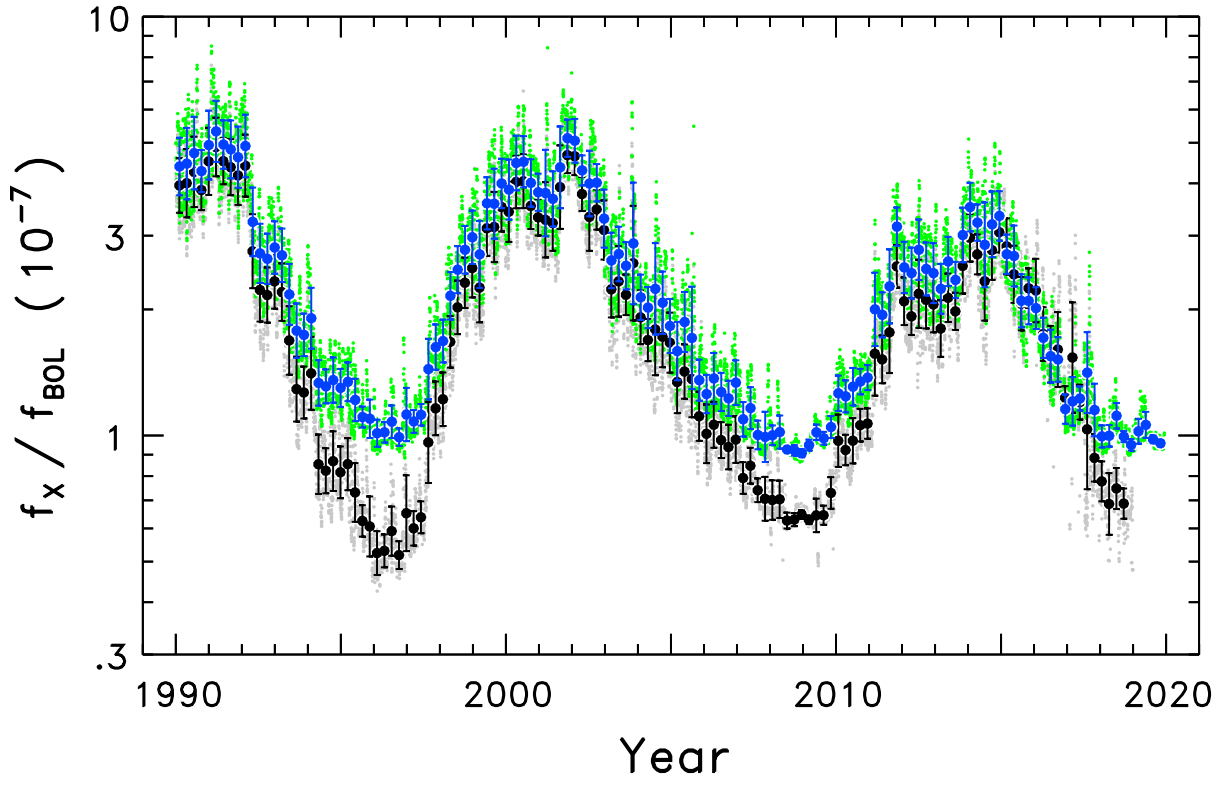
Fig. 8.— New FISM2 solar X-ray fluxes compared to previous FISM.

Figure 8 compares the new FISM2 solar X-ray fluxes to original FISM over a time period relevant to the multi-decadal X-ray campaigns on α Cen AB described earlier. The FISM2 daily fluxes are in green, while the connected blue dots are 81-day averages (3 synodic solar rotations); error bars are standard deviations of the daily values over each 81-day bin. The previous FISM fluxes are shown in gray (daily values) and darker dots (81-day averages). The new FISM2 fluxes are about 10–20 % higher at the cycle MAXs, but up to 50 % higher at the MINs, thereby reducing the Sun's soft X-ray MAX/MIN contrast to about 5, roughly the same as seen in the α Cen B X-ray cycles over the past 25 years. For "Trenches," the relevant time period is that of the *SORCE* mission, 2003.5–2020.0, so the UV measurements from SOLSTICE can be compared directly with their higher energy counterparts from XPS (as translated through FISM2). For the pre-*SORCE* time period, and during the 6-month *SORCE* "battery gap," 2013.4–2014.1, the FISM2 modeling was based on precursor versions of XPS flown on earlier irradiance platforms (some still operating), or extrapolations from various coronal proxies like the 10.7 cm solar radio flux. The "filling" of these periods by non-XPS measurements has no consequences for "Trenches," because only those XPS-based X-ray fluxes that specifically have contemporaneous UV measurements from SOLSTICE were utilized in the present analysis.

2.3.   Measurements, Cross-Calibrations, and Corrections

There were three general classes of assessments performed for "Trenches:" (1) Line-flux measurements via numerical integrations; (2) IRIS/SOLSTICE NUV cross-calibration; and (3) corrections to compensate for the low resolution of the SOLSTICE scans. These three, partially overlapping, assessments are described, in turn, below.

2.3.1.   Line Flux Integrations

The first assessment type is quite simple, though fundamental: emission line flux measurements in the SOLSTICE daily scans, and the various STIS epochs for α Cen AB. The resulting collections are the raw material of flux–flux comparisons analogous to those described earlier for the historical stellar samples. A straightforward approach to these measurements was taken, namely numerical integrations of the flux densities, above a fitted continuum level, between pre-determined wavelength limits (which, however, were allowed to differ for the solar and stellar cases). For additional simplicity, in cases where a line pair was resolved by STIS but not by SOLSTICE, the STIS integration limits were chosen to be similar to those for SOLSTICE, i.e., measuring the line pair together rather than separately.

Direct numerical integration was favored over more complex schemes, for example single- or multiple-Gaussian modeling, because the fundamental interest here was the line fluxes rather than the detailed profile shapes (which are known to be distorted by a variety of velocity effects in the case of α Cen AB [see, e.g., Ayres 2015]). In any event, there would be no such velocity information easily forthcoming from much lower resolution SOLSTICE.

Table 5 lists the target species and integration parameters utilized for the STIS spectra of the α Cen stars and for SOLSTICE. The broad-band FUV continuum level in the STIS spectra was set by clipping and heavily smoothing the observed flux densities with a series of filters: first a running median of 71 wavelength bins (35 resels), then a running minimum of width 101 bins, and lastly two passes of a running mean of width 71 bins. The multi-step filtering removes the narrow emission lines, leaving behind a smooth trace that closely follows any long-range persistent backgrounds (normally the major FUV photoionization continuua mentioned earlier). A similar filtering scheme was applied to the SOLSTICE FUV scans, but with widths more suitable to its resolution and sampling: 21 bins, 31 bins, and 31 bins, respectively, for the three filters described above.

Table 5.   Line Flux Integration Parameters

Feature	$\log T_{\mathrm{MAX}}$	λ_{cen}	$\Delta\lambda$	λ_{cen}	$\Delta\lambda$	R-Comp	Contin?
		— STIS —		— SOLSTICE —			
	(K)	(Å)	(Å)	(Å)	(Å)		
1	2	3	4	5	6	7	8
CIII-1175	4.8	1175.700	1.000	1175.700	1.750	0.976	Y
SiIII-1206	4.7	1206.550	0.300	1206.600	1.250	1.011	Y
HI-1215	(4.3)	1215.700	2.000	1215.700	2.000	0.999	Y
NV-1238	5.2	1238.850	0.375	1238.900	1.150	0.961	Y
FeXII-1241	6.2	1241.985	0.190	$\cdots$	$\cdots$	$\cdots$	Y
NV-1242	5.2	1242.825	0.250	1242.950	1.000	0.849	Y
OI-1302	(3.9)	1302.175	0.275	1302.200	0.850	1.005	Y
OI-1305	(3.9)	1305.450	0.850	1305.500	1.750	0.965	Y
CII-1335	4.5	1335.150	0.950	1335.250	1.900	0.999	Y
FeXII-1349	6.2	1349.400	0.190	1349.400	1.000	0.749	Y
ClI-1351	(3.8)	1351.650	0.175	1351.700	1.100	1.010	Y
SiIV-1393	4.9	1393.800	0.350	1393.850	1.300	0.958	Y
SiIV-1402	4.9	1402.775	0.350	1402.850	0.850	1.027	Y
c1506	(3.8)	1506.000	2.500	1506.000	2.500	1.000	N
CIV-1548	5.0	1548.225	0.350	1548.250	1.200	0.947	Y
CIV-1551	5.0	1550.800	0.300	1550.730	0.950	0.918	Y
MgII-2796	(3.9)	2796.350	0.500	2796.375	0.775	[a]	c2796[b]
MgII-2803	(3.9)	2803.550	0.450	2803.475	0.650	[c]	c2803[d]
c2820	(3.7)	2820.000	4.000	2820.000	4.000	1.000	N

Note. — Col. 1 is the short name of the measured feature, possible multiple. Col. 2 is the approximate temperature of maximum emissivity from *CHIANTI* (see: https://www.chiantidatabase.org/chianti_linelist.html); parenthetical values are estimates for species that form in the chromosphere or photosphere. Flux integration

bandpass (Cols. 3 and 4 for STIS; Cols. 5 and 6 for SOLSTICE) is $\lambda_{\mathrm{cen}}\pm\Delta\lambda$. In Col. 8, "Y" means that a continuum level was subtracted; "N" means no continuum subtraction. For Mg II hk, "c2803" and "c2796" are the "block" fluxes below the h and k local minimum features, respectively; whereas the h and k "core" fluxes ("MgII-2803" and "MgII-2796," respectively) were integrated above the local minima (see Figs. 9a–c). Col. 7 is a flux correction factor that compensates for the lower resolution of SOLSTICE compared with STIS. The analogous correction factors for the Mg II hk core fluxes above the minimum features, and the block fluxes below the minimum features, are given by power laws, $R_{\mathrm{X}} = R_0 \times (f_{\mathrm{X}}/f_0)^{\alpha}$, where f_{X} is the measured SOLSTICE f/f_{BOL} in units of 10^{-5} for species "X," and the other parameters (post-2006.07 values) are listed below (the empirical power laws are illustrated in Fig. 11, to be presented shortly):

[a] Mg II k: R_0= 1.150; f_0= 0.527; α= −0.02

[b] c2796: R_0= 0.545; f_0= 0.428; α= −0.08

[c] Mg II h: R_0= 1.424; f_0= 0.283; α= −0.24

[d] c2803: R_0= 0.518; f_0= 0.458; α= +0.54

The NUV regions of both STIS and SOLSTICE were treated somewhat differently, given the unique nature of the Mg II resonance lines, whose local "background continuum" is controlled by the partially blended photospheric damping wings of hk themselves. In fact, fitting the hk lines raises a philosophical dilemma. The immediate temptation is to identify the Mg II cores, above a level set by the k_1 or h_1 local minimum features, as the appropriate line flux measurement, hopefully to isolate the desired chromospheric radiative emission component. However, Linsky & Ayres (1978) showed that part of the flux in the "block" *under* the hk minimum features represents legitimate chromospheric emission. In the absence of a chromospheric temperature rise, the outward declining temperatures expected in Radiative Equilibrium (RE) would produce strong "absorption" cores in both Mg II lines, so that any excess flux above that deep absorption but below the k_1 or h_1 level presumably would represent genuine emission originating inside the chromosphere itself. The Linsky & Ayres finding, however, was based on simplistic 1-D modeling of the chromosphere and RE background atmosphere, without accounting for the dynamical effects inherent in modern 3-D radiation-MHD simulations (e.g., Martínez-Sykora et al. 2009). Because the near-UV Mg II lines respond strongly to small temperature fluctuations (in the Wien limit), the predictions of a thermally diverse 3-D simulation could be quite different from those of a thermally more monotonous 1-D RE model. Thus, it is not clear how much of the h or k "block flux" might be contributed by chromospheric heating versus normal overshooting convective dynamics (a "photospheric" phenomenon). Indeed, an important part of the Mg II core emission, itself, likely arises from shock waves produced ultimately by photospheric kinematics (cf., Carlsson & Stein 1995, 1997), rather than high-altitude magnetic heating. It then becomes largely a question of semantics to assign this or that part of the Mg II emission to a "true" chromospheric component. (And, of course, there is the larger question of exactly what the "chromosphere" is in the first place [see, e.g., Carlsson et al. 2019].)

The straightforward solution to the dilemma was simply to ignore it, and retain the core flux above the minimum features, and the block flux below them, separately. At worst, the core flux is an underestimate of the true chromospheric emission component, while the sum of the core flux and block flux must be an overestimate.

In practice, the h_1 or k_1 level for the STIS high-resolution NUV spectra was determined by identifying the minimum flux density in a 0.5 Å wide window centered on the expected position of the feature, in the red wing of k and blue wing of h, in each case less affected by extraneous absorption features unrelated to Mg II than the opposite wing. The core flux, and block flux, then were integrated in a fixed wavelength bandpass compatible with the full range of Mg II profiles encountered in the AB epochs. For the lower resolution SOLSTICE spectra, the corresponding h_1 and k_1 finding windows were restricted to just two wavelength points: whichever of these had the minimum flux then dictated the h_1 or k_1 level (and the

choice would flip-flop with changing activity). The core flux above the derived minimum, and the block flux below it, then were integrated in fixed bands that included a specific number of wavelength bins: six for h and seven for k. All these restrictions were found necessary to accommodate the subtle changes of the high-S/N SOLSTICE Mg II profiles over the solar cycle, especially across the boundary in early 2006 when the SOLSTICE-B NUV aperture mechanism became permanently stuck in the solar position, which then very slightly affected the apparent spectral resolution of that channel.
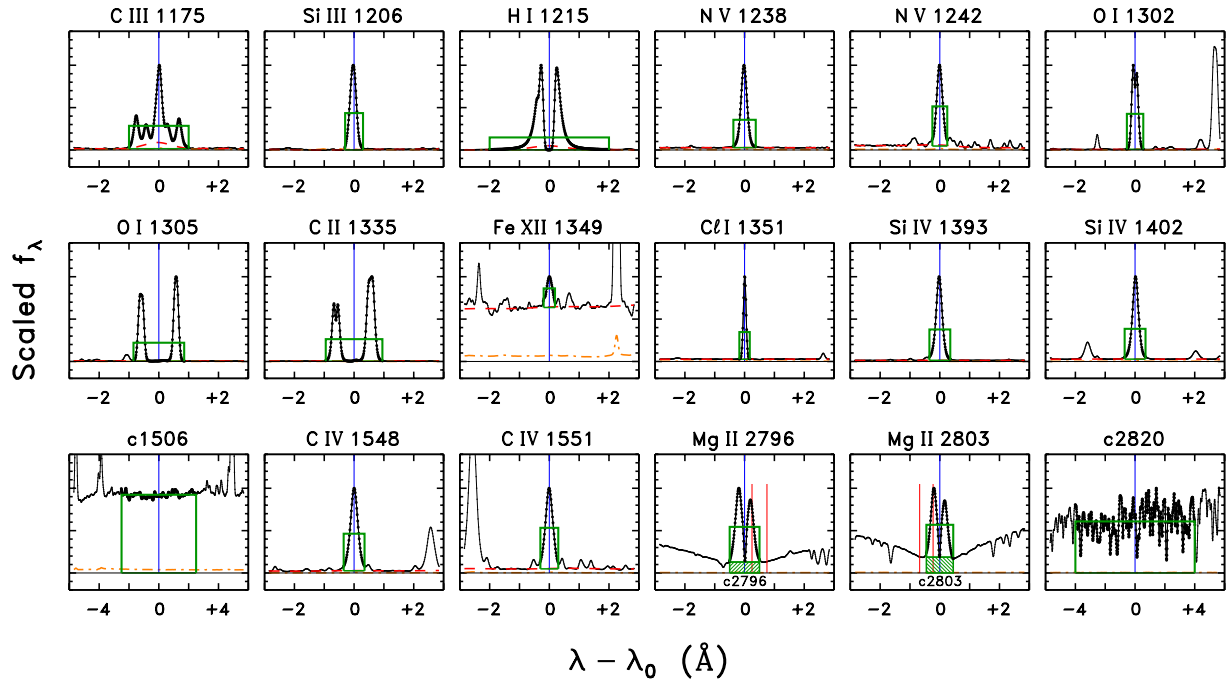
Fig. 9a.— Numerical flux integration scheme applied to the STIS reference spectrum of α Cen A.

The numerical integration strategy is illustrated in Figure 9a for α Cen A's epoch-average reference spectrum, Fig. 9b for α Cen B's epoch-average, and Fig. 9c for a representative, albeit high-activity, SOLSTICE average (from 2014.9$\pm$0.1). In each sub-panel, the observed spectrum is the connected dark dots; the photometric error curve is orange dot-dashed (mostly barely visible for the high S/N α Cen epoch-averages; not plotted for very high-S/N SOLSTICE). The filtered long-range background continuum level is the red dashed curve. Integration limits are indicted by a green box: lower boundary is the adopted continuum level, left and right sides are wavelength integration bounds, and the upper edge represents the average flux density level over the feature (for illustration). Mg II hk were divided into "core" and "block" emissions separated at the "h_1" and "k_1" features, set by the minimum flux between the vertical red lines. In Fig. 9c, the solar integration wavelength limits typically are much wider than for the higher resolution stellar counterparts. For Mg II h_1 and k_1, larger red dots indicate whichever of the two restricted wavelength points was tagged for this particular average spectrum. The hk block fluxes now are larger, and the core fluxes smaller, than for the STIS examples, owing to the influence of SOLSTICE's lower resolution.

Both components of the Fe XII coronal forbidden line multiplet (1241 Å and 1349 Å) could be measured in the high-resolution STIS tracings, whereas the 1241 Å feature was too blended with N V 1242 Å in the SOLSTICE scans and only the more isolated 1349 Å component was clean enough to be extracted. The 1241 Å Fe XII fit is not shown explicitly in Fig. 9a or 9b for the α Cen stars, although the coronal forbidden line is clearly visible just to the left of the brighter N V 1242 Å profiles.

The lower right hand panels in the Figs. 9 depict an NUV continuum band, 2820$\pm$4 Å. The maximum measured 2820 Å flux of the α Cen A epochs was used to normalize all the Mg II exposures of that star, according to their individual measured 2820 Å fluxes, and similarly for B. This was done to mitigate the potentially variable throughputs experienced with the narrow spectroscopic slits and/or ND-filtered apertures that were employed for these NUV-bright stars. The long-term SOLSTICE measurements of the 2820 Å continuum (described in more detail later) show a minimal, less than 1 %, change from Solar MIN to MAX, so that continuum band can serve as a calibration "hook" for the nearby Mg II lines (the latter vary by $\sim$40 % over the cycle, at least for the Sun and the high-resolution case).
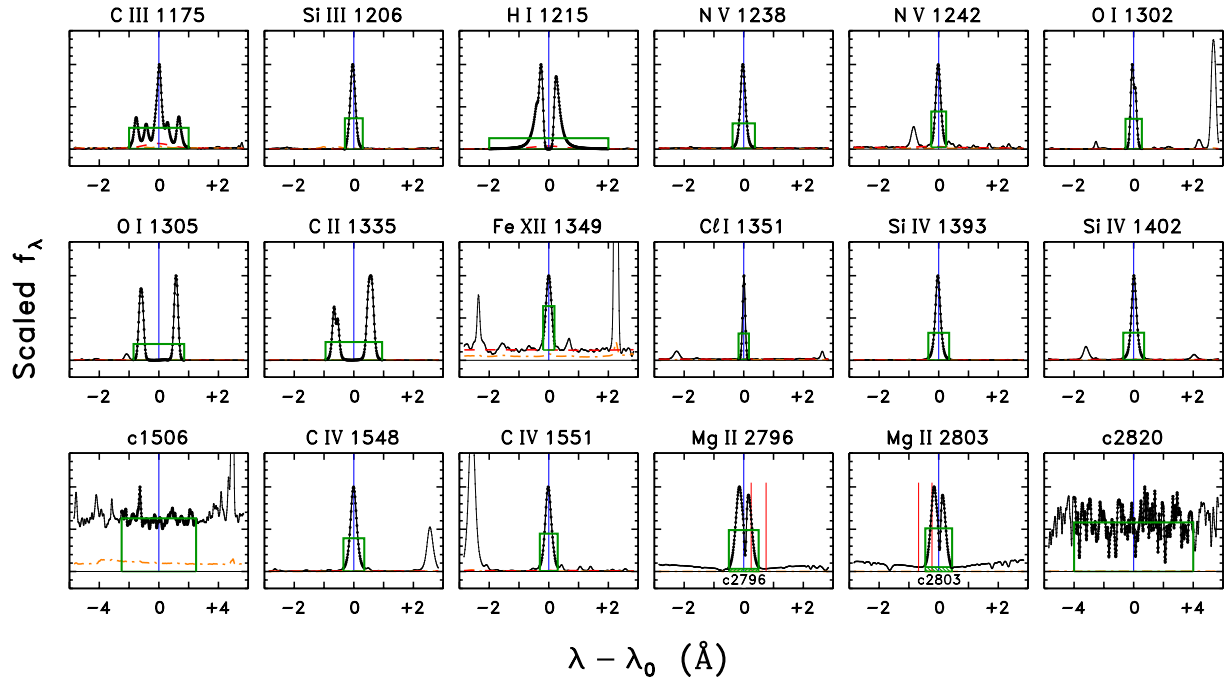
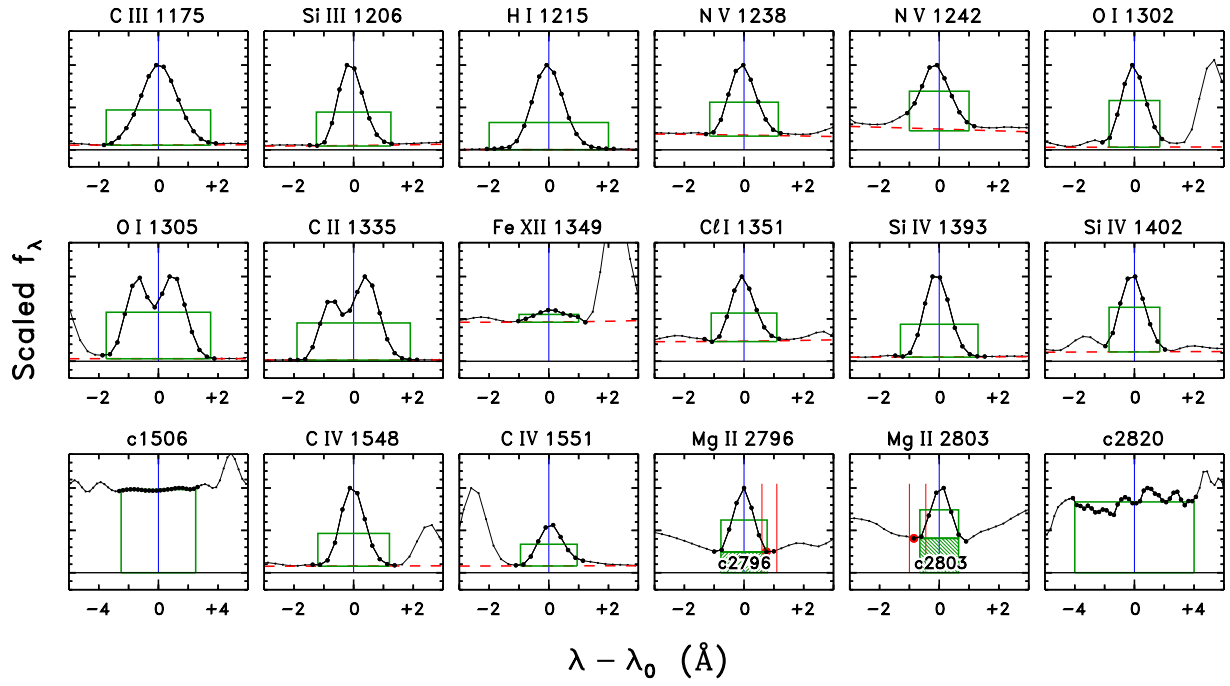Fig. 9b.— Same as Fig. 9a for STIS epoch-average reference spectrum of α Cen B.

Fig. 9c.— Similar to Fig. 9a, for a representative average SOLSTICE spectrum (near solar MAX).

2.3.2. NUV Cross-Calibration

The second type of assessment was a cross-calibration, whereby an appropriately smoothed version of the IRIS disk-average NUV spectrum was adjusted in flux density to match a SOLSTICE average (near minimum solar activity levels commensurate with the step-2 IRIS spectrum described earlier). The resulting calibration factor converts the IRIS tracings in instrumental intensities, DN s^{-1} pixel^{-1}, into flux density units, ergs cm^{-2} s^{-1} Å^{-1} (at 1 au). The scale factor subsequently was applied to the array of IRIS disk-average Mg II histogram-split profiles to calibrate them in flux-density units, so that smoothed versions would be compatible with the SOLSTICE NUV spectral irradiances. This was a key part of simulating, and compensating for, the changing spectral degradation of hk as the Mg II profiles evolve over the solar cycle.

A reference SOLSTICE spectrum was constructed for 2008.7±0.3, appropriate to the minimum between Cycles 23 and 24 (and the very quiet areas for which the IRIS spectra were collected). When the calibration originally was enforced in the far red wing of h (2820±4 Å); the SOLSTICE spectrum was systematically several percent higher than smoothed IRIS in the low-intensity region between the hk lines (2798–2802 Å), as well as shortward, down to the blue limit of the IRIS spectrum ($\sim$2786 Å). The two most obvious reasons for such a disagreement were: (1) a small amount of uncompensated scattered light in SOLSTICE, which would affect the low-intensity regions more than the higher intensity continuum band (where the normalization was enforced); or (2) a slight tilt in the IRIS response compared with that of SOLSTICE across the wavelengths in common. Both possibilities were investigated. The scattered light scenario was found to introduce significant structure into the IRIS/SOLSTICE flux ratio, especially in the inner wings of h and k; whereas the response tilt did relatively less damage to the ratio. Thus, the deviation was treated as a calibration issue on the IRIS side, and a simple response gradient of +0.25 % Å^{-1} was applied to the IRIS spectrum from 2820 Å down to the blue limit. The IRIS flux conversion then is the tilt function multiplied by the 2820 Å continuum factor (1.487 erg cm^{-2} DN^{-1} Å^{-1}).
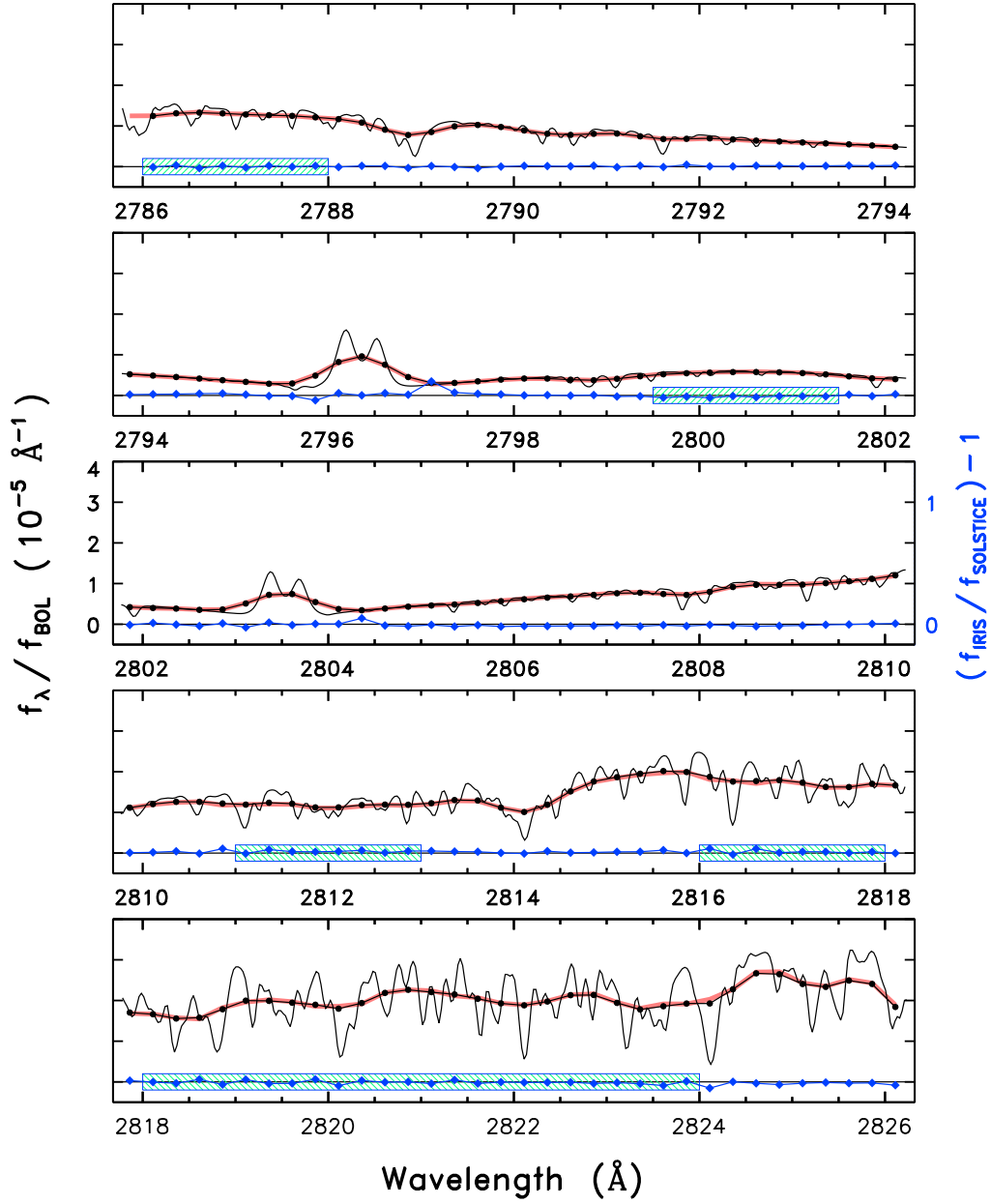
Fig. 10.— Radiometric cross-calibration of the IRIS Mg II channel against SOLSTICE-B NUV.

Figure 10 illustrates the result of the procedure. The thicker rose curve represents the SOLSTICE spectrum at cycle MIN. The thin black undulating tracing is the IRIS step-2 disk-average spectrum, corrected for the response gradient and normalized to the 2820 Å continuum flux. The connected black dots are that spectrum smoothed with a FWHM= 24 pixel Gaussian, then interpolated onto the same wavelength grid (0.25 Å spacing) as the SOLSTICE scans. The connected blue diamonds track an amplified ratio $(R - 1)$ of smoothed-IRIS to SOLSTICE-MIN. Thin horizontal blue shaded rectangles indicate reference bands to assess the cross-calibration. The two spectra are in good agreement across the 2790–2810 Å interval containing the hk emission cores and inner wings.

The STIS spectra of α Cen AB already are in flux density units like SOLSTICE. Nevertheless, there might be small offsets in the absolute scales between STIS and SOLSTICE devolving from the ways in which the independent radiometric calibrations were performed. In principal, one could examine the derived energy distributions of the SOLSTICE validation hot stars, and compare them to STIS observations of the same objects, to assess any inter-calibration offsets. Unfortunately, the SOLSTICE reference stars are so FUV-bright that STIS must employ ND-filtered apertures to avoid bright-limit violations. These ND apertures are not as well calibrated as the clear slits, and further are quite narrow, so are susceptible to variable light losses owing to thermally driven focus changes of *Hubble's* OTA. Thus, any such comparisons would be less than definitive.

Nevertheless, it is unlikely that inter-calibration systematics are larger than the $\sim$6– 8 % absolute accuracies cited for SOLSTICE[5] and STIS[6]. Further, any such offsets would be systematic, and thus would simply shift the α Cen AB integrated line flux scales relative to the corresponding solar measurements. For those species that show large intensity changes over a stellar cycle, small systematic offsets would be a minor annoyance. In fact, some level of relative offsets are expected, given that α Cen is slightly metal rich compared to the Sun. The relative compositions might be element dependent (or atmospheric dependent) as well, thus partially obscuring any legitimate inter-calibration effects. In any event, the possible calibration offsets would have no influence on the flux–flux relations for the solar measurements taken alone, for those of A or B alone, or for AB in combination.

---

[5]see: http://lasp.colorado.edu/home/sorce/instruments/solstice/science/

[6]see: https://hst-docs.stsci.edu/display/STISIHB/16.1+Summary+of+Accuracies

2.3.3. Resolution Compensation

The third type of assessment was directed toward compensating for the relatively low spectral resolution of SOLSTICE, to place the solar scans on a similar a footing to higher resolution STIS (or IRIS). For this assessment, epoch-average STIS reference spectra of α Cen A, and the various IRIS histogram-split disk-average Mg II hk tracings, were measured in the same way as in the first assessment (i.e., numerical line flux integrations); however, not only the native high-resolution datasets, but also smoothed versions to mimic the substantially lower resolution of SOLSTICE, together with re-gridding to exactly match the SOLSTICE wavelength scales. The STIS α Cen A spectra were utilized to estimate the (in most cases relatively minor) degradation effects on the more-or-less isolated FUV emission lines; while the IRIS histogram-split disk-average Mg II spectra were applied to gauge the more significant influence on hk.

The main impacts of resolution on the FUV emissions involve partly the possibility of extraneous, non-related features in the integration (noting that the typically narrower high-resolution "stellar" wavelength bandpasses might exclude features included in the broader "solar" bands); but mostly the influence on the local continuum level as set by the multi-stage filtering process described earlier. The continuum effect is relatively minor for the stronger features, although several of the weaker emissions (especially very low-contrast Fe XII 1349 Å) were more noticeably impacted. The degradation outcomes were expressed as the ratio of the high-resolution integrated flux to that measured in the smoothed spectrum, and typically were of order unity, mostly between 0.9 and 1.0 (although in some cases slightly greater than 1). These ratios then were used to multiplicatively convert the SOLSTICE daily fluxes into equivalent high-resolution values. The conversion factors are listed in Table 5 along side the SOLSTICE fitting parameters. For simplicity, the corrections, already of order unity, were assumed to be independent of the line flux.

The compensation factors for NUV Mg II hk are more complex. This is because the hk lines consist of a broad, structured emission core, normally blue-asymmetric with a shallow central reversal, partially resolved at SOLSTICE-B NUV resolution, on top of extensive wings contributed by the same species. Further, the hk cores change shape with increasing activity (as seen in Fig. 5): the hk minimum features move farther from line center as the core brightens, while the peak separations hold relatively constant. In addition, the "block flux" under the minimum features also increases as the core brightens, although not as rapidly. These effects were addressed by applying the Mg II measurement strategy (separated core flux and block flux) to the sequence of five-level histogram-splits from the quiet-Sun IRIS NUV disk average, which spans the activity range of the recent solar cycles.
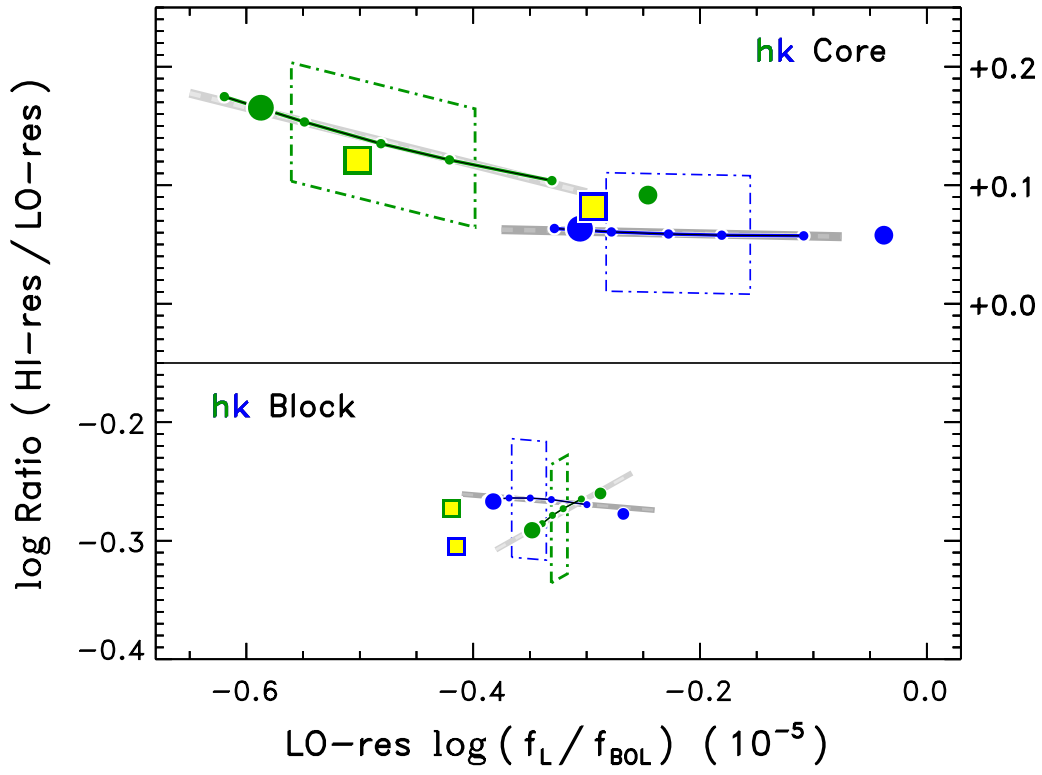
Fig. 11.— Correction factors to compensate for influence of SOLSTICE low resolution on Mg II.

Results of the procedure are depicted in Figure 11. A Gaussian FWHM of 24 pixels (0.61 Å) was applied to the IRIS spectra (this smoothing is appropriate to the SOLSTICE period 2006.07–2020.00). The upper part of the panel shows the behavior of the core-flux ratios (blue dots for k; green for h) as a function of the core fluxes (along the x-axis). The lower part is for the block-flux ratios (same color-coding), as a function of the block-flux values (also along the x-axis). Note that all the quantities are logarithmic. In absolute ratios, the core-flux corrections are ~ 1.3, and the block-flux corrections are ~ 0.5. In both panels, the smaller connected dots refer to the 5-level histogram-split IRIS disk-average profiles; larger dots at left are the full-histogram disk-averages; and larger dots at right are the high-quiet components. Thin dot-dashed trapezoids indicate (in the x-direction) the approximate span of the particular core flux or block flux (same color-coding) over the SOLSTICE time frame (last part of Cycle 23 and most of Cycle 24). Note that the empirical SOLSTICE h-line block fluxes are higher than those of the k-line, but span a narrower range; less so than might be anticipated by the IRIS histogram-split profiles.

Light gray lines indicate fitted power-law relations for h and k, core and block. Notice that the core fluxes of the full-histogram disk average (in upper part of figure) fall slightly below those of the corresponding approximate SOLSTICE MIN/MAX ranges for h and k; the block fluxes follow the same trend. In other words, the IRIS quiet-Sun disk average (specifically constructed from very quiet regions) is quieter than even solar-MIN SOLSTICE. On the other hand, the level-2 component of the 5-level histogram split (by design) is a good match for solar-MIN SOLSTICE.

Red and green outlined yellow squares represent the corresponding values for the epoch-average α Cen A NUV reference spectrum. Like the disk-average solar profiles, α Cen A's hk fall in the lower range of the cycle-spanning SOLSTICE core fluxes. To be sure, A's Mg II hk are depressed somewhat by the presence of the interstellar absorptions, but also recall that 6 of the 7 STIS NUV observations were near the apparent maximum of its cycle.

As alluded earlier, the apparent trends of the high-resolution/low-resolution ratios inferred from the IRIS analysis were expressed as power laws:

$$R \equiv (f_{\mathrm{high-res}} \,/\, f_{\mathrm{low-res}}) = R_0 (f_{\mathrm{low-res}} \,/\, f_0)^{\alpha} \qquad (1)$$

where the "fluxes" are f/f_{BOL} in units of 10^{-5} (the normalization for the SOLSTICE irradiances ingested by the measuring algorithm). Coefficients were derived separately for the pre- and post-2006.07 effective resolutions (FWHM~ 0.66 Å and 0.61 Å, respectively). The post-2006.07 relations are listed, as an example, in the "Notes" following Table 5.

Table 6 summarizes fluxes (as f/f_{BOL} in units of 10^{-7}) for the several sets of average spectra: solar-MIN (2008.7$\pm$0.3), solar-MAX (2014.9$\pm$0.1), α Cen A, and α Cen B. The

AB reference spectra are the ones illustrated in several previous figures. In the case of the SOLSTICE spectra, the resolution correction factors have been applied (important mainly for the Mg II hk core and block fluxes); and additional small corrections for time-dependent calibration inconsistencies described in the next section.

Table 6.   Fluxes from Average Spectra: Sun (Cycle MIN and MAX), α Cen A, α Cen B

| Feature | $f_{\rm L}/f_{\rm BOL}$ (10^{-7}) | | | |
| | $\odot$MIN (2008.7±0.3) | $\odot$MAX (2014.9±0.1) | α Cen A | α Cen B |
(1)	(2)	(3)	(4)	(5)
CIII-1175	0.358±0.002	0.467±0.013	0.417	0.702
SiIII-1206	0.568±0.006	0.95±0.07	0.706	1.089
HI-1215	42.7±0.3	57.4±2.0	19.0	51.0
NV-1238	0.082±0.001	0.107±0.004	0.105	0.219
FeXII-1241	$\cdots$	$\cdots$	0.0041	0.0252
NV-1242	0.043±0.001	0.059±0.002	0.051	0.105
OI-1302	0.279±0.002	0.330±0.011	0.263	0.448
OI-1305	0.594±0.003	0.699±0.021	0.645	1.143
CII-1335	1.112±0.007	1.53±0.07	1.189	2.135
FeXII-1349	0.0020±0.0002	0.0037±0.0002	0.0015	0.0108
ClI-1351	0.040±0.001	0.046±0.001	0.049	0.054
SiIV-1393	0.268±0.002	0.408±0.020	0.354	0.608
SiIV-1402	0.139±0.001	0.211±0.010	0.191	0.321
c1506	0.283±0.001	0.314±0.005	0.270	0.135
CIV-1548	0.604±0.005	0.772±0.024	0.706	1.223
CIV-1551	0.311±0.003	0.394±0.012	0.361	0.620
MgII-2796	59.7±0.3	79.3±3.5	62.7	111.9
c2796	23.4±0.1	25.1±0.2	19.5	8.19
MgII-2803	39.3±0.2	52.4±2.2	42.6	78.2
c2803	24.3±0.1	25.9±0.3	23.1	9.77
c2820	1514±1	1527±3	1340	382
X-rays	0.92±0.02	3.6±0.5	0.76±0.29	9.6±4.6

Note. — In Cols. 2 and 3, cited uncertainties are standard deviations of 7-day averages of $f/f_{\rm BOL}$ over the time span of the particular interval. In last row of Cols. 4 and 5, cited uncertainties are standard deviations of the X-ray $f/f_{\rm BOL}$ over

the 30 *Chandra* HRC epochs, 2005.8–2020.4 . Measurement errors for the average UV fluxes in the other rows of Cols. 4 and 5 typically are less than 4 units in the least significant digit.

3. ANALYSIS

This section describes the several approaches taken to characterize the cycle dependencies of the key FUV species, and NUV Mg II and the 2820 Å continuum band, considered in this study. The first part focuses on *SORCE* (SOLSTICE and XPS) 2003–2020, while the second part adds the STIS and *Chandra* campaigns on α Cen AB 2010–2020 to complete the "solar-stellar connection" for this fortuitous alliance of sunlike stars.

3.1. Flux-Flux Correlations over the Solar Cycle

3.1.1. Corrections to the SOLSTICE Time Series

Before presenting the solar cycle flux–flux correlations, there are a two subsidiary issues that must be addressed: (1) a series of epochs when a specific type of calibration observation was made (field-of-view [FOV] maps to investigate any influence of pointing on the instrumental sensitivity and to evaluate possible localized degradation of the optics), which apparently had a small photometric influence, uncovered specifically in the high-S/N 2820 Å continuum time series. There is an additional modest inconsistency, over time, in the c2820 fluxes themselves, which might be caused by an underestimate of the SOLSTICE-B NUV channel sensitivity decline. The c2820 inconsistency led to a further examination of possible small calibration offsets for the FUV species as well. Figure 12a illustrates these two effects.
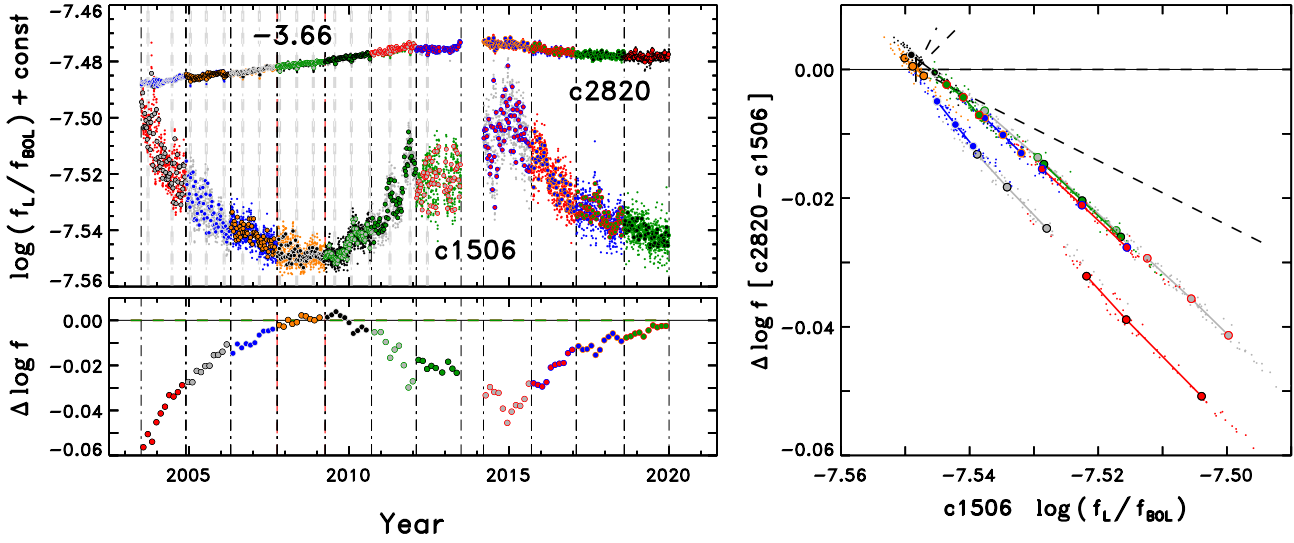
Fig. 12a.— Various comparisons between the FUV continuum band "c1506" and NUV counterpart "c2820."

Fig. 12a is a comparison between the FUV continuum flux "c1506" and NUV "c2820" over the SOLSTICE mission. The upper left panel shows the time history of the two fluxes, on a logarithmic $f/f_{\rm BOL}$ scale, where the c2820 fluxes were reduced by the indicated (logarithmic) factor to fit comfortably on the same diagram with the FUV time series. Small dots are daily irradiance values; larger dots are 1-week averages (about a quarter solar rotation). Note the six-month *SORCE* hiatus just prior to 2014.2 mentioned earlier. Thin vertical dot-dashed lines, and alternating symbol colors, mark 11 roughly equal time sectors in which flux–flux correlations were separately constructed (for reasons that will be clear shortly). Examination of the nearly flat c2820 time series (exaggerated by the expanded y-axis scale) reveals small dips occurring about every six months, coincident with the FOV-mapping calibrations mentioned earlier (marked by pairs of gray vertical dashed lines). The dips are very small, yet evident thanks the high precision of the SOLSTICE photometry and high S/N of the 8 Å c2820 continuum band. Intervals of a few days on either side of the calibration pointings were excluded from further consideration for the sake of uniformity, even though the impact on the other line diagnostics for the most part might be barely noticeable (if similar in amplitude to c2820). The excluded intervals represent a negligible fraction of the available time domain, in any event.

The lower left hand panel depicts the difference between the two flux curves, further up-binned to $\sim$2 rotations, normalized to a reference epoch 2007.75–2009.25 (vertical red dashed lines in both left panels), which corresponds to the low activity period between Cycles 23 and 24. The minimum of the difference near 2003.5 is noticeably lower than the subsequent minimum near 2015.0, even though the X-ray light curve indicates that these activity levels were similar, at least at high energies. This dichotomy suggested that there might be a further issue with the time dependence of either the FUV or NUV calibration, or both.

The right hand panel illustrates individual flux–difference relations for the 11 distinct epochs, separately color-coded, as a function of the c1506 flux. Small dots are 1-week averages; larger dots are up-binned along the x-axis by a factor of 20 (to achieve $\sim$3 points per 1.5-year time segment). The horizontal dark dashed line indicates a 1:1 correlation, the lower dashed line is for a power law slope $\alpha = +0.5$, and the upper two (short) dashed lines are for $\alpha = +2$ and $+3$. Now, the expected seamless, coherent flux–flux relation has devolved into parallel, displaced trajectories, with even some internal dispersion apparent within the upper branch. These separated tracks are unexpected given that the two continuum bands, which form by relatively simple atmospheric processes, should follow each other closely. Instead, the systematic displacements suggest small, time-dependent calibration errors, as might be deduced by simple examination of the upper left time series for NUV c2820, which shows a decline toward earlier times from the 2008 minimum, whereas the FUV c1506 band displays the anticipated rise back toward the previous cycle maximum.
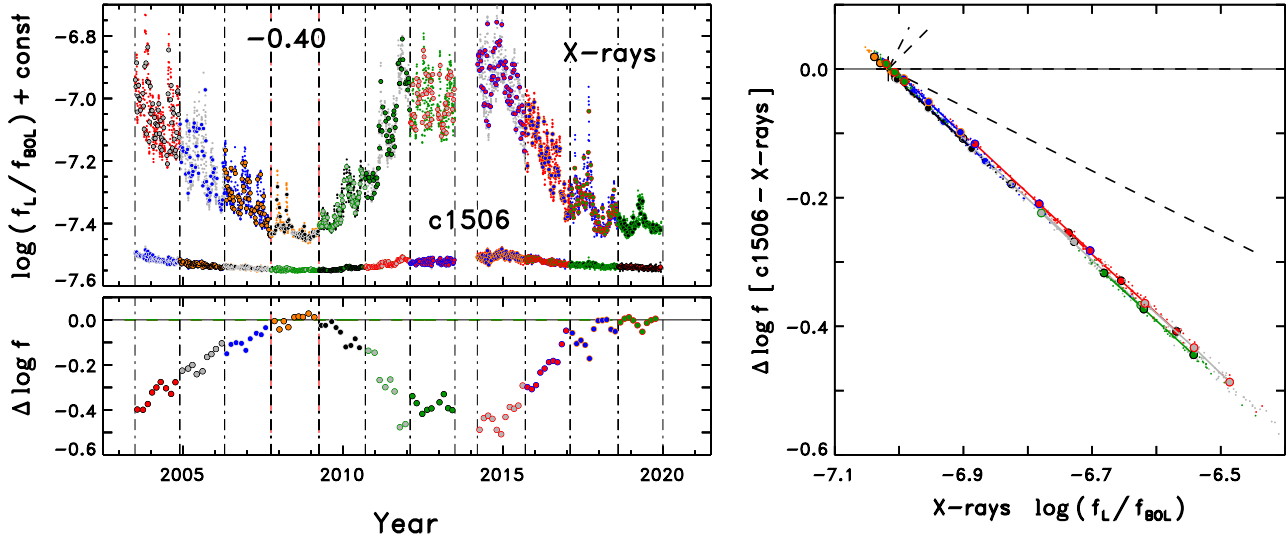
Fig. 12b.— Similar to Fig. 12b, for coronal X-rays versus FUV continuum band c1506.

Fig. 12b is a similar comparison between X-rays and the c1506 continuum flux. The coronal X-rays exhibit high contrast relative to the FUV chromospheric continuum band, and the difference time series at lower left is more symmetrical than the previous FUV–NUV continuum comparison. Nevertheless, close examination of the time-segmented flux-ordered differences in the right panel reveals similarly displaced tracks as in the previous figure, although less exaggerated (partly owing to the expanded y-axis scale). These small differences suggest possible slight inconsistencies, now between the relative calibration of SOLSTICE FUV and the FISM2 X-ray record.

If just the daily values had been plotted in the right panel of Fig. 12a, the downward sloping cloud of points would have roughly outlined a flux-flux correlation, with a boosted dispersion that might have appeared simply as statistical noise, but which the time-segmentation has revealed are systematic temporal shifts. For the subsequent analysis, it was assumed that the time-dependent offsets were, in fact, calibration-related, and were treated in a two-step process.

Firstly, the c1506 offsets relative to the X-rays were compensated by introducing small flux scale factors ($1\pm s$; $s\ll1$) at the centers of the time segments marked in Figs. 12b, and connecting these in a piece-wise linear fashion to create an overall calibration correction of FUV continuum relative to the X-ray cycle. The reasoning was that the X-ray time series shows the highest contrast of any of the FUV or NUV diagnostics, and is traceable to a different instrument (i.e., XPS), which is functionally very simple, lacking, for example, optical elements that can degrade over time with exposure to UV sunlight. The high contrast suggests that the shape of the time series is relatively immune to calibration errors (of the sort hopefully corrected in the advanced FISM2 compared with the earlier incarnation: see Fig. 8). The uncorrected X-ray – c1506 flux difference versus X-ray flux shows a strong correlation, albeit with the small deviations noted earlier. Thus it is reasonable to expect that the correlation is universal over cycle phase, and the time-dependent calibration corrections should be chosen to enforce that expectation.
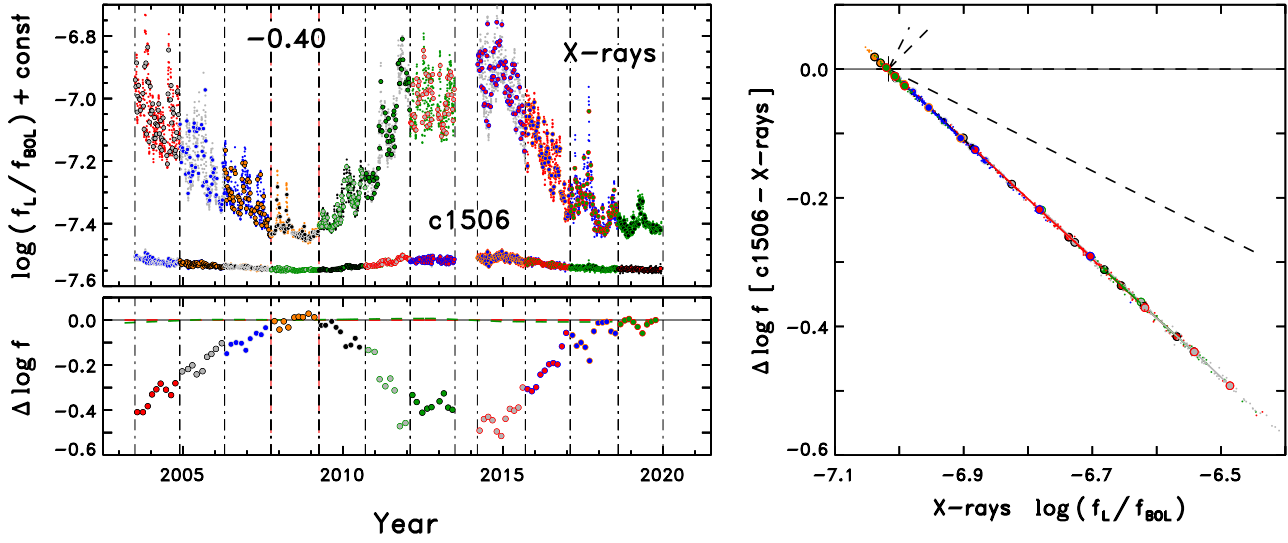
Fig. 13a.— Similar to Fig. 12b, but with small epoch-dependent flux corrections applied to the c1506 time series.

The procedure is illustrated in Fig. 13a, which depicts the corrected c1506 time series (changes barely noticeable), based on the calibration tweaks displayed in the lower left panel (green dashed: logarithmic values). The refined difference–flux correlation (right side), which now has tightened up. The time period 2007.75–2009.25, encompassing the minimum period between Cycles 23 and 24, was chosen to set the zero point of the correction scale. In other words, the average SOLSTICE FUV spectrum over that interval was assumed to have the correct absolute calibration at all wavelengths. The analysis then derives correction factors for the other time segments relative to the reference interval. This particular minimum period was reasonably close to the beginning of the *SORCE* mission, so any instrumental degradation in the FUV likely was modest, but far enough from the beginning that degradation trends could be measured. Choice of the high-S/N FUV continuum band was motivated by the stellar flux references for SOLSTICE, which are hot stars with maximum signal in the mid-FUV, so that degradation effects can be monitored best at those wavelengths.

The second part of the cross-calibration was to perform the same differential offset analysis for the other FUV and NUV diagnostic pairs, but now using the corrected c1506 time series as the reference template. The reasoning here is that the other FUV and NUV species were recorded by the same instrument, i.e., SOLSTICE, so that the differential offsets relative to the high-S/N FUV continuum band should be modest, aside from the already derived systematic shifts of c1506 relative to the X-ray record.
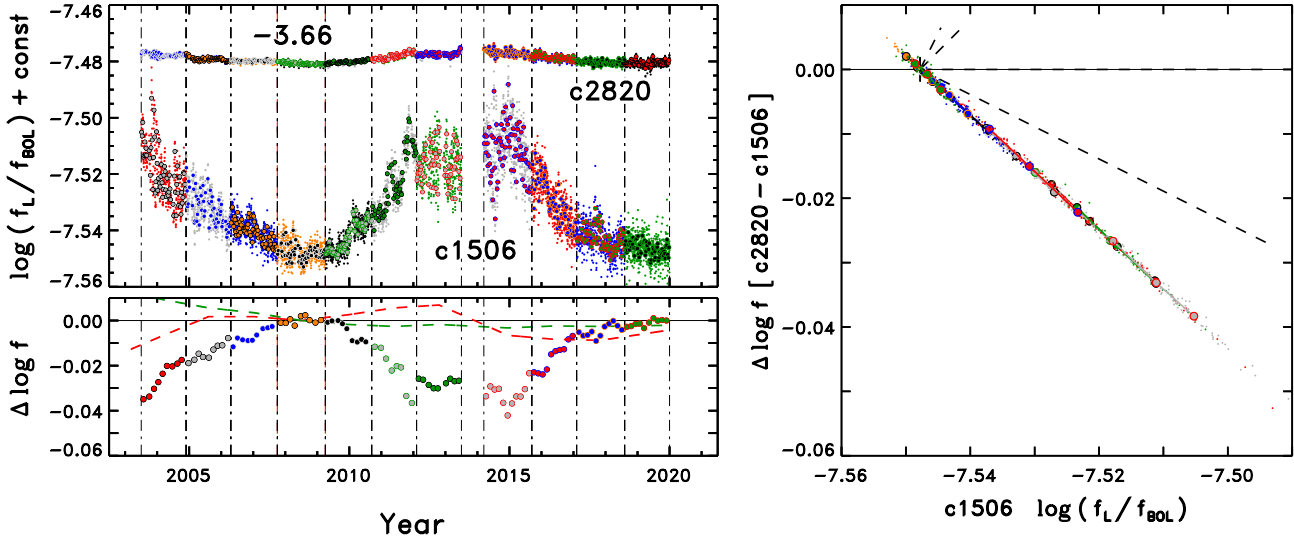
Fig. 13b.— Similar to Fig. 12a, but with small epoch-dependent flux corrections.

Fig. 13b shows the result of the cross-calibration applied to the c2820 NUV continuum band. The epoch-dependent flux scaling factors (logarithmic values) are the red- and green-dashed curves at lower left, for c1506 and c2820, respectively. Compared with Fig. 12a, the corrected c2820 time series is much flatter, the flux differences at lower left are more symmetrical with respect to cycle phase, and the previously disjoint difference–flux relation at right now is rectified. Notice that the c2820 corrections are relatively constant between 2010–2020, but display a mild up-tick at times before 2008, which compensates for the conspicuous down-turn of the c2820 fluxes noted in Fig. 12a during that period.

Similar differential calibration adjustments were derived, and applied, to all the measured FUV and NUV diagnostics in an effort to remove any extraneous systematic effects. Again, this was with the assumption that each flux–flux correlation should track a coherent path, regardless of epoch or cycle phase. (The correction approach will be described in more detail in Paper II of this series, involving solar EUV spectral measurements for which the calibration offset compensation proved to be even more important than the essentially trivial annoyance in this study.)

3.1.2. Examples of Flux–Flux Correlations for Pairs of Species

Having compensated for the possible calibration systematics, it is time to present the long-awaited flux–flux correlations. There are numerous possible combinations of species, so it is not practical to display them all, just a few examples. Four selected comparisons are provided in Figures 14a–14d. Additional examples, but not all the possibilities, will be given in subsequent figures. Nevertheless, all the important combinations are summarized in Appendix A, Table A1. Many of the correlations follow simple power laws, although some are better described by curved (or "bent") relations, as demonstrated in more detail below.
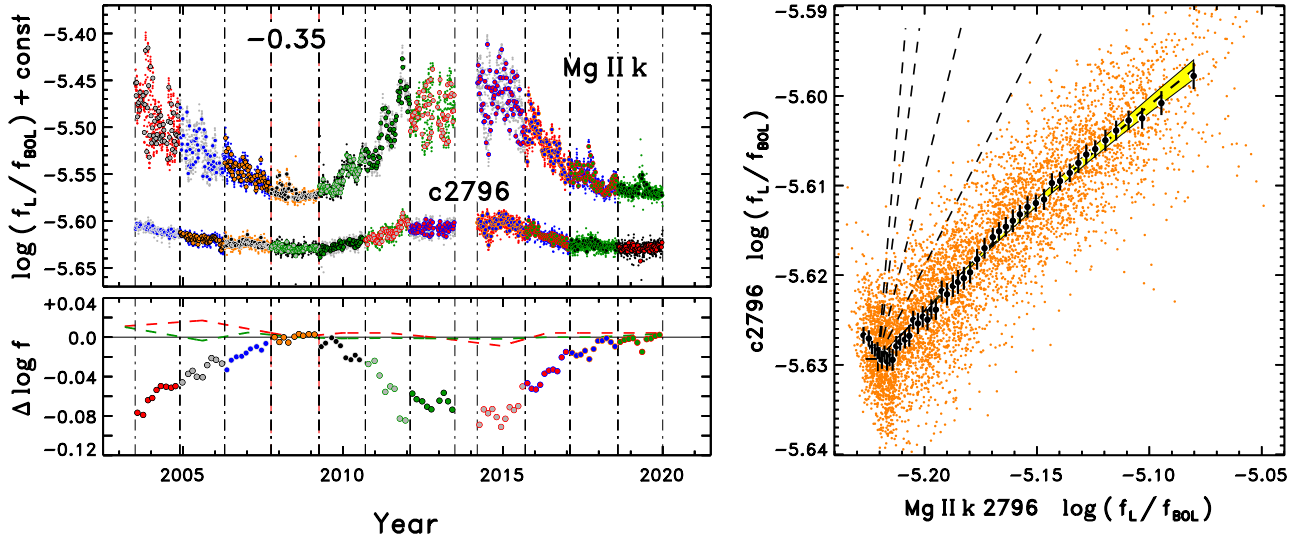
Fig. 14a.— Comparison of Mg II k-line core and c2796 block flux.

The first example, in Fig. 14a, is between the Mg II k line core flux and its block, c2796. This comparison bears on an issue raised earlier, namely the slight change in the SOLSTICE-B NUV resolution in 2006.07. In the upper left panel, there is no obvious change in the pre-2006 and post-2006 time series across the resolution boundary. Most of the correction was accomplished by tuning the parameters illustrated in Fig. 11 to match the measured pre- and post-2006.07 resolutions, but some is attributable to the calibration adjustments derived from the independent comparisons to the reference c1506 time series (logarithmic scale factors are the dashed curves at lower left: red for the core flux, green for the block). In the time series comparison itself, the core flux shows much larger cycle variability than the block flux, consistent with their separate origins: mid-to-high chromosphere for the core, upper photosphere/low chromosphere for the block.

In the right panel, orange points are daily flux pairs, while larger dark points and error bars represent values binned along the x-axis (k-line core flux). The up-binning was accomplished by taking groups of 110 y-axis values in ascending order of the x-axis values, eliminating the 5 highest and 5 lowest ("Olympic" filter), then averaging the remaining 100 y samples. A y error bar was assigned according to the standard error of the mean of the y fluxes in the super-bin. The x position is the average of the x values. In this case, the binned fluxes display a good correlation, although rather shallow. (The dashed lines represent power laws of slope 0.5, 1, 2, and 3: the point of origin is the average x and y values over the reference period 2007.75–2009.25.)

Closer examination of the correlation shows that it is curved slightly downward. The yellow-shaded relation under the up-binned points represents a "bent" power law, modeled as:

$$y = y_{\min} + c_1 \left(x - x_{\min} \right) + c_2 \left(x - x_{\min} \right)^2 , \qquad (2)$$

where $x \equiv \log \left(f_{\mathrm{X-Line}} / f_{\mathrm{BOL}} \right)$ represents the x-axis values for the X-line of the comparison pair (here, k-line core flux), and similarly for y for the Y-line (here, c2796). The parameter x_{min} is the average of the X-line flux distribution over the reference epoch 2007.75–2009.25; and similarly for y_{min}. The $c_{1,2}$ coefficients were obtained using the IDL routine "CURVE-FIT," which performs a non-linear least-squares fit, with the appropriate function specification, and utilizing the standard errors of the mean of the up-binned fluxes in the weighting factor, $1/\mathrm{error}^2$. The divergence of the shaded area represents $\pm 1\,\sigma$ extremes of the fitted parameters.

Aside from the well defined correlation at higher k-line core fluxes, there is a curious "hook" at the lower flux limit. The origin of the hook, and whether it has any physical significance, are unclear.
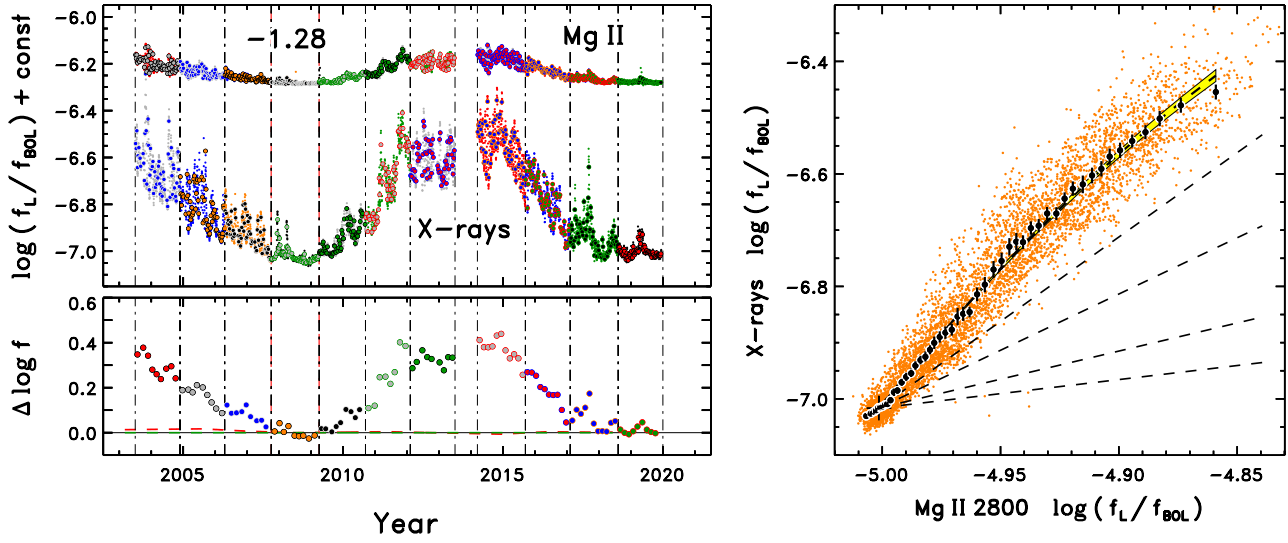
Fig. 14b.— Comparison of 0.2–2 keV coronal X-rays against mid-chromosphere Mg II h+k core flux ("Mg II 2800").

The second example, Figure 14b, in many respects is the most surprising. It depicts coronal X-rays versus the Mg II hk core flux (in this, and subsequent, comparisons the h and k core fluxes have been combined into a single "Mg II 2800" flux). In the upper left time-series panel, the Mg II fluxes are much higher than the 0.2–2 keV X-rays, reflecting the larger heating, and balancing radiative losses, of the moderate-temperature, dense chromosphere compared with the very hot, but nonetheless quite tenuous, low-emissivity corona. At the same time, the apparent coronal variability is much larger (a factor that makes solar "Space Weather" more impactful). In the lower left panel, the Mg II flux corrections are depicted in red dashed; the X-rays in green (identically unity [zero in the logarithmic presentation], given the fundamental reference status of the high-energy light curve). In the right flux–flux panel, the X-rays and Mg II display a close correlation, but the relationship again is noticeably bent: a steep initial power-law ($\alpha \sim 5$) followed by a return, at higher Mg II intensities, to the $\alpha \sim 3$ seen in the *ROSAT/IUE*-era stellar flux–flux relations. Apparently, as chromospheric activity falls during the declining phase of a magnetic cycle, the coronal X-rays initially drop rapidly with decreasing Mg II flux, roughly as the "stellar" $\alpha = 3$ power law; but at a certain activity juncture, the X-rays begin to plummet even more precipitously, a behavior not clearly evident in the earlier stellar samples.

The bent power law suggests a transition between different types of heating that govern conditions in the solar outer atmosphere at different phases of the cycle. Perhaps at the lower activity levels there is a shift away from the big internal Dynamo and its large-scale active regions toward the weaker, but more pervasive "surface dynamo" that generates small-scale flux ropes, a major source of the so-called "magnetic carpet" fields (Title & Schrijver 1998). Many of these small-scale flux concentrations are swept into the supergranulation subduction lanes where they interact with other magnetic elements, causing localized heating events. The surface ("little") dynamo should operate independently of the 11-year cycle, because it is controlled solely by local convective over-turning flows; whereas the big Dynamo is enabled by global rotation-dependent Coriolis effects and large-scale slow meridional transport. The magnetic carpet itself evolves over the cycle due to pollution by flux shredded from decaying active regions.
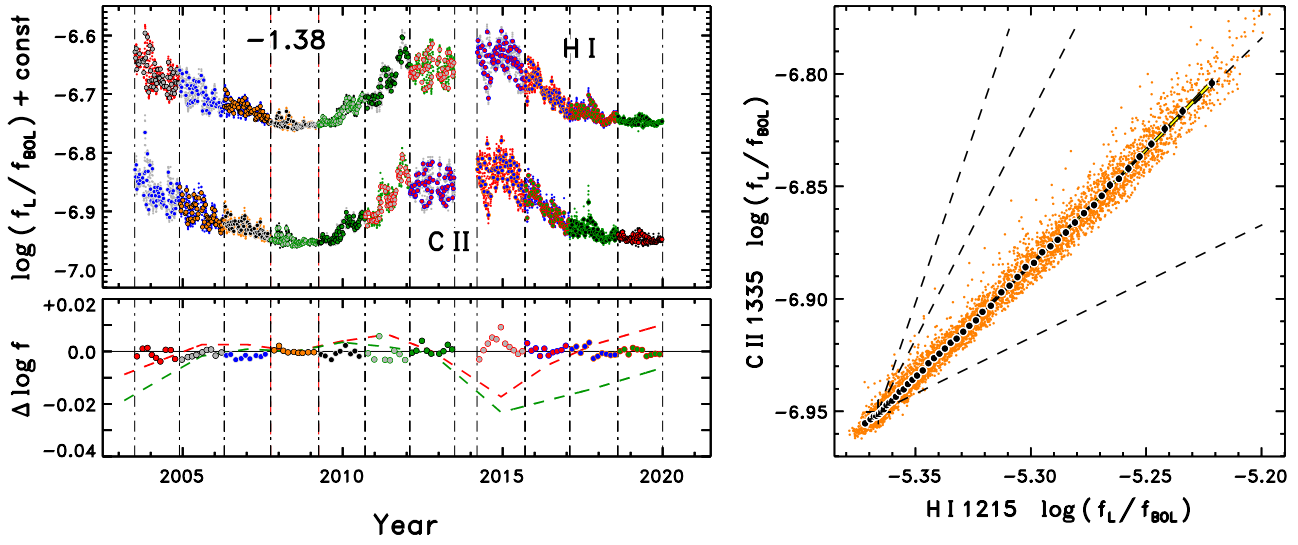
Fig. 14c.— Upper-chromosphere/low-transition-zone H I Lyα versus C II.

The third example, Figure 14c, is highly pertinent to the "stellar–solar connection:" solar experience that is relevant to the stars. The comparison is between two species that form between the upper chromosphere and low transition zone (low-TZ): H I Lyα 1215 Å and C II 1335 Å. In the left panel, the H I flux is considerably larger than the carbon emission, although the right panel shows that the Lyα flux is well correlated with the C II strength, with a power-law slope very close to unity, with no sign of "bending." This correlation is of interest not only for exploring the heating and cooling processes at different levels of the solar outer atmosphere, but also for quantifying the attenuation of the Lyα features of even nearby stars caused by interstellar atomic hydrogen absorption. Such degradation effects have been modeled in previous work (e.g., Linsky & Wood 1996; Wood et al. 2005), but the empirical behavior of Lyα versus other chromospheric diagnostics less affected by ISM absorption – like Mg II 2800 Å, C II 1335 Å, or Si III 1206 Å – offers an alternative, model-independent, way to estimate the unabsorbed stellar H I flux, at least for stars in the low-activity range spanned by the Sun's magnetic cycle. The hydrogen emission is particularly important for host-star impacts on their exoplanets, because Lyα is the dominant source of photoionization and photodissociation of cold, molecular atmospheres in most practical situations (e.g., France et al. 2018).
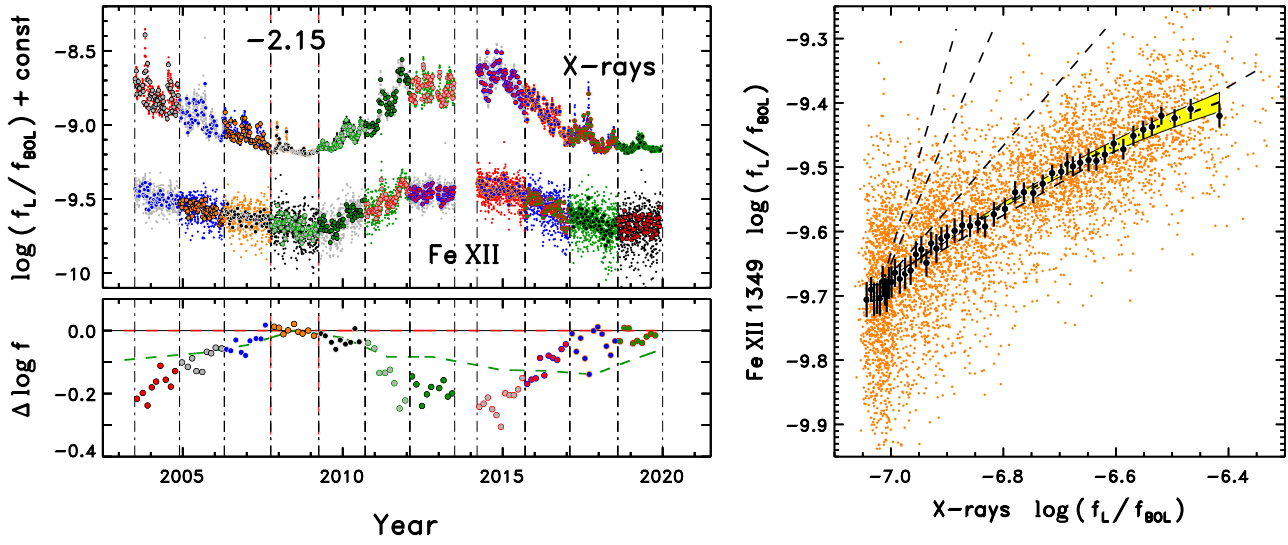
Fig. 14d.— Coronal forbidden line Fe XII versus coronal X-rays.

The final pair-wise example, Figure 14d, pits the Fe XII 1349 Å coronal forbidden line against 0.2–2 keV soft X-rays. In Fig. 9c, earlier, Fe XII appears as a very weak feature, under the best of circumstances. Given the low resolution of the SOLSTICE-A FUV channel, it is surprising that the integrated flux can be measured at all. Nevertheless, the remarkably high S/N and precision of the SOLSTICE daily scans allows even ultra-low-contrast features like Fe XII to be captured, as long as they are relatively isolated (the reason why the other, few times stronger, Fe XII component at 1241 Å could not be measured successfully). At the same time, the coronal forbidden line is weaker during the lower phases of the cycle, which introduces substantial noise into the joint correlation at low X-ray fluxes.

The left panel demonstrates that the FUV coronal line is very faint (more than 2 orders of magnitude lower in flux) compared to the soft X-rays, but also displays a large cycle contrast, like the X-rays. The right panel indicates that Fe XII initially rises more-or-less in step with the X-rays ($\alpha \sim 0.5 - 1$), but as the activity increases, Fe XII begins to bend over closer to an $\alpha \sim 0.5$ power law. The Fe XII emission forms in a relatively narrow temperature range peaking at around 1 MK, whereas the broad-band soft X-rays can arise over a much wider span (e.g., 1–10 MK, or even hotter in flares). Thus, the bent power law between Fe XII and X-rays likely is a coronal temperature effect, as the global high-energy emission evolves from dominance by the "cooler" ($\lesssim 1$ MK) supergranulation magnetic elements at low activity, to a mixture of the supergranulation bright points and warmer active regions (2–3 MK) as the cycle progresses.

3.1.3.   Examples of Flux–Flux Correlations for Multiple Species against a Single Reference

The final set of solar comparisons involves groups of species contrasted against a single reference. The four references are: Mg II 2800 Å ($T \sim 8{\times}10^3$ K; Fig. 14a), H I 1215 Å ($T \sim 2{\times}10^4$ K; Fig. 14b), C II 1335 Å ($T \sim 3 \times 10^4$ K; Fig. 14c), and Si III 1206 Å ($T \sim 5 \times 10^4$ K; Fig. 14d). Here, for clarity, only the up-binned fluxes are illustrated. In these presentations, the individual flux–flux relations were shifted along the vertical f/f_{BOL} axis to coincide at the origin, while the reference species was expressed in relative fluxes, between cycle MIN to cycle MAX along the horizontal axis. Both scalings were so that the apparent relations could be compared against one another as fairly as possible. In these examples, there are several instances where the two isolated components of a doublet, for example Si IV 1393 Å and 1402 Å, were combined into a single total flux, in that case "Si IV 1400 Å." In other cases, such as O I 1305 Å (1304 Å +1306 Å) and C II 1335 Å (1334 Å +1335 Å), the components were partially blended at SOLSTICE resolution, and thus already integrated together in the same bandpass.
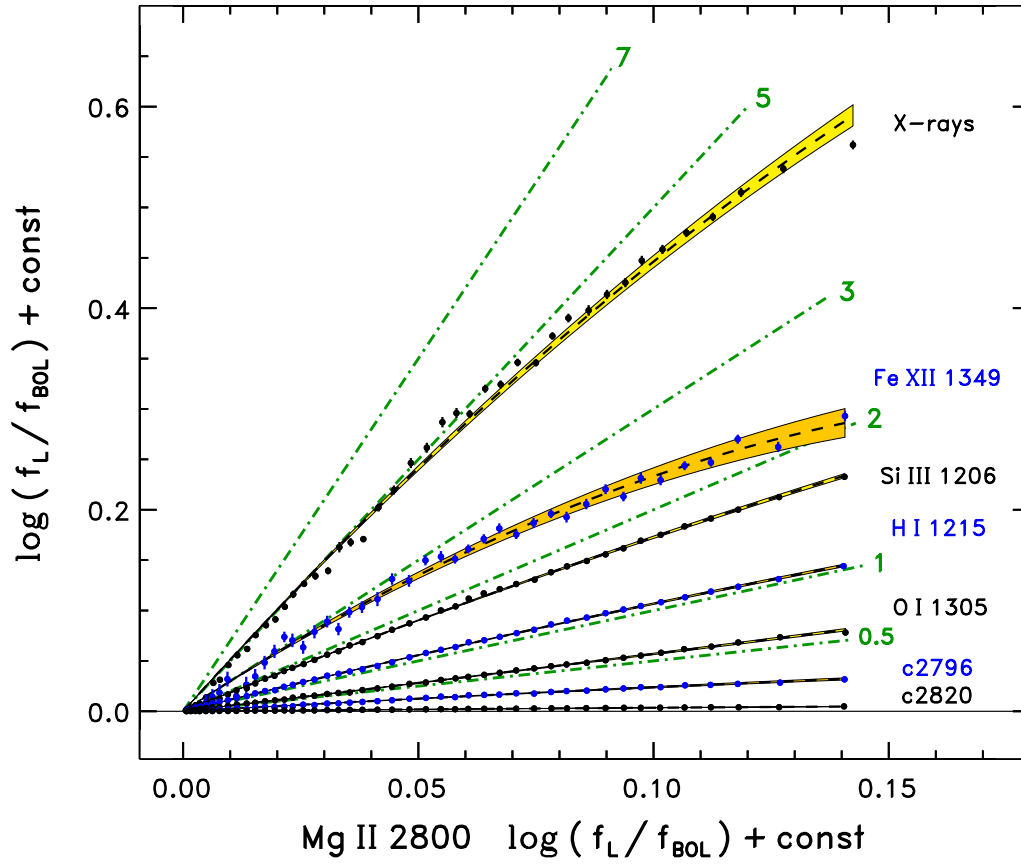
Fig. 15a.— Combination solar flux–flux diagram pitting various species against a reference, in this case mid-chromosphere Mg II 2800 Å.

Fig. 15a is for Mg II 2800 Å as the reference. Green dot-dashed lines represent power laws of the indicated slopes. There are systematic trends of the other species relative to Mg II across the cycle range spanned by the premier chromospheric diagnostic. The general behavior parallels that seen in the earlier stellar surveys (e.g., Ayres et al. 1995), namely the power-law slopes tend to increase with increasing formation temperature; lowest for the c2820 photospheric continuum flux; higher for the c2796 block flux, which has mixed photosphere/chromosphere origin; higher still for the two O I triplet lines 1304 Å + 1306 Å combined, which, like Mg II hk, form in the middle chromosphere; even higher for H I 1215 Å and Si III 1206 Å, which arise in the upper chromosphere and low-TZ (2–5×10^4 K), respectively; and finally much steeper, bent power laws for Fe XII and coronal soft X-rays. Note that the O I correlation is shallow, $\alpha \sim 0.5$, whereas the one other FUV resonance line with similarly elevated excitation energy, H I Lyα, has $\alpha \gtrsim 1$. This probably is because the extremely high opacity in the hydrogen resonance line forces its contribution function to higher altitudes and higher temperatures, whereas the much less opaque O I lines would form in the middle chromosphere where temperatures are lower and high-excitation transitions are less favored energetically. (This dichotomy is reflected in the formation temperatures cited in Table 5.)
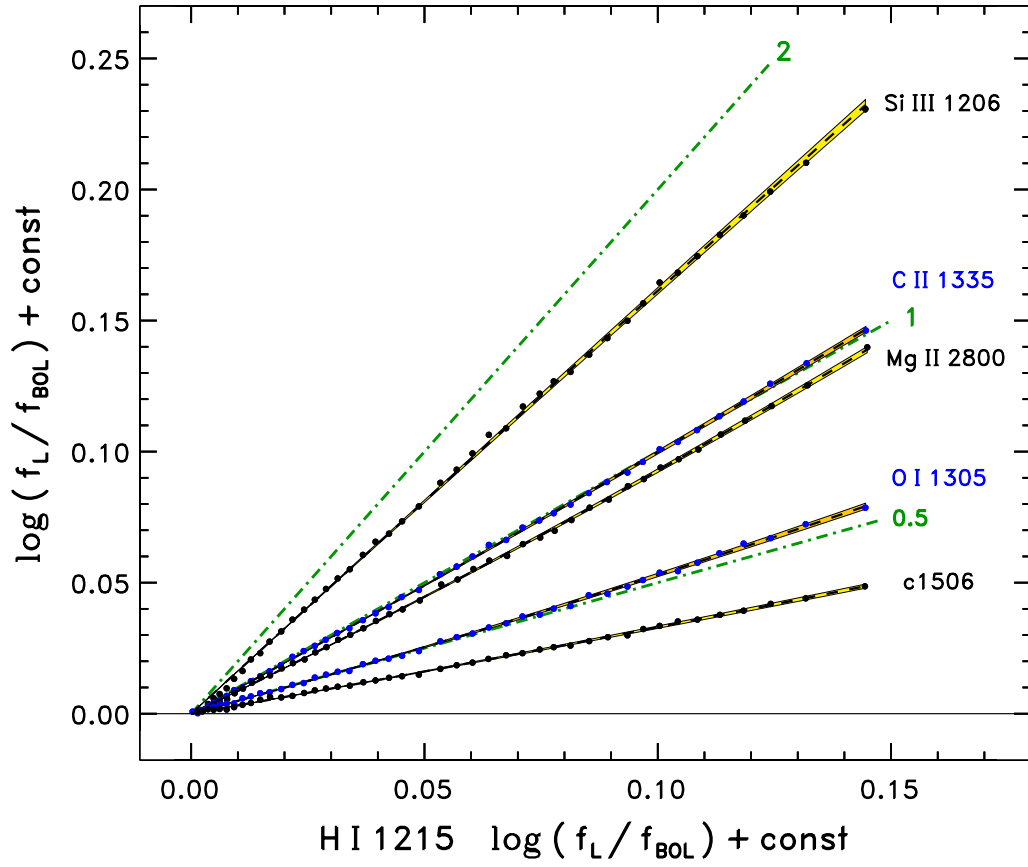
Fig. 15b.— Combination solar flux–flux diagram, for reference upper chromosphere H I 1215 Å Lyα.

Fig. 15b is for H I 1215 Å Lyα as the reference. Two new species are shown: the FUV continuum c1506 and the C II 1335 Å resonance multiplet. The c1506 band shows a shallow power law slope relative to high-chromosphere H I, which is not surprising, but a steeper trend than seen in the genuinely photospheric NUV continuum band at 2820 Å (Fig. 15a). As anticipated from the previous figure, both O I and Mg II display shallow slopes (< 1) relative to Lyα, the former much more so than the latter; and both relations curve slightly upward. Moving higher in excitation, the C II 1335 Å multiplet and H I are remarkably well correlated, with a power-law slope very close to unity (as seen already in Fig. 14c). C II technically has a higher collisional ionization equilibrium (CIE) peak temperature than Lyα, but both are optically thick resonance lines that arise from species (C^{+1} and H^0) that likely are out of CIE at the relevant temperatures. In fact, the strong Lyα emission falls just inside of one of the $C^0 \rightarrow C^{+1}$ photoionization continua (near 1240 Å; see Fig. 2), so the carbon ionization balance is coupled to the non-LTE H I resonance line formation. Regardless of the theoretical nuances, the empirical 1:1 result has practical value, as alluded earlier, in that C II 1335 Å, which is less affected by ISM absorption, could serve as a proxy to estimate the true Lyα flux from a star whose 1215 Å feature was strongly absorbed by interstellar hydrogen. The final comparison is against Si III 1206 Å, which shows a steeper power law ($\alpha \sim 1.6$), as expected within the traditional stellar paradigm given the higher formation temperature of doubly ionized silicon.
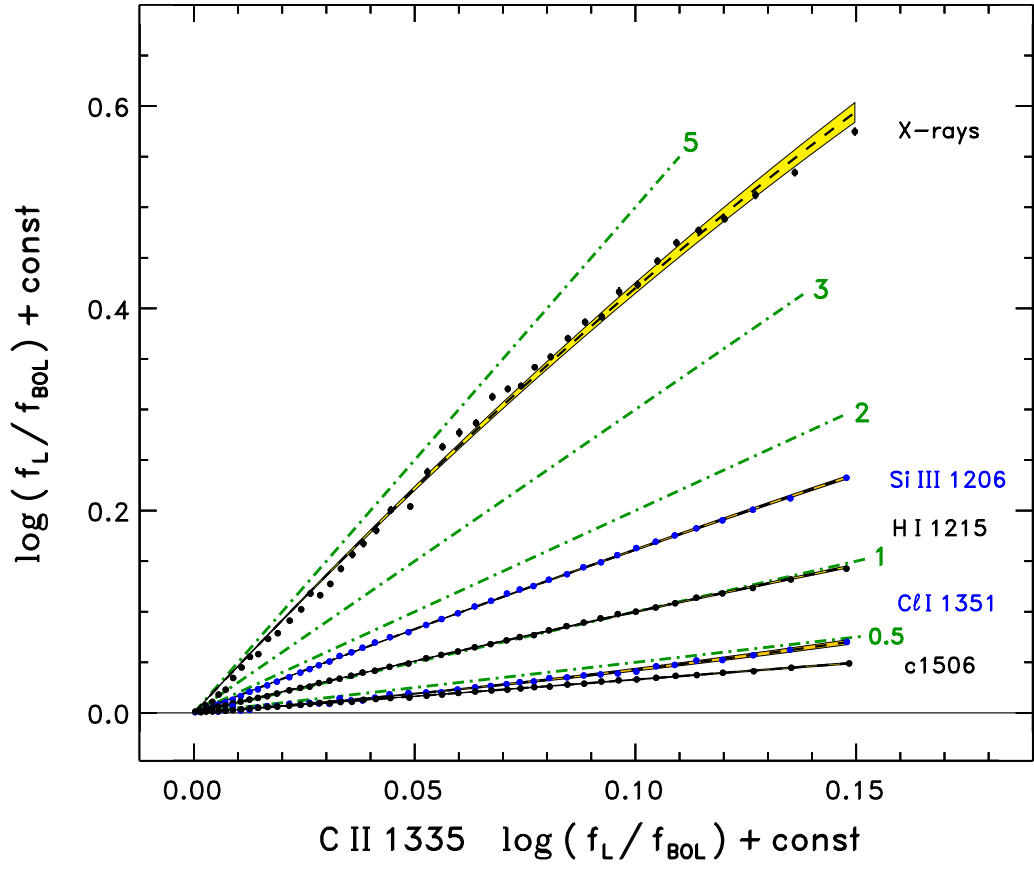
Fig. 15c.— Combination solar flux–flux diagram, for reference low-TZ C II 1335 Å.

Fig. 15c is for C II 1335 Å as the reference. This comparison includes some of the species from the previous Lyα diagram, but now also coronal X-rays shown earlier in Fig. 15a, as well as chromospheric Cl I 1351 Å. The close correspondence between Lyα and C II is repeated here, but also note the bent power law for the soft X-rays, and less strongly curved relation for Si III. Apparently, the bent nature of the coronal diagnostic persists beyond Mg II up to at least the higher formation temperature of C II. This indicates that the bent power laws are not an accident of the way in which the NUV Mg II lines were processed, but rather a general behavior of the coronal species when compared to lower excitation FUV emissions.

Another curiosity is Cl I 1351 Å. Chlorine lines are not prominent in the solar spectrum owing to the low abundance of the element, so the relatively strong 1351 Å emission seen in early FUV spectra from *Skylab* (e.g., Cohen et al. 1978) and the *Solar Maximum Mission* (*SMM*: Woodgate et al. 1980) was a puzzle (Shine 1983). That author pointed out that another member of the Cl I multiplet, 1335 Å, is coincident with the red component of C II, consequently 1351 Å could be radiatively pumped via the strong low-TZ emission. In that scenario, the Cl I fluorescence might be expected to follow the C II flux hand-in-hand, yet the apparent correlation is flatter, $\alpha \sim 0.5$, much as seen for the atomic oxygen 1305 Å lines in the previous figure (noting that H I 1215 Å and C II 1335 Å essentially are interchangeable as reference [x-axis] species). Nevertheless, C II 1335 Å would have high opacity in the middle chromosphere where Cl I 1351 Å likely is pumped, so the scattered radiation field viewed by the chlorine atoms probably is rather flat and diffuse (Shine 1983), and the fluorescence might respond less than linearly to the increasing C II intensity viewed by an external observer.
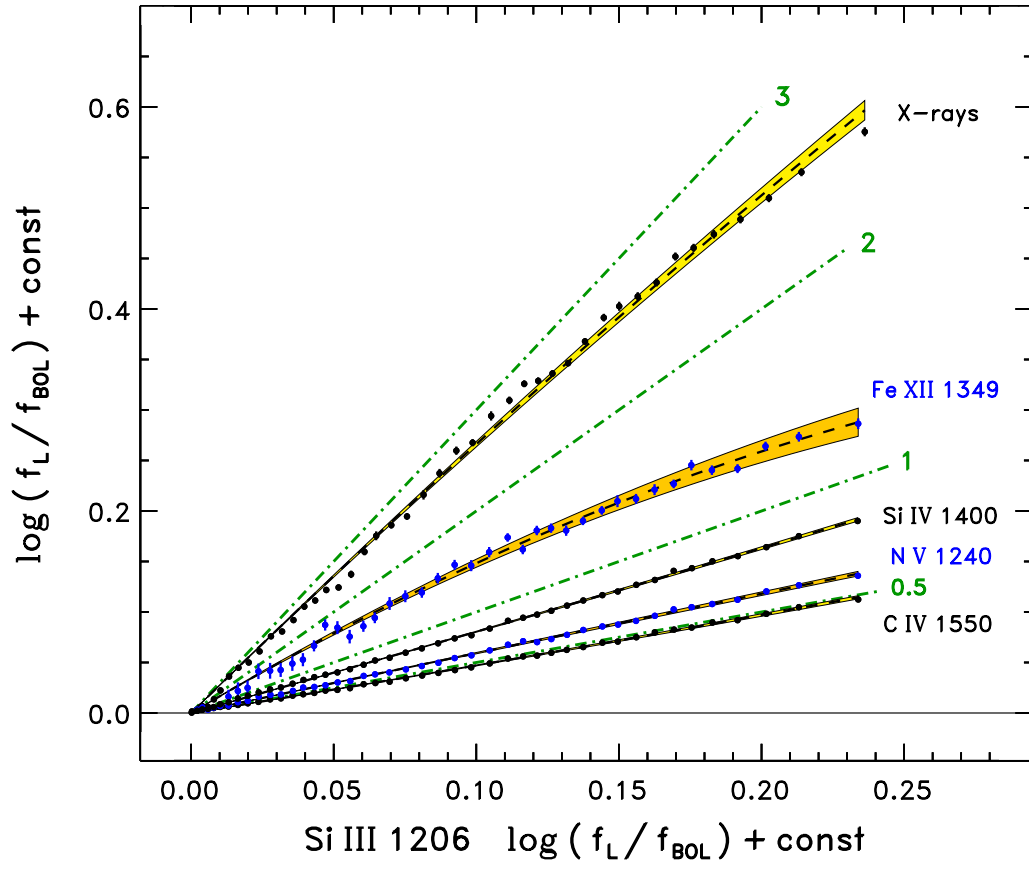
Fig. 15d.— Combination solar flux–flux diagram, for reference low-TZ Si III 1206 Å.

The final solar figure, 15d, is for Si III 1206 Å as the reference. This comparison contains all the important species with nominal CIE temperatures higher than Si^{+2}, including the two coronal tracers. The comparisons are both unexpected and remarkable. The unexpected aspect is that the Li-like high-ionization species C IV 1550 Å and N V 1240 Å both show relatively feeble power-law slopes compared with lower temperature Si III, not much better than $\alpha \sim 0.5$. This is contrary to the previous stellar lore, which found increasing power-law slopes with increasing excitation energy when compared with a lesser excitation species. Even Si IV 1400 Å shows $\alpha < 1$ with respect to Si III, whereas certainly $\alpha > 1$ would be anticipated. This is a genuine puzzle. The remarkable part is that Fe XII and X-rays both display at least partially bent power laws, so the odd behavior continues up to Si III temperatures. In fact, this trend continues through Si IV 1400 Å, C IV 1550 Å, and N V 1240 Å (not shown explicitly here, but see tabulated indices in Table A1).

3.2. Flux-Flux Correlations over the Cycles of Alpha Cen AB

The solar correlations based on $SORCE$-SOLSTICE (and XPS/FISM2) are of superior quality owing to the high-S/N of the daily scans, bolstered further by 110-sample up-binning, with Olympic filtering to remove outliers. Also contributing are the high-precision of the calibrations, both internally within the SOLSTICE instrument itself, as well as the frequent measurements of a suite of carefully vetted external UV-constant hot stars; and including the various cross-calibration corrections described earlier. These exquisite records have revealed puzzling bent power laws and curious inversions in the power-law hierarchy, whereby Si III 1206 Å holds the title "most active" of the $T \lesssim 2 \times 10^5$ K FUV species, whereas normally N V 1240 Å would have that honor. Are these behaviors unique to the Sun, or do they hold more generally for other stars of sunlike low activity? This is where the, albeit shorter and less precise, STIS UV time series of α Cen AB come into play.
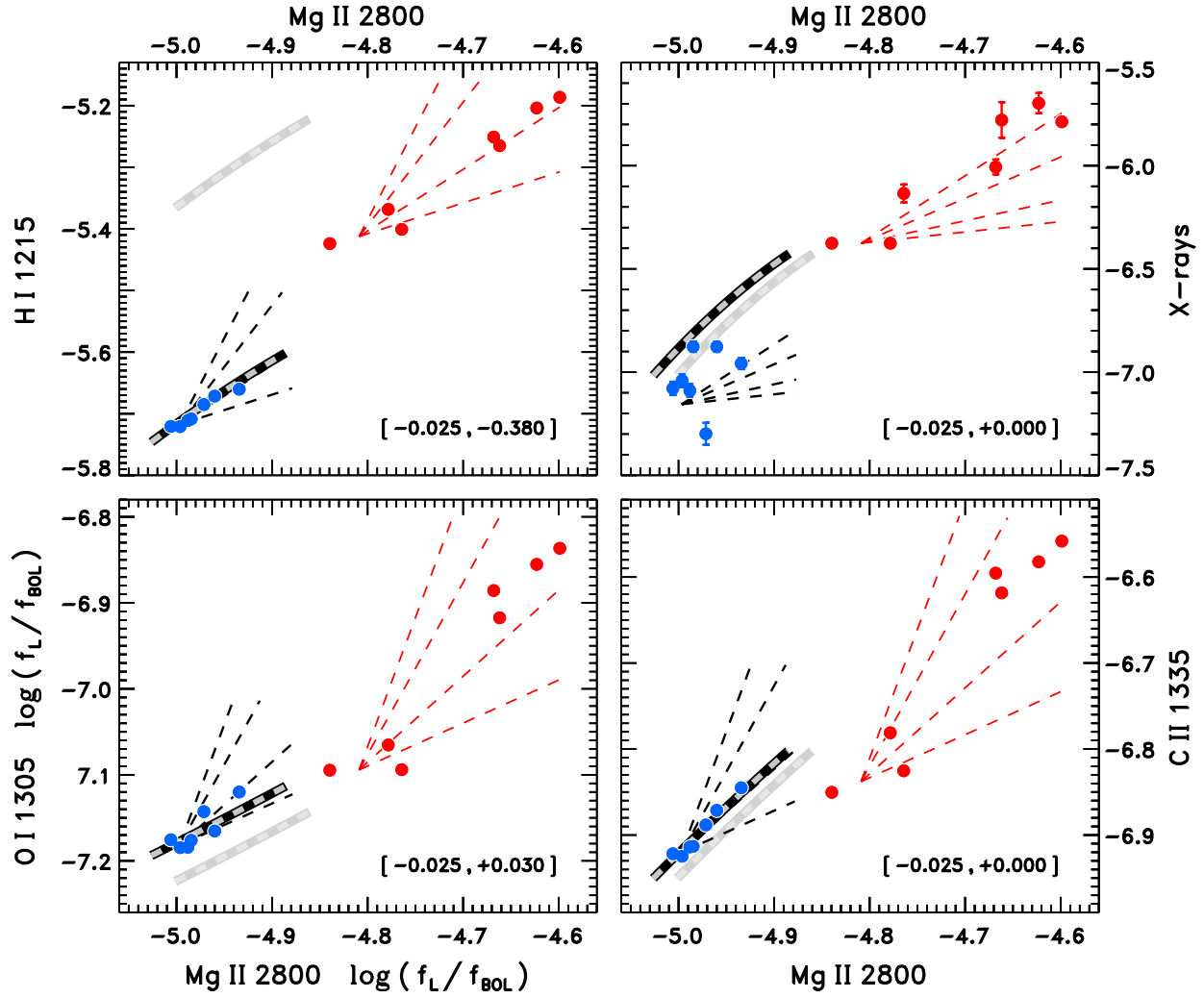
Fig. 16a.— Solar-stellar flux–flux correlations against reference Mg II.

Figure 16a displays correlations between mid-chromosphere Mg II 2800 Å and four other species: mid-chromosphere O I 1305 Å (lower left panel); high-chromosphere H I 1215 Å Lyα (upper left); low-TZ C II 1335 Å (lower right); and coronal soft X-rays (upper right). In each panel, the x-axis and y-axis both are $\log(f_{\rm L}/f_{\rm BOL})$. Blue dots are the scatter points for α Cen A; red dots for B. (Note: the *HST* UV and *Chandra* X-ray pointings were contemporaneous [typically within 2 months, often within 1] but not simultaneous, so the X-ray value closest in time to each UV point was adopted.) As in the previous flux–flux diagrams, dashed lines fanning out from the approximate origins of the A and B relations, separately, depict simple power laws: from bottom to top, $\alpha = 0.5$, 1, 2, 3. The equivalent solar flux–flux relation is depicted by a broad gray line. The darker broad dashed line is the result of translating the nominal solar relation by the bracketed values of Δx and Δy listed in the lower right corner of each panel, in order to obtain a better empirical match to the α Cen A correlation. In most cases, the shifts are relatively minor, and are in the direction expected for the small differences in abundances between the Sun and (slightly metal-rich) α Cen A. In other cases, such as Lyα, and to a lesser extent Mg II, the shifts are more significant, and compensate mainly for ISM absorption effects (which, in the case of Mg II would subtract from an otherwise small positive shift due to metallicity). There are other cases, such as the coronal X-rays, where the empirical shifts between the Sun and solar-twin α Cen A cannot easily be attributed to metallicity differences

Consider the large Lyα shift. It corresponds to a dip in the observed H I flux down to about 42 % of the "expected" value (i.e., from the ISM-free solar relation). Qualitatively similar drops are seen in the ISM modeling of α Cen AB by Linsky & Wood (1996), although the authors did not provide quantitative estimates for the specific flux deficits (their objective was to derive hydrogen column densities rather than flux correction factors per se). However, subsequently Wood et al. (2005) did present estimates of the unabsorbed Lyα fluxes for α Cen AB (their Table 3). Taking epoch-average values for the observed ("absorbed") STIS Lyα fluxes of AB (Table 6, here), the deficits relative to the reported unabsorbed fluxes are -0.28 dex for A (vs. -0.38 dex here) and -0.50 dex for B. This should be considered good agreement for α Cen A given the uncertainties (mainly that it would follow the solar Lyα relation exactly).

Back to the flux shifts in general: for a given species, the same shift was applied in all its displayed correlations. The Mg II flux–flux relations are not as impressive as those that will be shown later, because there are far fewer of the NUV observations of the α Cen stars. Nevertheless, the A relations seem to agree well with the scaled solar equivalents, while B appears to show somewhat steeper slopes, at least for O I and C II. In the cases of O I and X-rays, the solar relation appears to segue seamlessly into the lower points of the B correlation; whereas for H I and C II, the solar and B power laws are noticeably disjoint.
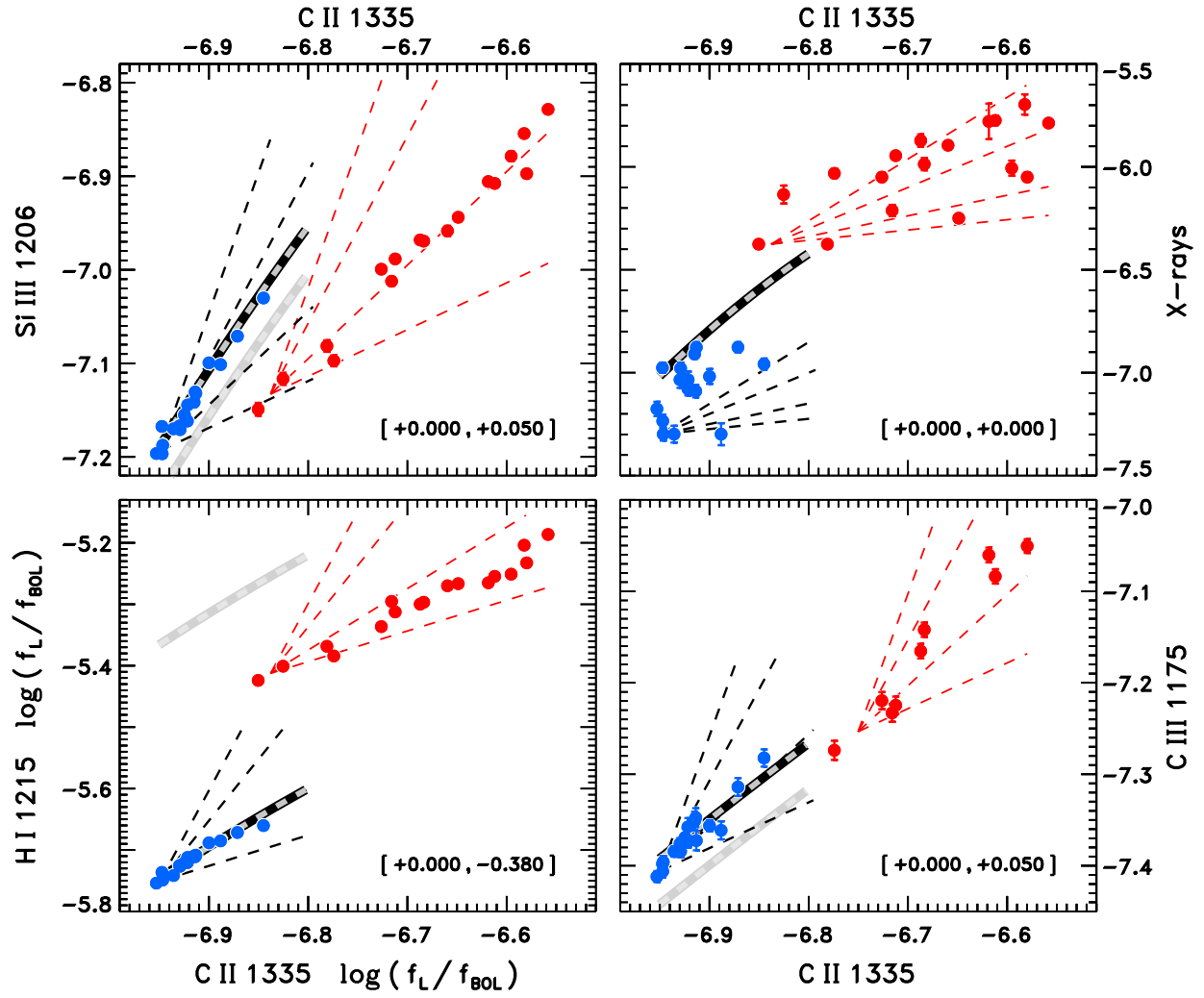
Fig. 16b.— Solar-stellar flux–flux correlations, for reference C II.

Figure 16b displays correlations between low-TZ C II 1335 Å and high-chromosphere H I Lyα (lower left); low-TZ Si III 1206 Å (upper left); low-TZ C III 1175 Å (lower right); and coronal soft X-rays (upper right). These flux–flux diagrams are more populated given the better FUV coverage of the two stars, although the C III comparison for B still is missing points for epochs when E140H exposures were taken: these cut off just below Si III 1206 Å, so C III 1175 Å was excluded. As tentatively seen in the Mg II panels previously, the A correlations line up nicely with the solar equivalents, although A's X-rays still are shifted downward, and noisier than the others perhaps partly because of non-simultaneous coverage. Again, there is somewhat disjoint behavior in several of the panels between the A and B relations. Notice also that A's Lyα slope closely matches that of the solar correlation, but B's trend is somewhat shallower. Similarly, the Si III correlation against C II is noticeably shallower for B, and curiously shifted downward, compared to A or the Sun. At the same time, the C III behavior of B appears to be steeper. Finally, A's X-rays (though scattered) seem to show a steeper rise with increasing C II, as in the lower branch of the Sun's bent power law, whereas B displays a flatter relation (although still with $\alpha \sim 2$).
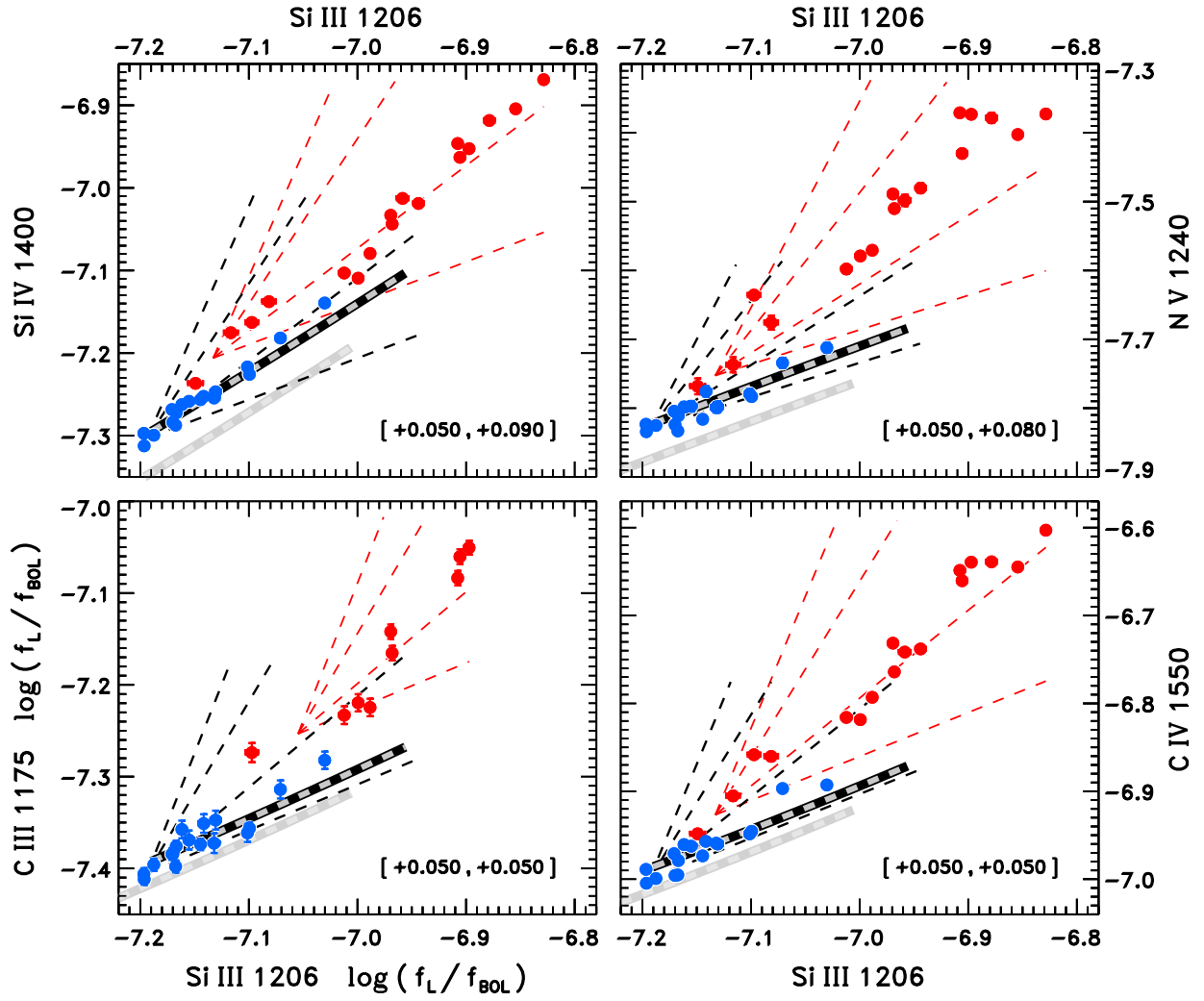
Fig. 16c.— Solar-stellar flux–flux correlations, for reference Si III.

Figure 16c displays correlations between low-TZ Si III 1206 Å and low-TZ C III 1175 Å (lower left), mid-TZ Si IV 1400 Å (upper left), mid-TZ C IV 1550 Å (lower right), and mid-TZ N V 1240 Å (upper right). Again, the C III comparison is lacking a few points for α Cen B, most conspicuously on the low flux side. Despite that, all four panels have the same general appearance: the A points closely track the translated solar power laws, while B shows universally steeper slopes. Curiously, the B trends have "retreated" backward to the extent that the A and B origins of the four correlations are similar (again taking into account the abbreviated C III series for B). This is a consequence of the behavior seen in the upper left panel of previous Fig. 16b, wherein B's Si III points were seen to parallel those of A, but also approach a similar minimum. This behavior is unlike the other diagnostics shown earlier, for which the *minimum* B value generally was comparable to, or exceeded, that of A's *maximum*. The contrary behavior emphasizes the unique position of Si III 1206 Å in both the Sun and α Cen A, as a "super-active" species, showing the steepest power laws relative to the other FUV features, even including hot N V. In α Cen B, in contrast, the Si III feature has declined in strength, and shows the expected "stellar" behavior, namely Si IV, C IV, and especially N V all exhibit power laws comparable or steeper than unity against Si III.
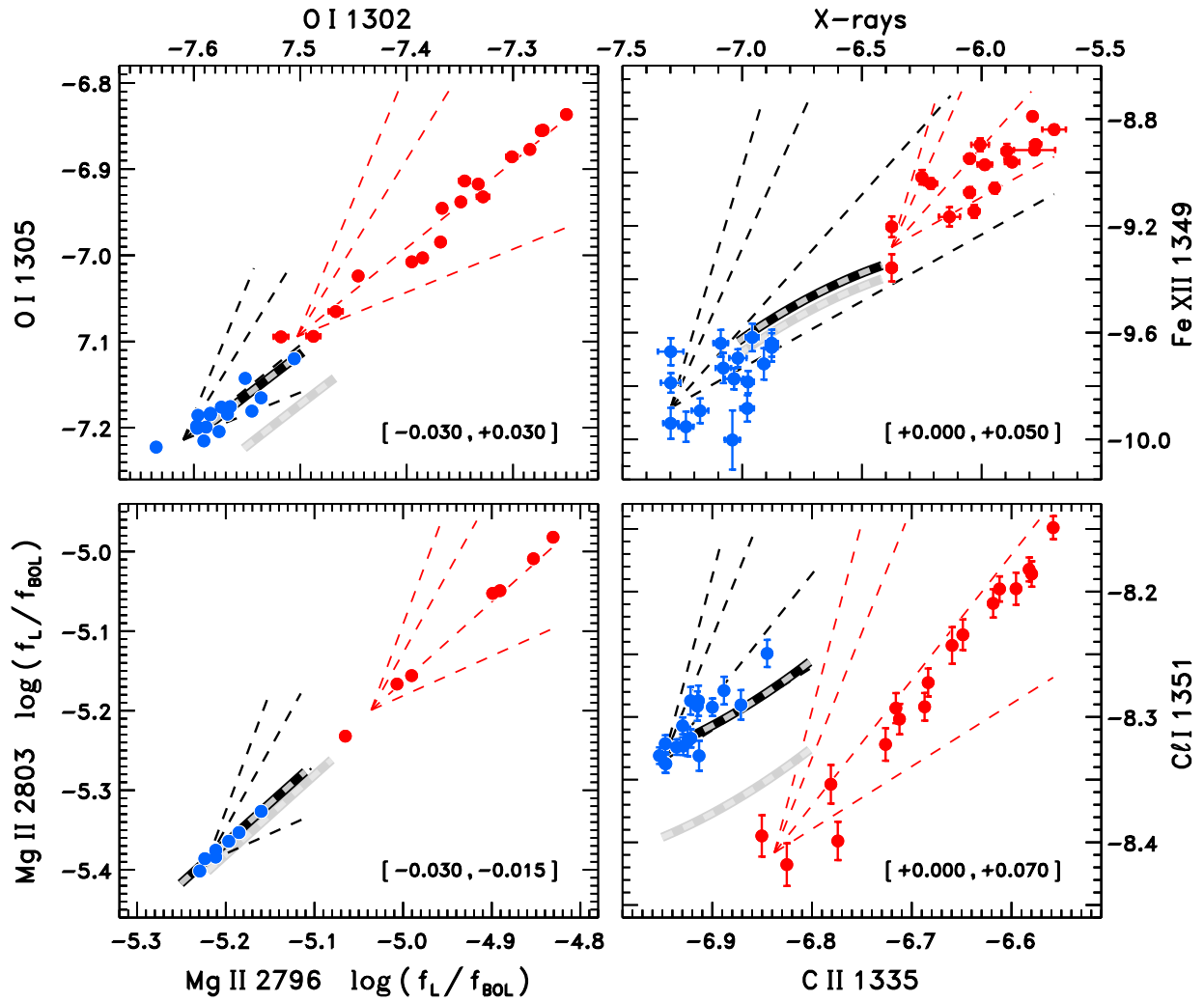
Fig. 16d.— Solar-stellar flux–flux correlations, for miscellaneous reference species.

The final figure, Figure 16d, illustrates a number of miscellaneous, but nonetheless illuminating, comparisons. The lower left panel compares the two Mg II resonance lines, which both are affected by ISM absorptions, but the k-line more so than the weaker h-line. The α Cen A 1:1 correlation extends seamlessly into the higher intensity B series, also 1:1, with negative x and y shifts compatible with the overall Mg II 2800 Å combined doublet (interstellar absorption) shift for A seen earlier (e.g., Fig. 16a).

The upper left panel compares O I 1302 Å against the other members of the triplet, O I 1305 Å (composed of 1304 Å + 1306 Å). The 1302 Å resonance line, arising from the 0 eV level of the ground term, is more affected by ISM absorption than the other two components, from excited levels 0.020 eV and 0.028 eV above ground. Thus 1302 Å has a slightly negative x-axis scale factor, to compensate for the increased interstellar absorption, which, in concert with the slightly positive y-axis factor for 1305 Å, achieves an excellent match to the solar 1:1 relation. Similarly, B shows an essentially 1:1 correlation between the two atomic oxygen features, closely following the extrapolation of A's (and the solar) trend.

The lower right panel compares the Cl I fluorescent emission mentioned earlier, with the presumed C II 1335 Å pumping transition. A chlorine shift was specified to align the bases of the solar and α Cen A trends, given the (negligible) carbon shift inferred in earlier comparisons (balancing between a positive metallicity boost and the negative drag of ISM absorption). If the chlorine adjustment represents an abundance enhancement, it is a small increase over that deduced for silicon. The lower part of A's Cl I trend now sits comfortably on top of the scaled solar relation, although A's slope appears to be steeper than the solar counterpart. Meanwhile, B's correlation unaccountably is displaced *downward* from that of A, and the slope clearly is closer to the 1:1 naively expected from the radiative pumping process described earlier. B's downward shift is puzzling, because its C II fluxes are larger than those of A, so the pumping of the Cl I line should follow suit. The suppressed Cl I fluorescence possibly is due to a thicker chromosphere on the somewhat more active early-K dwarf, which would inhibit the diffusive scattering of the C II photons – created in higher, hotter layers – down into the middle chromosphere where the atomic chlorine density likely peaks. However, an essentially similar argument was offered to explain the shallower Cl I versus C II power law seen in the Sun, which then would be challenged by the apparent 1:1 correlation in B. This conundrum among the three sunlike stars could be tested by the type of NLTE fluorescence simulations described by Shine (1983), although using more sophisticated chromospheric models and the better understanding of the various key atomic physics parameters achieved over the decades since the pioneering *SMM* investigation. Thankfully, that modeling is beyond the scope of the present work.

The final panel, in the upper right, compares the Fe XII 1349 Å coronal forbidden line

to soft X-rays. Recall that in the STIS observations of the α Cen stars, both members of the Fe XII multiplet could be measured, not just weaker 1349 Å as in the lower resolution SOLSTICE scans. The empirical ratio of 1241 Å/1349 Å was about 2.5, averaging over the epoch-combined E140M spectra of AB, so the total 1241 Å + 1349 Å flux was divided by 3.5 to obtain a higher S/N estimate of the 1349 Å contribution, alone, for each star. For scaling the solar trend, the y-axis shift was taken equal to that of Si III (as a representative metal line). The empirical behavior of A's Fe XII seems to roughly follow a $\alpha = 0.5 - 1$ power law, like that of the lower end of the bent solar power law, but falls systematically below the scaled solar power law. The solar relation then seems to connect to the bottom end of the B cloud, although the B correlation beyond that point appears to be steeper.

4. DISCUSSION and CONCLUSIONS

As mentioned at the outset, this study was intended to be primarily observational, with minimal discussion. Nevertheless, a few points can be made.

First, and foremost, there is a clear distinction between the various X-ray, FUV, and NUV flux–flux correlations of the Sun and solar-twin α Cen A, on the one hand, and cooler more active α Cen B on the other. The high-quality relations for the Sun, over 1.5 cycles, albeit weak ones, show bent power laws between coronal X-rays (and Fe XII) and virtually all the other lower temperature species. These bends suggest a change in the character of the activity across the solar cycle. One is reminded of the appearance of the solar disk near solar MAX compared to MIN. At the higher phases of the cycle, the disk often is covered with several patches of plage associated with active sunspot groups, or decaying regions. During the lower phases of the cycle, in contrast, the disk mostly is plage-free, and yet still broadly covered by the lacy supergranulation network (which also is present at cycle MAX, but not so evident against the backdrop of the more dramatic plage regions). The network has a weak coronal signature, but nonetheless substantial enough that the global X-ray luminosity of the Sun is only a few times lower at solar MIN. Thus, the bends in the power laws must simply reflect a transition between cool-corona supergranulation at the lower phases of the cycle, segueing into hot-corona plage as the cycle advances toward MAX.

Strikingly, most of the important flux–flux correlations continue their power-law behavior down to the lowest intensities, rather than, say, leveling off before the minimum (as one might expect if a cool reference species, say Mg II in Fig. 15a, had a significant contribution from a heating process, for example shock waves in the low chromosphere, that had little penetrative impact on the higher hotter layers). This suggests that the expedient partitioning of the Mg II fluxes into core and block has had a positive impact on isolating

the chromospheric emission component, much what the basal subtraction procedure on the stellar side was intended to accomplish (Rutten et al. 1991).

Another curiosity of the solar-stellar power laws is the dominance of Si III in the Sun and α Cen A, but a return to the "normal" activity hierarchy in α Cen B. In the lower activity objects, the energy balance seems to favor the FUV side, especially the Si III/Si IV thermal regime (5–8$\times 10^4$ K). In more active objects like α Cen B, the energy balance apparently shifts to the coronal side, where the FUV emissions play a subsidiary role, perhaps arising mainly in conductive interfaces at the bases of hot coronal loops in the now dominant active regions. In particular, α Cen B's coronal X-rays are up to ten times more intense than FUV Si III at the peak of B's cycle, whereas the two distinct thermal species are more comparable in strength in α Cen A.

These schematic activity transitions are reminiscent of the "plage-dominated" versus "spot-dominated" photometric dichotomy among sunlike stars, discussed most recently by Radick et al. (2018). For the plage-dominated stars, of which the Sun is an example, the broad-band optical brightness rises (albeit very slightly) with increasing chromospheric Ca II intensity. Apparently the brightness enhancements associated with active-region faculae (photospheric counterparts of plage) are enough to compensate the darkening due to the accompanying starspots. Just the opposite is true for the spot-dominated stars, which tend to be more Ca II-active than the Sun: the optical brightness falls (again very slightly) with higher HK intensity. In this case, the darkening impact of the starspots apparently outweighs the facular brightening. In fact, Radick et al. proposed that the Sun is on the cusp of the dichotomy, where the spot darkening and facular brightening are nearly in balance. Is it a coincidence that the flux–flux power laws also appear to transition in character from low-activity α Cen A, through the Sun, up to higher activity α Cen B? Perhaps an accident, but the suggested increasing importance of the spots jibes with the transition to "normal" stellar power laws in B, recalling that the historical UV/X-ray surveys tended to be biased toward more active stars owing to limited instrumental sensitivity (e.g., *IUE, Einstein*, and *ROSAT*).

In a related vein, Foukal (2018) has offered a novel explanation for the so-called "Vaughan-Preston Gap" in activity–color diagrams. The Gap refers to a lower density of sunlike stars at intermediate chromospheric HK intensities, just above the Sun's position but below a higher-intensity band occupied by generally young, Ca II-active stars. Empirically on the Sun, Foukal noted, the ratio of plage to sunspot area begins to bend over with increasing spot area on the rise to cycle MAX (likely the root of the stellar faculae versus spot dichotomy noted above). Because the global Ca II emission is sensitive to the plage area, the turn-down might suppress the chromospheric intensity to some extent, even though the

magnetic activity traced by the spot area has increased. If this effect continues to stars more active than the Sun, it could pull their HK emission downward in the activity-color diagram, creating a void, compared with their expected locations if the plage–sunspot area correlation had been more linear. Whatever causes the bend in the plage area relation at intermediate activity must alter course at some higher activity state, in order to fill in the high-HK branch on the upper side of the Gap. Foukal argued that the underlying cause is a change in the way that emerging surface fields are partitioned into flux ropes of different spatial scales. Whatever the cause, the Sun's location near the boundary reinforces the idea that its "special" behavior in other respects (like the flux–flux relations) might be traceable to the same type of transition in magnetic properties.

Along these lines, van Saders et al. (2016) proposed that coronal wind braking, which causes the spindown of young sunlike stars, appears to weaken near solar age, perhaps again owing to a re-organization of the star's field, in this case on global scales. These several indications suggest that more attention should be paid to the possibility that the Sun's magnetic engine might be operating in a delicately balanced regime.

Another curiosity is the empirical 0.05 dex flux shift of Si III between the Sun and α Cen A, which is less than expected given the 0.22–0.24 dex higher metallicity of the system. It is unlikely, however, that the reduced enhancement at low-TZ temperatures in α Cen A might represent an actual abundance depletion (say, as a consequence of the FIP-effect [First Ionization Potential: e.g., Laming et al. 1995], which selectively enhances low-FIP species like Si and Fe in the corona), because the comparison is relative to the Sun where presumably the same process would be operating. Further, the inferred enhancements of high-FIP C IV and N V in α Cen A are similar to that of Si III, whereas spectroscopic surveys (Allende Prieto et al. 2004) and Galactic chemical evolution models (e.g., Morel 2018) suggest that CNO abundances relative to iron might be as much as 0.1 dex lower for metal-rich stars with [Fe/H]$\sim$ +0.2 dex (like that of α Cen); roughly consistent with the small [C/Fe] and [O/Fe] depletions reported for AB (Table 1). To be sure, these deviations are modest, and probably are more related to differential excitation effects than metallicity.

Although the present study has focused on sunlike stars, there also is the broader context set by other stellar types, especially the M dwarfs (which have attracted attention as potential habitable-planet hosts). As part of the so-called "MUSCLES" *HST* Treasury Survey, Youngblood et al. (2017) have derived a number of FUV and NUV flux–flux correlations for 15 M1–M5 dwarfs spanning a range of Ca II activity (their Table 9). Much like α Cen B, the M-star Si IV–Si III correlation is close to 1:1, as is C IV–Si III. However, much like the Sun and α Cen A, the M-star N V–Si III slope falls below 1; especially striking since the equivalent pair for B shows $\alpha \sim 1.5$ (Fig. 16c, here). Further, the M-dwarf ISM-corrected

Lyα versus C II slope is about 0.6, like that of B; whereas the Sun and A show 1:1 correlations. Similarly, the M-dwarf Si III–C II relation is very close to 1:1, just as seen for α Cen B (Fig. 16b, here); whereas both the Sun and A have steeper slopes $\sim$1.5 . Such flux–flux differences must mirror systemic changes in the sub-coronal atmospheres; differences that should be reproduced by model simulations if they are to be considered successful (e.g., Fontenla et al. 2014).

How might the empirical flux–flux relations for the Sun be of value in other settings? Firstly, as alluded above, they offer a way to vet numerical simulations of stellar chromospheric/coronal structure; to improve the understanding of the underlying physical heating and cooling processes. Validated models, in turn, might be used to calculate the important, but "hidden," emissions in the Lyman Continuum regions of other stars, for the purpose of evaluating EUV radiation loading on exoplanetary atmospheres. Secondly, the flux–flux relations could be incorporated in proxy-based irradiance models; for example to extrapolate solar global activity indices into regimes above or below those spanned by contemporary records, say to explore consequences of a Maunder-like minimum (when sunspots mostly vanished for much of the 17th Century). Thirdly, analogous flux–flux proxy models, especially extended to solar EUV emissions, could be applied to estimate ionizing radiation fields of exoplanet hosts at the low end of the sunlike activity ladder, applying to the vast majority of solar neighborhood G stars of middling ages.

It is gratifying that a half century after Leo Goldberg advocated for the "solar–stellar connection," in a prestigious Russell Lecture to the American Astronomical Society, a fortuitous confluence of new missions and old techniques is providing our best-ever view of the Sun as a star, and the stars as suns in their own right.

A.   Flux–Flux Correlations

Table A1 summarizes the flux–flux correlations for nearly 80 combinations of species, based on the solar irradiance measurements from *SORCE* described earlier. Each pair has minimum and maximum values, representing the extremes of the up-binned fluxes over the 1.5 solar cycles covered by the *SORCE* mission. The next entries are parameters describing the quadratic fit to the pair-wise logarithmic fluxes (eq. 2). In some cases the relation is noticeably "bent," which is reflected in a significant difference between the two extreme slope values reported.

Table A1. Flux–Flux Power Laws

Pair No.	X-line	Y-line	$(x_{\min}, y_{\min})$	$(x_{\max}, y_{\max})$	c_1	$c_2^{\star}$	χ_r^2
1	2	3	4	5	6	7	8
1	c2796	c2820	(−5.629, −3.820)	(−5.595, −3.815)	0.160±0.002	0.11±0.02	4.5
2	c2803	c2820	(−5.613, −3.820)	(−5.583, −3.815)	0.196±0.002	0.13±0.03	4.2
3	c1506	c2796	(−7.548, −5.629)	(−7.497, −5.598)	0.73±0.01	0.5±0.1	3.8
4	c1506	c2803	(−7.548, −5.613)	(−7.497, −5.586)	0.59±0.01	0.5±0.1	2.1
5	c1506	c2820	(−7.548, −3.820)	(−7.497, −3.815)	0.114±0.001	0.07±0.01	3.3
6	MgII-2800	c2820	(−5.001, −3.820)	(−4.861, −3.815)	0.041±0.001	0.027±0.002	3.5
7	MgII-2800	c2796	(−5.001, −5.629)	(−4.861, −5.598)	0.264±0.003	0.19±0.02	2.6
8	MgII-2800	c2803	(−5.001, −5.613)	(−4.861, −5.585)	0.211±0.003	0.17±0.01	1.3
9	MgII-2800	c1506	(−5.001, −7.548)	(−4.861, −7.499)	0.366±0.002	0.33±0.01	1.6
10	MgII-2800	CII-1351	(−5.001, −8.396)	(−4.861, −8.328)	0.39±0.01	0.60±0.04	1.8
11	MgII-2800	OI-1302	(−5.001, −7.553)	(−4.861, −7.470)	0.563±0.004	0.64±0.02	1.9
12	MgII-2800	OI-1305	(−5.001, −7.224)	(−4.861, −7.146)	0.558±0.003	0.59±0.02	2.1
13	MgII-2800	HI-1215	(−5.001, −5.366)	(−4.861, −5.222)	1.162±0.004	0.90±0.02	2.4
14	MgII-2800	CII-1335	(−5.001, −6.950)	(−4.860, −6.804)	1.115±0.004	0.99±0.02	2.5
15	MgII-2800	CIII-1175	(−5.001, −7.442)	(−4.861, −7.321)	0.97±0.01	0.79±0.03	2.2
16	MgII-2800	SiIII-1206	(−5.001, −7.240)	(−4.861, −7.007)	1.89±0.01	1.44±0.03	4.6
17	MgII-2800	SiIV-1400	(−5.001, −7.385)	(−4.861, −7.196)	1.50±0.01	1.22±0.04	2.6
18	MgII-2800	CIV-1550	(−5.001, −7.036)	(−4.861, −6.925)	0.87±0.01	0.76±0.03	2.1
19	MgII-2800	NV-1240	(−5.001, −7.902)	(−4.861, −7.769)	1.13±0.01	0.81±0.04	2.2
20	MgII-2800	FeXII-1349	(−5.001, −9.683)	(−4.861, −9.390)	3.07±0.04	1.0±0.2	1.8
21	MgII-2800	X-rays	(−5.001, −7.016)	(−4.859, −6.454)	5.19±0.03	3.1±0.2	10.5
22	OI-1305	c1506	(−7.224, −7.548)	(−7.142, −7.500)	0.661±0.005	0.51±0.04	2.5
23	OI-1305	CII-1351	(−7.224, −8.396)	(−7.142, −8.329)	0.71±0.01	1.0±0.1	2.1
24	OI-1305	OI-1302	(−7.224, −7.553)	(−7.142, −7.469)	1.012±0.005	1.07±0.03	2.1

Table A1—Continued

Pair No.	X-line	Y-line	$(x_{\min}, y_{\min})$	$(x_{\max}, y_{\max})$	c_1	$c_2^\star$	χ_r^2
1	2	3	4	5	6	7	8
25	OI-1305	HI-1215	$(-7.224, -5.366)$	$(-7.142, -5.226)$	2.08 ± 0.01	1.4 ± 0.1	4.3
26	OI-1305	CII-1335	$(-7.224, -6.950)$	$(-7.142, -6.807)$	2.00 ± 0.01	1.6 ± 0.1	5.5
27	OI-1305	CIII-1175	$(-7.224, -7.442)$	$(-7.142, -7.324)$	1.74 ± 0.01	1.2 ± 0.1	4.3
28	OI-1305	SiIII-1206	$(-7.224, -7.240)$	$(-7.142, -7.014)$	3.38 ± 0.02	2.3 ± 0.1	8.1
29	OI-1305	SiIV-1400	$(-7.224, -7.385)$	$(-7.142, -7.201)$	2.71 ± 0.02	1.9 ± 0.1	5.5
30	OI-1305	CIV-1550	$(-7.224, -7.036)$	$(-7.142, -6.926)$	1.54 ± 0.01	1.2 ± 0.1	2.9
31	OI-1305	NV-1240	$(-7.224, -7.902)$	$(-7.142, -7.770)$	2.02 ± 0.01	1.3 ± 0.1	2.6
32	OI-1305	FeXII-1349	$(-7.224, -9.683)$	$(-7.142, -9.402)$	5.7 ± 0.1	1 ± 1	2.4
33	OI-1305	X-rays	$(-7.224, -7.016)$	$(-7.141, -6.455)$	9.4 ± 0.1	4.7 ± 0.4	9.5
34	HI-1215	c1506	$(-5.366, -7.548)$	$(-5.222, -7.499)$	0.315 ± 0.002	0.36 ± 0.01	2.1
35	HI-1215	CII-1335	$(-5.366, -6.950)$	$(-5.222, -6.804)$	0.960 ± 0.003	1.07 ± 0.02	4.1
36	HI-1215	CIII-1175	$(-5.366, -7.442)$	$(-5.222, -7.323)$	0.84 ± 0.01	0.85 ± 0.03	1.9
37	HI-1215	SiIII-1206	$(-5.366, -7.240)$	$(-5.222, -7.009)$	1.63 ± 0.01	1.58 ± 0.03	9.4
38	HI-1215	SiIV-1400	$(-5.366, -7.385)$	$(-5.222, -7.198)$	1.30 ± 0.01	1.31 ± 0.04	3.2
39	HI-1215	CIV-1550	$(-5.366, -7.036)$	$(-5.222, -6.926)$	0.751 ± 0.005	0.81 ± 0.03	1.9
40	HI-1215	NV-1240	$(-5.366, -7.902)$	$(-5.222, -7.770)$	0.98 ± 0.01	0.89 ± 0.04	1.7
41	HI-1215	FeXII-1349	$(-5.366, -9.683)$	$(-5.222, -9.397)$	2.71 ± 0.04	1.3 ± 0.2	2.0
42	HI-1215	X-rays	$(-5.366, -7.016)$	$(-5.220, -6.463)$	4.54 ± 0.03	3.5 ± 0.2	12.1
43	CII-1335	CII-1351	$(-6.950, -8.396)$	$(-6.802, -8.326)$	0.33 ± 0.01	0.61 ± 0.03	1.6
44	CII-1335	CIII-1175	$(-6.950, -7.442)$	$(-6.803, -7.319)$	0.862 ± 0.004	0.82 ± 0.03	1.4
45	CII-1335	SiIII-1206	$(-6.950, -7.240)$	$(-6.802, -7.007)$	1.697 ± 0.004	1.45 ± 0.02	5.2
46	CII-1335	SiIV-1400	$(-6.950, -7.385)$	$(-6.803, -7.195)$	1.346 ± 0.005	1.24 ± 0.03	1.3
47	CII-1335	CIV-1550	$(-6.950, -7.036)$	$(-6.802, -6.923)$	0.767 ± 0.004	0.79 ± 0.02	2.2
48	CII-1335	NV-1240	$(-6.950, -7.902)$	$(-6.802, -7.765)$	1.00 ± 0.01	0.86 ± 0.03	1.3

Table A1—Continued

Pair No.	X-line	Y-line	(x_{min}, y_{min})	(x_{max}, y_{max})	c_1	$c_2^\star$	χ_r^2
1	2	3	4	5	6	7	8
49	CII-1335	FeXII-1349	$(-6.950, -9.683)$	$(-6.802, -9.399)$	2.81 ± 0.04	1.0 ± 0.2	1.8
50	CII-1335	X-rays	$(-6.950, -7.016)$	$(-6.801, -6.441)$	4.67 ± 0.03	3.3 ± 0.1	8.4
51	CIII-1175	SiIII-1206	$(-7.442, -7.240)$	$(-7.315, -7.014)$	2.01 ± 0.01	1.6 ± 0.1	3.8
52	CIII-1175	SiIV-1400	$(-7.442, -7.385)$	$(-7.315, -7.196)$	1.57 ± 0.01	1.47 ± 0.04	2.6
53	CIII-1175	CIV-1550	$(-7.442, -7.036)$	$(-7.315, -6.921)$	0.878 ± 0.004	0.98 ± 0.02	2.0
54	CIII-1175	NV-1240	$(-7.442, -7.902)$	$(-7.315, -7.762)$	1.15 ± 0.01	1.07 ± 0.03	1.5
55	CIII-1175	FeXII-1349	$(-7.442, -9.683)$	$(-7.315, -9.409)$	3.34 ± 0.05	1.1 ± 0.3	2.3
56	CIII-1175	X-rays	$(-7.442, -7.016)$	$(-7.313, -6.434)$	5.45 ± 0.03	3.9 ± 0.2	9.1
57	SiIII-1206	SiIV-1400	$(-7.240, -7.385)$	$(-7.006, -7.195)$	0.793 ± 0.003	0.85 ± 0.01	3.0
58	SiIII-1206	CIV-1550	$(-7.240, -7.036)$	$(-7.006, -6.923)$	0.457 ± 0.003	0.52 ± 0.01	4.8
59	SiIII-1206	NV-1240	$(-7.240, -7.902)$	$(-7.006, -7.766)$	0.595 ± 0.004	0.58 ± 0.02	3.2
60	SiIII-1206	FeXII-1349	$(-7.240, -9.683)$	$(-7.006, -9.397)$	1.67 ± 0.03	0.8 ± 0.1	1.4
61	SiIII-1206	X-rays	$(-7.240, -7.016)$	$(-7.004, -6.441)$	2.76 ± 0.02	2.3 ± 0.1	7.3
62	SiIV-1400	CIV-1550	$(-7.385, -7.036)$	$(-7.193, -6.921)$	0.564 ± 0.003	0.64 ± 0.01	3.0
63	SiIV-1400	NV-1240	$(-7.385, -7.902)$	$(-7.193, -7.764)$	0.742 ± 0.004	0.70 ± 0.02	1.9
64	SiIV-1400	FeXII-1349	$(-7.385, -9.683)$	$(-7.193, -9.401)$	2.10 ± 0.03	0.9 ± 0.1	2.5
65	SiIV-1400	X-rays	$(-7.385, -7.016)$	$(-7.191, -6.438)$	3.42 ± 0.02	2.7 ± 0.1	11.2
66	CIV-1550	NV-1240	$(-7.036, -7.902)$	$(-6.918, -7.763)$	1.31 ± 0.01	1.07 ± 0.04	1.9
67	CIV-1550	FeXII-1349	$(-7.036, -9.685)$	$(-6.918, -9.410)$	3.78 ± 0.05	1.0 ± 0.3	1.9
68	CIV-1550	X-rays	$(-7.036, -7.017)$	$(-6.916, -6.439)$	6.11 ± 0.03	3.9 ± 0.2	11.5
69	NV-1240	FeXII-1349	$(-7.902, -9.683)$	$(-7.760, -9.405)$	2.90 ± 0.04	1.1 ± 0.2	2.1
70	NV-1240	X-rays	$(-7.902, -7.016)$	$(-7.758, -6.435)$	4.70 ± 0.03	3.7 ± 0.1	13.6
71	X-rays	FeXII-1349	$(-7.016, -9.683)$	$(-6.416, -9.409)$	0.63 ± 0.01	0.32 ± 0.03	2.2
72	NV-1238	NV-1242	$(-8.085, -8.367)$	$(-7.948, -8.218)$	1.21 ± 0.01	1.01 ± 0.04	3.9

Table A1—Continued

Pair No.	X-line	Y-line	$(x_{\min}, y_{\min})$	$(x_{\max}, y_{\max})$	c_1	$c_2^\star$	χ_r^2
1	2	3	4	5	6	7	8
73	SiIV-1393	SiIV-1402	$(-7.566, -7.851)$	$(-7.374, -7.661)$	0.965 ± 0.003	1.01 ± 0.01	3.8
74	CIV-1548	CIV-1551	$(-7.216, -7.505)$	$(-7.097, -7.390)$	0.940 ± 0.004	1.00 ± 0.02	2.6
75	MgII-2796	MgII-2803	$(-5.221, -5.402)$	$(-5.081, -5.263)$	1.010 ± 0.003	1.00 ± 0.02	4.9
76	MgII-2796	c2796	$(-5.221, -5.629)$	$(-5.080, -5.598)$	0.263 ± 0.003	0.20 ± 0.02	3.5
77	MgII-2803	c2803	$(-5.402, -5.613)$	$(-5.263, -5.586)$	0.207 ± 0.003	0.18 ± 0.01	1.5
78	c2796	c2803	$(-5.629, -5.613)$	$(-5.595, -5.586)$	0.82 ± 0.01	0.7 ± 0.1	2.5

Note. — Col. 2 is the short name of the species on the x-axis; Col. 3 is the short name of the species on the y-axis. In Cols. 4 and 5, x is $\log(f_{\text{X−line}}/f_{\text{BOL}})$ for the X-line; y similarly for the Y-line. In Col. 6, c_1 the linear coefficient of the quadratic fit, which is equivalent to the slope of the curve at $x_{\min}$. In Col. 7, $c_2^\star$ is the slope of the curve at $x_{\max}$: $c_1 + 2(x_{\max} - x_{\min})\,c_2$, where c_2 is the quadratic coefficient. Col. 8 is the (reduced) χ^2 of the fit, based on the assumption that the standard error of the mean of the up-binned, Olympic-filtered fluxes is a fair measure of the random statistical errors. In some cases, the reduced χ^2 is close to the expectation of unity, but in other cases it is much larger, indicating that the simple quadratic fit is inadequate, at least with respect to the assigned error.

REFERENCES

Allende Prieto, C., Barklem, P. S., Lambert, D. L., et al. 2004, A&A, 420, 183

Anderson, L. S., & Athay, R. G. 1989, ApJ, 346, 1010

Ayres, T. R. 1979, ApJ, 228, 509

Ayres, T. R., Marstad, N. C., & Linsky, J. L. 1981, ApJ, 247, 545

Ayres, T. R., Fleming, T. A., Simon, T., et al. 1995, ApJS, 96, 223

Ayres, T. R. 1997, J. Geophys. Res., 102, 1641

Ayres, T. R., Judge, P. G., Saar, S. H., et al. 2008, ApJ, 678, L121

Ayres, T. R. 2014, AJ, 147, 59

Ayres, T. R. 2015, AJ, 149, 58

Bazot, M., Bourguignon, S., & Christensen-Dalsgaard, J. 2012, MNRAS, 427, 1847

Boggess, A., Carr, F. A., Evans, D. C., et al. 1978, Nature, 275, 372

Bouvier, J. 1994, in 8th Cambridge Workshop on Cool Stars, Stellar Systems, and the Sun, Ed. J.-P. Caillault, Astronomical Society of the Pacific Conference Series 64, 151

Briel, U. G., Aschenbach, B., Balasini, M., et al. 2000, Proc. SPIE, 154

Carlsson, M., De Pontieu, B., & Hansteen, V. H. 2019, ARA&A, 57, 189

Carlsson, M., & Stein, R. F. 1995, ApJ, 440, L29

Carlsson, M., & Stein, R. F. 1997, ApJ, 481, 500

Chadney, J. M., Galand, M., Unruh, Y. C., et al. 2015, Icarus, 250, 357

Chamberlin, P. C., Woods, T. N., & Eparvier, F. G. 2008, Space Weather, 6, S05001

Claire, M. W., Sheets, J., Cohen, M., et al. 2012, ApJ, 757, 95

Cohen, L., Feldman, U., & Doschek, G. A. 1978, ApJS, 37, 393

Cram, L. E., & Dame, L. 1983, ApJ, 272, 355

De Pontieu, B., Title, A. M., Lemen, J. R., et al. 2014, Sol. Phys., 289, 2733

Dere, K. P., Del Zanna, G., Young, P. R., et al. 2019, ApJS, 241, 22

Dumusque, X., Pepe, F., Lovis, C., et al. 2012, Nature, 491, 207

Flannery, B. P., & Ayres, T. R. 1978, ApJ, 221, 175

Fontenla, J. M., Landi, E., Snow, M., et al. 2014, Sol. Phys., 289, 515

Fontenla, J. M., Linsky, J. L., Witbrod, J., et al. 2016, ApJ, 830, 154

Foukal, P. 2018, arXiv e-prints, arXiv:1810.06558

France, K., Loyd, R. O. P., Youngblood, A., et al. 2016, ApJ, 820, 89

France, K., Arulanantham, N., Fossati, L., et al. 2018, ApJS, 239, 16

Giacconi, R., Branduardi, G., Briel, U., et al. 1979, ApJ, 230, 540

Guinan, E. F., Ribas, I., & Harper, G. M. 2003, ApJ, 594, 561

Hallam, K. L., Altner, B., & Endal, A. S. 1991, ApJ, 372, 610

Hock, R. A. 2012, Ph.D. Thesis, University of Colorado, "The Role of Solar Flares in the Variability of the Extreme Ultraviolet Solar Spectral Irradiance"

Hughes, D. W., Rosner, R., & Weiss, N. O. 2007, The Solar Tachocline, Edited by D. W. Hughes, R. Rosner, N. O. Weiss, (Cambridge, UK: Cambridge University Press)

Jansen, F., Lumb, D., Altieri, B., et al. 2001, A&A, 365, L1

Joyce, M., & Chaboyer, B. 2018, ApJ, 864, 99

Kasting, J. F., Whittet, D. C. B., & Sheldon, W. R. 1996, Lunar and Planetary Science Conference 27, 655

Kervella, P., Bigot, L., Gallenne, A., et al. 2017, A&A, 597, A137

Kraft, R. P. 1967, ApJ, 150, 551

Laming, J. M., Drake, J. J., & Widing, K. G. 1995, ApJ, 443, 416

Linsky, J. L., & Ayres, T. R. 1978, ApJ, 220, 619

Linsky, J. L., & Wood, B. E. 1996, ApJ, 463, 254

Maehara, H., Shibayama, T., Notsu, S., et al. 2012, Nature, 485, 478

Martínez-Sykora, J., Hansteen, V., De Pontieu, B., et al. 2009, ApJ, 701, 1569

Matt, S. P., Pinzón, G., de la Reza, R., et al. 2010, ApJ, 714, 989

McClintock, W. E., Rottman, G. J., & Woods, T. N. 2005, Sol. Phys., 230, 225

Miglio, A., & Montalbán, J. 2005, A&A, 441, 615

Morel, T. 2018, A&A, 615, A172

Murray, S. S., Chappell, J. H., Kenter, A. T., et al. 1997, Proc. SPIE, 3114, 11

Pagano, I., Linsky, J. L., Valenti, J., et al. 2004, A&A, 415, 331

Parker, E. N. 1970, ARA&A, 8, 1

Peacock, S., Barman, T., Shkolnik, E. L., et al. 2019, ApJ, 886, 77

Pesnell, W. D., Thompson, B. J., & Chamberlin, P. C. 2012, Sol. Phys., 275, 3

Pevtsov, A. A., Fisher, G. H., Acton, L. W., et al. 2003, ApJ, 598, 1387

Preibisch, T. 1997, A&A, 320, 525

Raassen, A. J. J., Ness, J.-U., Mewe, R., et al. 2003, A&A, 400, 671

Radick, R. R., Lockwood, G. W., Henry, G. W., et al. 2018, ApJ, 855, 75

Ribas, I., Bolmont, E., Selsis, F., et al. 2016, A&A, 596, A111

Robrade, J., Schmitt, J. H. M. M., & Favata, F. 2005, A&A, 442, 315

Robrade, J., Schmitt, J. H. M. M., & Favata, F. 2012, A&A, 543, A84

Rottman, G. 2005, Sol. Phys., 230, 7

Rutten, R. G. M., Schrijver, C. J., Lemmens, A. F. P., et al. 1991, A&A, 252, 203

Rutten, R. J. 1995, in Helioseismology, ESA Special Publication 376, 151

Saar, S. H., & Osten, R. A. 1997, MNRAS, 284, 803

Schmitt, J. H. M. M., Collura, A., Sciortino, S., et al. 1990, ApJ, 365, 704

Schrijver, C. J. 1983, A&A, 127, 289

Shine, R. A., & Linsky, J. L. 1972, Sol. Phys., 25, 357

Shine, R. A. 1983, ApJ, 266, 882

Skumanich, A. 1972, ApJ, 171, 565

Stauffer, J. B., & Hartmann, L. W. 1986, PASP, 98, 1233

Thiemann, E. M. B. 2016, Ph.D. Thesis, University of Colorado, "Multi-Spectral Sensor
     Driven Solar EUV Irradiance Models with Improved Spectro-Temporal Resolution
     for Space Weather Applications at Earth and Mars"

Title, A. M., & Schrijver, C. J. 1998, in Tenth Cambridge Workshop on Cool Stars, Stellar
     Systems, and the Sun, Eds. R.A. Donahue & J.A. Bookbinder, Astronomical Society
     of the Pacific Conference Series 154, 345

Truemper, J. 1982, Advances in Space Research, 2, 241

van Saders, J. L., Ceillier, T., Metcalfe, T. S., et al. 2016, Nature, 529, 181

Weber, E. J., & Davis, L. 1967, ApJ, 148, 217

Weisskopf, M. C., O'dell, S. L., & van Speybroeck, L. P. 1996, Proc. SPIE, 2805, 2

Wilson, O. C. 1978, ApJ, 226, 379

Wilson, O. C., & Vainu Bappu, M. K. 1957, ApJ, 125, 661

Woods, T. N., Eparvier, F. G., Hock, R., et al. 2012, Sol. Phys., 275, 115

Wood, B. E., Redfield, S., Linsky, J. L., et al. 2005, ApJS, 159, 118

Woodgate, B. E., Tandberg-Hanssen, E. A., Bruner, E. C., et al. 1980, Sol. Phys., 65, 73

Woodgate, B. E., Kimble, R. A., Bowers, C. W., et al. 1998, PASP, 110, 1183

Woods, T. N., & Rottman, G. 2005, Sol. Phys., 230, 375

Woods, T. N., Tobiska, W. K., Rottman, G. J., et al. 2000, J. Geophys. Res., 105, 27195

Youngblood, A., France, K., Loyd, R. O. P., et al. 2017, ApJ, 843, 31

Zahnle, K. J., & Walker, J. C. G. 1982, Reviews of Geophysics and Space Physics, 20, 280